

ULTRAFAST OPTICAL SPECTROSCOPIC STUDY OF SEMICONDUCTORS IN HIGH
MAGNETIC FIELDS

By

XIAOMING WANG

A DISSERTATION PRESENTED TO THE GRADUATE SCHOOL
OF THE UNIVERSITY OF FLORIDA IN PARTIAL FULFILLMENT
OF THE REQUIREMENTS FOR THE DEGREE OF
DOCTOR OF PHILOSOPHY

UNIVERSITY OF FLORIDA

2008

© 2008 Xiaoming Wang

To my wife and my daughter

ACKNOWLEDGMENTS

First of all, I would like to express my deep gratitude to my advisor, Professor David Reitze, for his supervision, instruction, encouragement, tremendous support and friendship during my Ph.D. He guided me into a beautiful world of ultrafast optics. His profound knowledge of ultrafast optics, condensed matter physics and his teaching style always impress me and will help me all through my life.

I wish to thank my supervisory committee, Prof. Stanton, Prof. Tanner, Prof. Rinzler and Prof. Kleiman, for their instructions for my thesis and finding errors in my thesis manuscript.

I would like to give my sincere thanks to the visible optics staff scientists at the National High Magnetic Field Laboratory, Dr. Xing Wei and Dr. Stephen McGill, for their excellent technical support for our experiments. I learned plenty of knowledge about spectrometers, fibers, cryogenics, magnets and LabView program from them. Also I give my special thanks to Dr. Brandt, former director of DC facility at NHMFL, for his great administrative assistance.

I appreciate the experimental and theoretical supervisions we received for our research projects from Prof. Stanton from University of Florida, Prof. Kono from Rice University and Prof. Belyanin from Texas A&M University. Special thanks should be given to my research collaborators, Dr. Young-dahl Cho and Jinho Lee. Our research projects would not be so successful without their contribution.

This work is supported by National Science Foundation and In House Research Program at the National High Magnetic Field Laboratory.

Finally I want to send my warmest thanks to my wife and my daughter, my parents and parents in law for their endless love and support. I could not complete my studies without their emotional and financial support.

TABLE OF CONTENTS

	<u>page</u>
ACKNOWLEDGMENTS	4
LIST OF TABLES	8
LIST OF FIGURES	9
ABSTRACT	14
CHAPTER	
1 INTRODUCTION AND OVERVIEW	16
1.1 Semiconductors and Quantum Wells	17
1.2 Magneto-spectroscopy in High Magnetic Fields	18
1.3 Motivation for Performing Ultrafast Spectroscopy in High Magnetic Fields	19
1.3.1 Quantum Optical Processes in Semiconductors--Superfluorescence	19
1.3.2 Studies of Technologically Interesting Materials	20
2 HIGH FIELD MAGNETO-OPTICAL TECHNIQUES AND FUNDAMENTALS OF MAGNETO-OPTICAL SPECTROSCOPY	24
2.1 Introduction	24
2.2 Basic Background of Optical Response of Solids	24
2.3 Magneto-spectroscopy of Semiconductors--Methods	27
2.3.1 Transmission Spectroscopy	27
2.3.2 Reflection Spectroscopy	28
2.3.3 Photoluminescence (PL) Spectroscopy	29
2.4 Time-resolved Spectroscopy of Semiconductors	29
2.5 CW Optical Experimental Capabilities at the NHMFL	32
2.6 Development of Ultrafast Magneto-optical Spectroscopy at NHMFL	34
2.6.1 Introduction of Ultrafast Optics	34
2.6.2 Magnet and Cryogenics for Ultrafast Optics at NHMFL	35
2.6.3 Ultrafast Light Sources	36
2.6.3.1 Ti:Sapphire femtosecond oscillator	36
2.6.3.2 Chirped pulse amplifier	37
2.6.3.3 Optical parametric amplifier	38
2.6.3.4 Streak camera	39
3 ELECTRONIC STATES OF SEMICONDUCTOR QUANTUM WELL IN MAGNETIC FIELD	57
3.1 Introduction	57
3.2 Band Structure of Wurzite and Zinc Blend Structure Bulk Semiconductors	57
3.3 Selection Rules	60

3.4	Quantum Well Confinement	61
3.5	Density of States in Bulk Semiconductor and Semiconductor Nanostructures	63
3.6	Magnetic Field Effect on 2D Electron Hole Gas in Semiconductor Quantum Well ...	64
3.7	Excitons and Excitons in Magnetic Field.....	66
3.7.1	Excitons.....	66
3.7.2	Magneto –excitons.....	67
4	MAGNETO-PHOTOLUMINESCENCE IN INGAAS QWS IN HIGH MAGNETIC FIELDS.....	78
4.1	Background	78
4.2	Motivation for Investigating PL from InGaAs MQW in High Magnetic Fields Using High Power Laser Excitation.....	81
4.3	Sample Structure and Experimental Setup.....	82
4.4	Experimental Results and Discussion	82
4.4.1	Prior Study of $\text{In}_x\text{Ga}_{1-x}\text{As}/\text{GaAs}$ QW Absorption Spectrum	82
4.4.2	PL Spectrum Excited with High Peak Power Ultrafast Laser in High Magnetic Field	84
4.5	Summary	87
5	INVESTIGATIONS OF COOPERATIVE EMISSION FROM HIGH-DENSITY ELECTRON-HOLE PLASMA IN HIGH MAGNETIC FIELDS	98
5.1	Introduction to Superfluorescence (SF).....	98
5.1.2	Spontaneous Emission and Amplified Spontaneous Emission.....	99
5.1.3	Coherent Emission Process--Superradiance or Superfluorescence	101
5.1.4	Theory of Coherent Emission Process--SR or SF in Dielectric Medium	106
5.2	Cooperative Recombination Processes in Semiconductor QWs in High Magnetic Fields.....	109
5.2.1	Characteristics of SF Emitted from InGaAs QW in High Magnetic Field.....	110
5.2.2	Single Shot Random Directionality of PL Emission	112
5.2.3	Time Delay between the Excitation Pulse and Emission.....	113
5.2.4	Linewidth Effect with the Carrier Density.....	113
5.2.5	Emission intensity Effect with Carrier Density	113
5.2.6	Threshold Behavior.....	114
5.2.7	Exponential Growth of Emission Strength with the Excited Area	114
5.3	Experiments and Setup.....	115
5.4	Experimental Results and Discussion	117
5.4.1	Magnetic Field and Power Dependence of PL	117
5.4.2	Single Shot Experiment for Random Directionality of In Plane PL.....	119
5.4.3	Control of Cherece of In Plane PL from InGaAs QW in High Magnetic Field	120
5.4.4	Discussion.....	121
5.5	Summary	125
6	STUDY OF CARRIER DYNAMICS OF ZINC OXIDE SEMICONDUCTORS WITH TIME RESOLVED PUMP-PROBE SPECTROSCOPY	140

6.1	Introduction	140
6.2	Background of Crystal Structure and Band Structure of ZnO Semiconductors	141
6.3	Valence Band Symmetry and Selection Rules of Excitonic Optical Transition in ZnO Semiconductors.....	142
6.4	Impurity Bound Exciton Complex (I line) in ZnO and Zeeman Splitting	144
6.5	Samples and Experimental Setup for Reflection and PL Measurement	146
6.6	Results and Discussion.....	147
6.7	Time Resolved Studies of Carrier Dynamics in Bulk ZnO, ZnO Epilayers, and ZnO Nanorod	149
6.8	Experimental Results and Discussion	151
	6.8.1 Relaxation Dynamics of A-X and B-X in Bulk ZnO.....	151
	6.8.2 Relaxation Dynamics of A-X and B-X in ZnO Epilayer and Nanorod	152
7	CONCLUSION AND FUTURE WORK	172
APPENDIX		
A	SAMPLE MOUNT AND PHOTOLUMINESCENCE COLLECTION.....	176
B	PIDGEON-BROWN MODEL	179
LIST OF REFERENCES.....		182
BIOGRAPHICAL SKETCH		190

LIST OF TABLES

<u>Table</u>		<u>page</u>
1-1	Some band parameters for some III-V compound semiconductors and their alloys.	22
3-1	Periodic parts of Bloch functions in semiconductors	70
3-2	Selection rules for interband transitions using the absolute values of the transition matrix elements.....	71
5-1	Some experimental conditions for observation of super fluorescence in HF gas.....	126
6-1	Some parameters of ZnO bulk semiconductors	155

LIST OF FIGURES

<u>Figure</u>	<u>page</u>
1-1 Physical and energy structure of semiconductor multiple quantum well	23
2-1 Transmission spectrum of InGaAs/GaAs MQW at 30 T and 4.2 K	40
2-2 Reflection spectrum of ZnO epilayer at 4.2K.....	41
2-3 e-h recombination process and photoluminescence spectrum in semiconductors.....	42
2-4 Simple illustration of optical pump-probe transient absorption or reflection experiment.....	43
2-5 Experimental setup for optical pump-probe spectroscopy and TRDR spectrum of ZnO	44
2-6 Time resolved photoluminescence spectrum of $\text{In}_x\text{Ga}_{1-x}\text{As}/\text{AlGaAs}$ MQW at 4.2K	46
2-7 Technical drawing of the 30 Tesla resistive magnet in cell 5 at NHMFL	46
2-8 Technical drawing of cryostat and optical probe for CW optical spectroscopy at NHMFL.....	47
2-9 Block diagram of the CW magneto optical experiment setup at the NHMFL.	48
2-10 Schematic diagram of modified magneto optical cryostat for direct ultrafast optics.	49
2-11 Technical drawing of the 17 Tesla superconducting magnet SCM3 in cell 3 at NHMFL.....	50
2-12 Technical drawing of the special optical probe designed for superconducting magnet 3 in cell 3 at the NHMFL.....	51
2-13 Schematic diagram of Coherent Mira 900F femtosecond laser oscillator	52
2-14 Schematic diagram of Coherent Legend-F chirped pulse amplifier (CPA).....	53
2-15 Top view scheme of layout of the optical elements and beam path in TOPAS OPA.....	54
2-16 Operation principle of a streak camera	55
2-17 Block diagram of ultrafast optics experimental setup in cell 3 and 5 at NHMFL	56
3-1 Band structure of Zinc blend semiconductors	72
3-2 Band structure of wurzite structure semiconductors.....	73

3-3	Schematic diagrams of band alignment and confinement subbands in type I semiconductor quantum well.....	74
3-4	Density of states in different dimensions.....	75
3-5	Electronic energy states in a semiconductor quantum well in the presence of a magnetic field.....	76
3-6	Calculation of free electron hole pair energy and magneto exciton energy of $\text{In}_x\text{Ga}_{1-x}\text{As}/\text{GaAs}$ QW as function of magnetic field.....	77
4-1	Magneto absorption spectrum and schematic diagram of interband Landau level transitions.....	88
4-2	Magnetophotoluminescence experimental results of band gap change and effective mass change.....	89
4-3	Valence band mixing of heavy hole and light hole subbands in semiconductor quantum well.....	90
4-4	Structure of $\text{In}_{0.2}\text{Ga}_{0.8}\text{As}/\text{GaAs}$ multiple quantum well.....	91
4-5	Faraday configuration in magnetic field.....	92
4-6	Energy levels of electron and hole quantum confinement states in $\text{In}_x\text{Ga}_{1-x}\text{As}$ quantum wells.....	93
4-7	Magneto-photoluminescence spectrum of $\text{In}_x\text{Ga}_{1-x}\text{As}$ quantum well at 10K.....	94
4-8	Landau fan diagram of absorption and PL spectrum of $\text{In}_x\text{Ga}_{1-x}\text{As}$ quantum well in magnetic field up to 30 T.....	95
4-9	Magneto-PL and excitation density dependence of the integrated PL in $\text{In}_x\text{Ga}_{1-x}\text{As}$ quantum wells at 20 T and 10 K.....	96
4-10	Theoretical calculation and experimental results of PL in high magnetic field.....	97
5-1	Spontaneous emission and amplified spontaneous emission process of a two level atom system.....	128
5-2	Four steps in the formation of collective spontaneous emission--SF in N atom system.....	129
5-3	Schematic diagram of the configuration for collection of in plane PL from InGaAs multiple QW in high magnetic field.....	130
5-4	Experimental schematic showing the configuration for a single shot experiment on $\text{In}_x\text{Ga}_{1-x}\text{As}$ QWs.....	131

5-6	Fitting method to determine line widths using a Lorentzian and Gaussian function for the sharp peak and broader lower-energy peak.....	133
5-7	Excitation power dependent PL spectrum and fitting results of in plane emission	134
5-8	Excitation spot size effect on the in plane PL emission.....	135
5-9	Single shot directionality measurement of in plane PL emission in SF regime	136
5-10	Single shot directionality measurement of in plane PL emission in ASE regime	137
5-11	Schematic diagram of the configuration of control of emission directionality in $\text{In}_x\text{Ga}_{1-x}\text{As}$ multiple QW	138
5-12	Control of coherence of in plane PL emission in $\text{In}_x\text{Ga}_{1-x}\text{As}$ QW	139
6-1	Top view of the lattice structure of a wurtzite ZnO crystal	156
6-2	The orientation of light polarization with respect to the ZnO unit cell	157
6-3	Band structures and symmetry of each band of a ZnO semiconductor.	158
6-4	Schematic of types of impurity bound exciton complexes	159
6-5	Energy diagram of Zeeman splitting of neutral bound excitons in ZnO	160
6-6	Schematic diagram of Voigt configuration of c-plane ZnO in magnetic field	161
6-7	Reflection spectrum of a-plane bulk ZnO semiconductor for different linear optical polarization at 4.2K.....	162
6-8	The magneto-PL spectrum of <i>a</i> and <i>c</i> -plane bulk ZnO sample and Zeeman splitting at 4.2K.....	163
6-9	Comparison of reflection and PL spectrum of c-plane bulk ZnO.....	164
6-10	Comparison of reflection and PL spectrum of c-plane epilayer ZnO at 4.2 K.....	165
6-11	Schematic diagram of the pump-probe experimental setup for measuring TRDR of ZnO semiconductors.	166
6-12	TRDR plots of a-plane bulk ZnO semiconductor at 4.2K and exponential decay fitting line.....	167
6-13	Fast decay in TRDR of A-X in a-plane bulk ZnO and the fitting with convolution of Gaussian function and exponential decay function	168
6-14	Temperature dependent TRDR of A-X recombination in c-plane bulk ZnO	169

6-15	TRDR plots of excitonic recombination in ZnO epilayer for different exciton states.....	170
6-16	Experimental TRDR plot of ZnO nanorod sample at 10K and fitting result.....	171
A-1	Detailed schematic diagram of sample mount and PL collection used in the experiment.....	178

LIST OF ABBREVIATIONS

BEC	Bound exciton complex
CCD	Charged coupled device
CPA	Chirped pulse amplifier
CW	Continuous wave
DOS	Density of states
LL	Landau level
MQW	Multiple quantum well
NHMFL	National High Magnetic Field Laboratory
OPA	Optical parametric amplifier
PL	Photoluminescence
PMT	Photomultiplier tube
SCM	Superconducting magnet
SF	Superfluorescence
TRDR	Time resolved differential reflectivity
X	Exciton

Abstract of Dissertation Presented to the Graduate School
of the University of Florida in Partial Fulfillment of the
Requirements for the Degree of Doctor of Philosophy

ULTRAFAST OPTICAL SPECTROSCOPIC STUDY OF SEMICONDUCTORS IN HIGH
MAGNETIC FIELDS

By

Xiaoming Wang

May 2008

Chair: David H. Reitze
Major: Physics

We studied the magneto-excitonic states of two-dimensional (2D) electron and hole gas in $\text{In}_x\text{Ga}_{1-x}\text{As}/\text{GaAs}$ multiple quantum wells (MQW) with continuous wave (CW) optical spectroscopic methods, including transmission and photoluminescence spectroscopy, in high magnetic field up to 30 Tesla. Interband Landau level (LL) transitions are clearly identified. The anticrossing behavior in the Landau fan diagram of the transmission spectrum is interpreted as dark and bright exciton mixing due to Coulomb interaction. With the unique facility of ultrafast optics at National High Magnetic Field Laboratory, we are able to change the 2D electron hole gas into 0D and increase density of each quantum state as well as the actual sheet carrier density in the quantum well (up to 10^{12}cm^{-2}) dramatically. Under these conditions, interactions between electron and hole pairs confined in 0D system play a very important role in the electron hole recombination process. With high power pulsed lasers and cryogenic equipment, we studied the strong magneto photoluminescence emission from $\text{In}_x\text{Ga}_{1-x}\text{As}/\text{GaAs}$ MQW in high magnetic field. By analyzing the power dependent, field dependent and direction dependent PL spectrum, the abnormally strong PL emission from $\text{In}_x\text{Ga}_{1-x}\text{As}/\text{GaAs}$ MQW in high magnetic field is found to be the result of cooperative recombination of high density magneto electron-hole plasmas.

This abnormally strong photoluminescence from $\text{In}_x\text{Ga}_{1-x}\text{As}/\text{GaAs}$ MQW in high magnetic field under CPA excitation is proved to be superfluorescence.

We studied CW spectroscopic properties of ZnO semiconductors including reflectivity and photoluminescence at different crystal orientations. A, B excitonic states in ZnO semiconductors are clearly identified. Also, with time resolved pump probe spectroscopy, we studied the carrier dynamics of excitonic states of A and B in bulk ZnO as well as ZnO epilayer and nanorods.

CHAPTER 1 INTRODUCTION AND OVERVIEW

During the past few decades, the transport and optical properties of electron (e) hole (h) gas in two-dimensional (2D) semiconductor quantum well (QW) in magnetic field have been studied extensively in theory and experiments [1-5]. However most of the magneto-optical studies are based on continuous wave (CW) optics or low magnetic field.

In this dissertation, we first investigate the magneto-excitonic states of 2D electron and hole gas in $\text{In}_x\text{Ga}_{1-x}\text{As}/\text{GaAs}$ multiple quantum wells (MQW) with CW optical spectroscopic methods, including transmission and photoluminescence (PL) spectroscopy. With the unique facility that exists at National High Magnetic Field Laboratory (30 Tesla magnetic field combined with intense ultrashort pulse lasers), we are able to change the 2D electron hole gas into a quasi-0D system, and increase carrier density of states of each quantum state as well as actual sheet carrier density dramatically. Under these conditions, the excitonic effect is suppressed because the Coulomb interaction between high-density e - h pairs is screened, while the interactions between e - h pairs confined in this quasi 0D system play a very important role in the recombination process.

With high power pulsed lasers and cryogenic equipment, we studied the strong magneto-PL emission from $\text{In}_x\text{Ga}_{1-x}\text{As}/\text{GaAs}$ MQW in high magnetic fields. With analyzing the power dependent, field dependent and single shot direction dependent PL spectrum, the abnormally strong PL emission is found to be result from a cooperative recombination process of high density magneto e - h plasmas, which is called superfluorescence (SF).

The second part of this thesis focuses on the CW and ultrafast optical spectroscopic study of ZnO semiconductors. Due to its unique band gap (~ 3.35 eV) and large exciton binding energy (~ 60 meV) at room temperature [6-10], these are promising materials for optoelectronic

applications, such as blue and ultraviolet emitters and detectors. By analyzing the CW spectra, the band structures, excitonic and impurity bound excitonic states are identified. By using pump-probe spectroscopy, the dynamics of different excitonic states are studied in bulk ZnO, ZnO epilayer and nanorods.

1.1 Semiconductors and Quantum Wells

By using epitaxial growth such as molecular beam epitaxy (MBE) and metal organic chemical vapor deposition (MOCVD), modern science and technology have provided us the methods of manufacturing a very thin epitaxial layer (~nm) of a semiconductor compound on another different semiconductor with interface of very high precision (atomic precision), thus allowing for ‘quantum-engineered’ materials and structures.

The optical properties of semiconductor QWs have been extensively studied [11-15], and many physical phenomena have been investigated thoroughly, i.e. interband transitions, inter-subband transitions.

Figure1-1 shows physical and band structure of III-V or II-VI group semiconductor multiple quantum wells, composed of periods of ABAB..., A and B are two layers of different type of semiconductor compounds, i.e. $\text{In}_x\text{Ga}_{1-x}\text{As}$ and GaAs. The bandgap of compound B (the well) lies within the bandgap of the compound A (the barrier). The thickness of barrier A is typically greater than 10 nm, so that carriers will be confined in the QW layers. This particularly unique property of semiconductor heterojunctions provides us an ideal system for studying the interesting physics and application of device in two dimensional electron gas system--carriers in QWs are confined in the z direction, the growth direction of QW, and still move freely in the quantum well plane, or x - y direction. The interface between barrier and well imposes confinement on carriers in QWs, which results in the formation of discrete quantum states in both conduction and valence band. In a semiconductor, if an electron in valence band is excited

to conduction band as a free electron, a hole will be left in valence band. Through the Coulomb interaction, this electron hole pair can form a hydrogen atom (H) like quasi-atom system: an exciton (X). In a semiconductor QWs, due to the spatial confinement and discrete quantum state confinement, excitonic effects are more pronounced than semiconductor bulks [16-20]. These discrete excitonic states of exciton provide a unique system to study quantum optical processes of carriers in semiconductor quantum wells.

1.2 Magneto-Spectroscopy in High Magnetic Fields

In the presence of a high magnetic field, the cyclotron energy $\hbar\omega_c$ of a charge carrier is greater than the exciton binding energy E_b (for GaAs, $\hbar\omega_c=4E_b$ above 20T). Thus, we open a new regime to study semiconductor magneto-optics, where the magnetic field effect due to the formation of Landau levels (*LLs*) will suppress the exciton effect. Also, in high magnetic field, electrons and holes populate on *LLs*, which provide us a system to study the mid infrared light driven intraband *LL* transitions. Many new physical processes can be explored in semiconductor quantum wells at high magnetic fields [21-25].

Another impact that applied high magnetic fields have on a semiconductor QW is an alteration of the carrier confinement. Free carriers are confined in QW plane since the magnetic length l_B is on the order of a few nm. At high magnetic fields, the density of states (DOS) of a two dimensional electron gas system will evolve into a zero dimensional system, like a quantum dot; the separation between *LLs* varies with the intensity of magnetic field. Magneto-excitons (or magneto-plasmas) confined in quasi-nanorods in semiconductor QWs at high magnetic field provides us with an atomic-like system with tunable internal energy levels to study quantum optics in solids.

In early studies of magneto-optics in semiconductor quantum wells, light sources used in the experiments were usually continuous wave (CW) white light or CW lasers (see Chapter.2.5 for detail), which provided static spectroscopic information only. In the past twenty years, with the development of ultrafast laser technology and magnet technology, time resolved spectroscopic studies of magneto optical experiments like time resolved Kerr rotation or time resolved Faraday rotation can be carried out in a split coil superconducting magnet [26-30]. However, time resolved dynamics of magneto-excitons populate on LLs in semiconductor QW has been carried out at fields less than 12 T [31-33] and not yet been realized at higher magnetic fields. Furthermore, in high magnetic fields, sheet carrier density in QW can also increased dramatically due to the 0D like DOS at each LL . If the excitation power of the pulsed laser is very large, i.e., as that achievable with amplified ultrafast laser systems (CPA) as the excitation light source, we can create a carrier density in excess of $10^{13}/\text{cm}^{-2}$ in the QWs. In this case, the $e-h$ response in the QW will be dominated by plasma-like instead of exciton-like behavior. These high-density magneto-plasmas confined in QWs interact with each other and correlate to each other before they start to recombine. This leads to many new and exciting physical phenomena, as we discussed later.

1.3 Motivation for Performing Ultrafast Spectroscopy in High Magnetic Fields

1.3.1 Quantum Optical Processes in Semiconductors--Superfluorescence

In high magnetic field, $e-h$ pairs are confined in a quasi 0D structure. Therefore, we can use this atom like system to study quantum optics in electron hole pair in high magnetic field, i.e. strong electromagnetic field induced energy splitting--AC Stark Effect [34] and cooperative recombination process--Superfluorescence [35].

In an atomic ensemble, if the atoms are in excited state, they will relax down to ground state through emission of photons. This process is called spontaneous emission if there is no

interaction between atoms during the emission. In the case where the decoherence time of the atom is significantly greater than the spontaneous emission time, due to the interaction between atoms, the atomic ensemble can evolve into to a coherent state and emit a burst of photons through a cooperative radiative process called superfluorescence. This type of emission, characterized by its short pulse width and high intensity compared to spontaneous emission, has been observed in rarefied gas systems [36], however, due to very short carrier decoherent time in solid, superfluorescence has not been observed so far.

1.3.2 Studies of Technologically Interesting Materials

In order to study quantum optics in semiconductor QW in high magnetic field, the intrinsic properties of semiconductor material are very crucial to observe quantum processes. These properties include band structure, electron and hole effective masses, QW structure, and barrier and well compositions.

Among all the III-V group and II-VI group semiconductor materials, III-V group compounds such as $\text{In}_x\text{Ga}_{1-x}\text{As}/\text{GaAs}$, $\text{In}_x\text{Ga}_{1-x}\text{As}/\text{InP}$, $\text{In}_x\text{Ga}_{1-x}\text{As}/\text{AlGaAs}$ and $\text{GaAs}/\text{AlGaAs}$ QW series are the best materials to study quantum optical phenomena of e - h pairs in semiconductor QWs.

These materials have been thoroughly studied using magneto-optical spectroscopy and their band structures are well known [37, 38]. First, their band gaps energy are in the near infrared region, which is very suitable for excitation with Ti: Sapphire ultrafast lasers; second, the electron subband and valence hole subband are separated reasonably well which cause less band complexity; third, the electron and hole effective mass in these materials are relatively small and the exciton binding energy are relatively large (~ 10 meV), which make it easy to observed higher LLs in high magnetic field. Some band structure constants of some III-V group semiconductors are listed in Table 1-1.

In this dissertation, we selected $\text{In}_x\text{Ga}_{1-x}\text{As}/\text{GaAs}$ MQW for the host material for 2D e - h gas. The behaviors of high density e - h pairs under high power excitation in high magnetic field are the main result in this dissertation.

Table 1-1. Some band parameters for some III-V compound semiconductors and their alloys.

Parameters	GaAs	InAs	InP	
$a_c(\text{\AA})$		5.65 ¹	6.05 ¹	5.87 ¹
$E_g^\Gamma(\text{mev})$		1519 ¹	417 ¹	1423 ¹
$E_g^x(\text{mev})$		1981 ¹	1443 ¹	1480 ¹
$\Delta_{so}(\text{mev})$		341 ¹	390 ¹	108 ¹
$m_e^*(\Gamma)$		0.067 ¹	0.026 ¹	0.0795 ¹
$m_e^*(X)$		1.9 ¹	0.64 ¹	0.077 ¹
$m_{hh}^*(m_e)$		0.45 ¹	0.41 ¹	0.64 ¹
$m_{lh}^*(m_e)$		0.082 ¹	0.026 ¹	

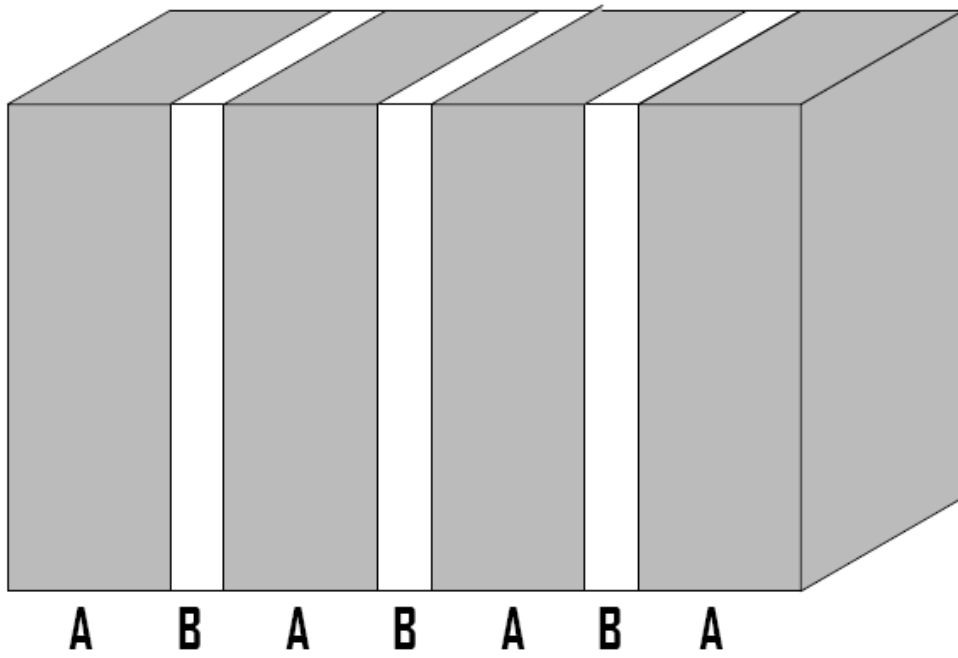
¹ Reference [37]

a_c is the crystal lattice constant in c direction.

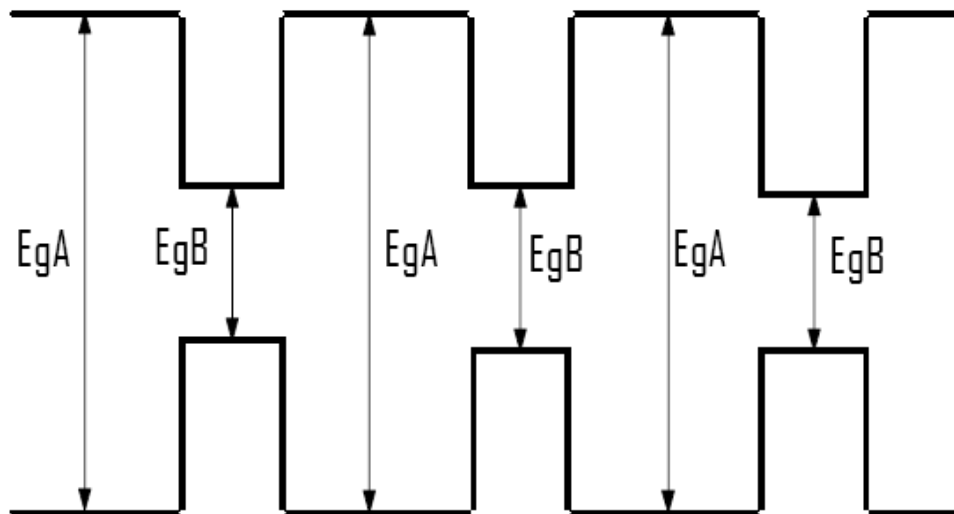
E_g^Γ and E_g^x are the bandgaps at Γ and X point.

Δ_{so} is the spin orbit interaction, $m_e^*(\Gamma)$ and $m_e^*(X)$ are the electron effective mass at Γ and x point.

m_{hh}^* and m_{lh}^* are the effective mass of heavy hole and light hole.



(a)



(b)

Figure 1-1. Physical and energy structure of semiconductor multiple quantum well.(a) Physical structure type I semiconductor multiple quantum well, (b) Energy structure of type I semiconductor multiple quantum well

CHAPTER 2 HIGH FIELD MAGNETO-OPTICAL TECHNIQUES AND FUNDAMENTALS OF MAGNETO-OPTICAL SPECTROSCOPY

2.1 Introduction

In this chapter, we introduce the basics on optical response theory, including optical complex dielectric constant ϵ and refractive index n . We then give a background in the techniques used to study optical properties of semiconductors, discussed the experimental techniques of CW measurements on semiconductors, including transmission, reflection and photoluminescence spectroscopy.

To understand the carrier dynamics in semiconductors, pump-probe spectroscopy is employed. By understanding the how the dielectric constant ϵ and refractive index n change with carrier density N , we can study the time resolved differential transmission and reflection spectroscopy.

In addition, a detailed description is provided for the existing CW spectroscopic experimental setup at the NHMFL that will be used for our measurements. Finally and most importantly, to extend our research regime in high magnetic fields and ultrafast lasers, we have developed an ultrafast facility at the NHMFL to study the ultrafast magneto optical phenomena in high magnetic field. In this chapter, we give an overview of the ultrafast facility and describe the technical details.

2.2 Basic Background of Optical Response of Solids

In a solid state system, including semiconductors, the optical response such as light transmission and reflection is determined by the complex dielectric constant ϵ . Coupled with an underlying model for the physics that relates to the dielectric function, the knowledge of the dielectric function over a given spectral range completely specifies the optical behavior of the material. In Drude's model [39], ϵ is given by [40]

$$\varepsilon(\omega) = \varepsilon'(\omega) + i\varepsilon''(\omega) = \varepsilon_\infty - \frac{4\pi N e^2 \tau}{m_e \omega} \frac{\omega \tau - i}{\omega^2 \tau^2 + 1}, \quad 2-1$$

where N is the electron density, e is the electron charge, m_e is mass of electron, τ is a phenomenological relaxation time constant corresponding to the mean time between carrier and ion collisions, and ε_∞ is dielectric constant at high frequency ($\omega \rightarrow \infty$). The refractive index n is [40]

$$n(\omega) = \sqrt{\frac{1}{2} \left[\varepsilon' + \sqrt{(\varepsilon')^2 + (\varepsilon'')^2} \right]}, \quad 2-2$$

And the intensity absorption coefficient is [40]

$$\alpha(\omega) = \frac{\omega}{cn(\omega)} \varepsilon''(\omega), \quad 2-3$$

where α is also the absorption coefficient in Beer Lambert's law [40]

$$I(z) = I_0 \exp(-\alpha z). \quad 2-4$$

The expression for optical reflection is given by

$$R^2 = \frac{(n_1 - n_2)^2}{(n_1 + n_2)^2}, \quad 2-5$$

where n_1 and n_2 are the refractive index on both sides of a solid and the incident beam light is perpendicular to the solid surface.

In the low frequency of optical frequency regime, corresponding to the infrared part of spectrum where $\omega \tau \ll 1$, we have [40]

$$\varepsilon(\omega) \cong i\varepsilon''(\omega) = \frac{4\pi n e^2 \tau}{m_e \omega} \quad 2-6$$

and

$$n(\omega) = \sqrt{\frac{1}{2} \varepsilon''}, \quad 2-7$$

for the index of refraction and

$$\alpha(\omega) = \frac{\omega}{c} \sqrt{2\varepsilon''} \quad 2-8$$

for the absorption coefficient.

In high optical frequency regime where $\omega\tau \gg 1$, corresponding to ultraviolet part of spectrum, we have [40]

$$\varepsilon(\omega) \cong \varepsilon'(\omega) = \varepsilon_\infty \left(1 - \frac{\omega_p^2}{\omega^2} \right), \quad 2-9$$

where $\omega_p^2 = \frac{4\pi N e^2}{\varepsilon_\infty m_e}$ is plasma frequency.

For $\omega > \omega_p$, we have [40]

$$n(\omega) = \sqrt{\varepsilon'}. \quad 2-10$$

The relation between dielectric constant ε and optical susceptibility χ is [40]

$$\varepsilon(\omega) = 1 + 4\pi\chi(\omega), \quad 2-11$$

χ is a complex parameter, given as

$$\chi(\omega) = \chi'(\omega) + i\chi''(\omega). \quad 2-12$$

Since the dielectric function ε and optical susceptibility χ have both real and imaginary components, both of them will contribute the optical response such as the transmission T and reflection R. Therefore, the optical resonant frequencies correspondent to $\varepsilon(\omega)$ are not necessarily directly related to absorption peaks or dips on the transmission and reflection spectrum. However, Kramers-Kronig transformations [40] allow us to determine the real part of optical response function from the imaginary part at

all frequency and vice versa, so that we are able to figure out the frequency of optical resonance in the spectra.

The real part and imaginary part of optical susceptibility χ are related by [40]

$$\begin{aligned}\chi'(\omega) &= \frac{2}{\pi} \text{Pr} \int_0^{\infty} d\omega' \frac{\omega' \chi''(\omega')}{\omega'^2 - \omega^2} \\ \chi''(\omega) &= -\frac{2\omega}{\pi} \text{Pr} \int_0^{\infty} d\omega' \frac{\chi'(\omega')}{\omega'^2 - \omega^2}\end{aligned}, \quad 2-13$$

and

$$\text{Pr} \int_0^{\infty} d\omega' \frac{\omega' \chi''(\omega')}{\omega'^2 - \omega^2} = \lim_{\eta \rightarrow 0} \left[\int_0^{\omega' - \eta} \frac{\chi'(\omega')}{\omega'^2 - \omega^2} d\omega' + \int_{\omega + \eta}^{\infty} \frac{\chi'(\omega')}{\omega'^2 - \omega^2} d\omega' \right], \quad 2-14$$

where Pr refers to the principal part of the complex integral.

2.3 Magneto-spectroscopy of Semiconductors--Methods

In magneto-spectroscopic studies of semiconductors, many experimental techniques have been developed. These spectroscopic methods include transmission and reflection spectroscopy, photoluminescence (PL) and photoluminescence excitation (PLE) spectroscopy, and optical detected resonance spectroscopy (ODR). Here, we will restrict our discussion to the methods that have been applied in this dissertation.

2.3.1 Transmission Spectroscopy

Transmission spectroscopy [40-44] is very useful tool in the study of electronic states in quantum well (discussed later in Chapter 3, 3.6). The first investigations of GaAs/AlGaAs quantum wells used this method. From Eq. 2-3, we can see that $\alpha(\omega)$ is related only with ϵ'' so that we can find the resonant frequency directly from transmission spectrum. In transmission spectroscopy, a white light beam is incident on the semiconductor sample, which is usually placed in a cryostat, and the transmitted white light is collected and sent to a spectrometer. The spectrum will be resolved with the

spectrometer and the intensity of each wavelength is detected by either a CCD array or a photomultiplier. Using the CW optical setup at NHMFL, a typical transmission spectrum of GaAs/AlGaAs multiple quantum well in high magnetic field 30 Tesla and 4.2K is shown in Fig. 2-1. In this figure, we can clearly resolve several quantum states, which will be interpreted in detail in Chapter 4. The dips in spectrum correspond to specific interband transitions, which are the positions of excitonic states (see section 4.4). Using transmission spectroscopy, we can directly mark the energy positions of Gaussian shape absorption dips as excitonic states on the spectrum. However, care should be taken for the band gap of substrate and barrier materials that they are high enough from the well material band gap to avoid overwhelmed by the continuum states of the barrier and substrate materials.

2.3.2 Reflection Spectroscopy

Reflection spectroscopy is also an important method to study the optical properties of semiconductor materials [45-48]. In reflection spectroscopy a white light beam is incident on a sample and the reflected light is collected and sent to a spectrometer for frequency resolution. Compared with transmission spectroscopy, this method offers a few advantages. It has a good signal noise ratio and not affected by the substrate materials unless the optical depth of quantum well is large, and it is a good method to study the above band gap excitonic features in semiconductors possessing very high absorption coefficient, since in transmission spectrum these features will be overwhelmed by the high absorption coefficient. Reflection spectroscopy has a significant disadvantage: the refractive index n shown in Eq. 2-2 has both ε' and ε'' , which have different contributions to reflection so that the location of resonant electronic state position is not completely straightforward and further analysis is needed. Fig. 2-2 is a reflection spectrum of a 400

nm thick ZnO epilayer at 4.2 K, the energy positions of electronic states are not clearly resolved. However, for a very good approximation, we can identify the states at the arrow points shown on the figure as the energy positions of electronic states.

2.3.3 Photoluminescence (PL) Spectroscopy

PL spectroscopy is also a very important method to study excited states in semiconductors [49-53]. In transmission and reflection spectroscopy, information about the optical absorption processes is obtained. They cannot be used to provide information about the photon emission process. In PL spectroscopy, electrons in the valence band are excited with photons whose energy is higher than the band gap of the semiconductor sample, followed by relaxation down to the bottom of the conduction band. This leads to recombination with holes on the top of the valence band, which undergo a similar energy relaxation, simultaneously producing a photon, which has the energy of the transition (See Fig. 2-3(a)). From the photon emission, we can use PL spectroscopy to understand the excited states in the conduction and valence bands. Fig. 2-3(b) shows a typical PL spectrum measured with the ultrafast magneto-optical setup at NHMFL, we can observe clearly PL peaks in the spectrum. The detailed physics of this spectrum will be discussed in Chapter 3, 4 and 5.

2.4 Time-resolved Spectroscopy of Semiconductors

The CW optical spectroscopic techniques described above provide a wide range of methods to study the optical properties of photoexcited carriers in semiconductors. However, these methods provide the information of static states in semiconductors only. In order to understand the dynamical processes of photoexcited carriers, time-resolved spectroscopic techniques need to be employed. Since the 1970's, extensive studies of

time resolved carrier dynamics in semiconductor have been reported [54-58], which have opened a new research area for semiconductor optics.

The most common time resolved spectroscopic method used to investigate the carrier dynamics in semiconductors are pump-probe spectroscopy and time-resolved photoluminescence spectroscopy.

In Fig. 2-4, a basic illustration of degenerate (equal wavelength) ultrafast pump probe experiment is shown in transmission geometry. The laser pulses (in our case of duration ~ 100 fs) are split into two pulses called the pump pulse and probe pulse, and pump pulse is much stronger than probe pulse. The pump and probe pulses are spatially overlapped on the sample with an optical focusing lens. Pump pulses are absorbed by the sample and excite carriers, which change the optical properties such as refractive index n (See equation 2-1, 2-2). After a controlled time delay Δt , the probe pulse reaches the sample, the transmission of this probe pulse will be recorded. By changing the time delay Δt between pump and probe, we can record the intensity of transmission of probe pulse at different time delays. The absorption coefficient $\alpha(\omega)$ is time dependent, it changes after pump pulses excitation and will go back to original value. Therefore, the transmission of probe light also manifests the dependency on time delay Δt , because the relationship between T and $\alpha(\omega)$ is

$$T = \frac{I}{I_0} = \exp(-\alpha(\omega)L) \quad 2-15$$

Generally speaking, in optical pump-probe spectroscopy, the pump pulse excites certain optical process in a sample and the probe is used to map out the dynamics of this process.

A typical pump-probe spectroscopy experimental setup is shown in Fig. 2-5. In this spectrum resolved pump-probe setup, either the transmission or reflection of the probe is sent to a spectrometer before it reaches the PMT (Photo Multiplier Tube), so that change of probe light at different wavelength can be resolved and detected. The intensity of reflection or transmission of probe beam will be recorded at different time delay between pump and probe pulse by changing the relative optical path of pump beam. The spectrometer is used to select specific wavelengths to probe.

In many cases, the change of probe induced by pump pulses is normalized to see the magnitude of the effect. These techniques are called differential transmission spectroscopy (DTS) or different reflection spectroscopy (DRS), and the signals are given by

$$\begin{aligned}\frac{\Delta T}{T_0} &= \frac{T - T_0}{T_0} \\ \frac{\Delta R}{R_0} &= \frac{R - R_0}{R_0}\end{aligned}\tag{2-16}$$

For DTS, because of Eq. 2-15, we have

$$\frac{\Delta T}{T_0} = \exp(-\Delta\alpha(\omega)L) - 1 \approx -\Delta\alpha(\omega)L.\tag{2-17}$$

However, for the DRS, the expression is quiet complicated because R is associated with both real and imaginary part of dielectric constant (see Eqs. 2-1, 2-2 and 2-5). Thus, by measuring the time resolved DTS and DRS, we can infer the carrier dynamics in semiconductors. Fig. 2-5(b) shows a typical degenerate time-resolved differential transmission (TRDR) spectrum of ZnO epilayer at 4.2K.

Time-resolved differential transmission (TRDT) and reflection (TRDR) provide an indirect method to study the carrier dynamics with very good time resolution (~ 100 fs and shorter). However the mechanism of carrier recombination processes can not be inferred, i.e. the radiative and nonradiative carrier recombination processes cannot be distinguished from a pump-probe spectroscopy since both of them will contribute to carrier recombination. To solve this problem, alternative techniques are required to perform time-resolved study of the radiative processes. In time-resolved photoluminescence, PL emitted from sample is sent to a streak camera, with which temporal information of PL emission is acquired. The resolution of this method (\sim ps) is not as high as pump-probe spectroscopy. The combination of pump-probe spectroscopy and time resolved PL spectroscopy will give us a thorough understanding of photoexcited carrier dynamics in semiconductors.

Fig. 2-6 shows a TRPL spectrum measured from $\text{In}_x\text{Ga}_{1-x}\text{As}/\text{AlGaAs}$ MQW at 4.2K taken using a Hamamatsu streak camera. These time-resolved figures are typical data we use in this thesis and the detailed physics will be discussed in the following chapters.

2.5 CW Optical Experimental Capabilities at the NHMFL

Since the construction of the DC magnetic field facility at the National High Magnetic Field Laboratory (NHMFL), there has been high demand for research in magneto-optics, and many research projects have been accomplished with the well-developed CW magneto-optical techniques that have been established [59-68]. In this dissertation, many experiments were carried out to characterize $\text{In}_x\text{Ga}_{1-x}\text{As}/\text{GaAs}$ MQW sample by using the CW magneto optical setup at NHMFL in Tallahassee.

In order to reach high magnetic fields, we used a 31 Tesla resistive magnet in cell 5 at NHMFL. Fig.2-7 shows the schematic diagram of this magnet. This magnet is a resistive magnet consists of a few hundreds of thin copper disks (Bitter disks). The Bitter disks are connected electronically and electric current can flow through Bitter disks in a spiral pattern. In Fig.2-7, we can see that there are four coils of Bitter disks in the magnet housing. There are huge flows of electric current ($\sim 37\text{KA}$) in the magnet coils when they are in operation at full field, at the same time, cold water flows continuously through holes punched on the Bitter disks to remove the huge amount of heat ($\sim \text{MW}$) generated by the electric current.

In many magneto-optical experiments, low temperatures are usually required to measure transmission, reflection and photoluminescence. Specially designed cryostats and probes have been designed to work at liquid helium temperatures with these resistive magnets with bore size around 50mm. The technical drawing of a cryostat and probes are given in Fig. 2-8. This cryostat has a long tail, so that the probe/sample can reach the position of highest magnetic field. In this cryostat, liquid helium is stored in the center space and enclosed by liquid nitrogen or nitrogen shield and vacuum jacket, which significantly reduce heat leaking into the helium reservoir. In Fig 2-8, an optical probe is inserted into the liquid helium reservoir of this cryostat, and the sample inside the probe is cooled down by back filling low-pressure helium exchange gas into probe. Light is delivered to the sample through an optical fiber, and temperature of sample is measured with a Cernox temperature sensor and controlled with a heater mounted on sample mount.

In Fig. 2-9, the layout of a typical CW magneto-optical experiment setup at NHMFL is shown in a block diagram. An optical probe is inserted in the cryostat, which is positioned on the top of a Bitter magnet. A Lakeshore temperature controller controls the temperature of the sample via a sensor and heater co-located next to sample. The input light and output signal light are delivered to sample and spectrometer respectively through two optical fibers. In the case of transmission, reflection measurements, CW white light sources (Tungsten or Xenon lamps) are used for input illumination while lasers (He-Ne, He-Cd, Argon and Ti:Sapphire) are used as input excitation light for photoluminescence (PL) experiments. The transmission, reflection and PL signal light are collected with the output optical fiber mounted next to the sample and analyzed by a 0.75 m single-grating spectrometer (McPherson, Model 2075) equipped with single channel photon counting electronics PMT as well as a multi-channel CCD detector. All of the control units in this setup, including magnet controller, temperature controller, spectrometer controller, PMT and CCD controller are managed by an Apple computer through GPIB interfaces.

2.6 Development of Ultrafast Magneto-optical Spectroscopy at NHMFL

2.6.1 Introduction of Ultrafast Optics

With the existing CW magneto optical setup at NHMFL, many experiments have been done successfully. However, there is still a drawback of this experimental setup – time-resolved magneto-optical information can not be acquired due to large stretch effect of multimode optical fibers, which expand the pulse width of ultrafast laser pulse dramatically (from ~ 100 fs to ~ 20 ps) and results in a significant loss of time resolution. In order to obtain time-resolved magneto-spectroscopy in high magnetic fields, a new

facility needs to be developed, which includes a new magnet, cryostat, probe as well as new ultrafast light sources and detection methods.

2.6.2 Magnet and Cryogenics for Ultrafast Optics at NHMFL

Note that in a standard pump-probe experiment, while the excitation (pump) and probe pulses must be delivered to the sample through free space to preserve the temporal resolution, the collection of the light from the sample can be accomplished using standard fibers.

To preserve the temporal duration of a femtosecond laser pulse before it reaches the sample, direct optical propagation in free space is required. We also needed to modify current cryostat so that it can be used on resistive magnet for ultrafast magneto optical experiments. A technical drawing of modified optical cryostat is shown in Fig. 2-10. We mount an optical window on the bottom of outer tail of the cryostat, open the bottom of nitrogen shield, weld a copper sample mount right on the bottom of helium tail so that samples can be cooled down with a cold sample mount. For the collection of light after excitation of the sample, optical fibers positioned right on the top of sample are used to deliver transmission or PL to spectrometer or detector. With this configuration, the ultrafast laser pulse can reach the sample directly through resistive magnet bore and optical window, while the sample can still be as cold as 10K (for more details see appendix A).

In addition to resistive magnet, a superconducting magnet was also developed and commissioned by us to carry out magneto-optical experiments, especially for the ultrafast magneto-optics laboratory. We redesigned the cryostat for a 17 Tesla superconducting magnet such that femtosecond laser pulses can be steered into the center magnet bore and

excite sample directly at field center. Fig 2-11 shows the section view of this superconducting magnet. There is a stainless steel center bore welded on the cryostat and going through the center of magnet. This bore isolates the sample chamber and helium reservoir, which make it possible to do direct optics with this superconducting magnet. The cold stainless steel bore is sealed with an optical window on the bottom and a specially designed probe loading system on the top, shown in Fig. 2-12. With this probe loading system, we can change sample without causing air leak into the center bore merged in liquid helium. The sample on probe is cooled down with backfilling low-pressure helium exchange gas in the center bore.

2.6.3 Ultrafast Light Sources

In addition to the development of cryogenics and magnet system, we also set up several femtosecond pulse laser systems for time resolved magneto-spectroscopy. These ultrafast laser systems include a Ti:Sapphire femtosecond oscillator, a Ti: Sapphire chirped pulse amplifier (CPA) and an optical parametric amplifier (OPA).

2.6.3.1 Ti:Sapphire femtosecond oscillator

Fig. 2-13 shows the schematic diagram of Coherent Mira 900 F femtosecond laser system. In this laser system, a prism pair compensates dispersion caused by broad bandwidth of laser emission. This passive mode locking ultrafast oscillator laser acquires self-mode locking with Kerr Lens effect, and the shaker in the cavity works as a trigger to initiate the mode locking. The pulse width of this ultrafast laser oscillator is around 150fs and the energy per laser pulse is around 4nJ. This laser is tunable from 700 to 900 nm and runs at 76MHz repetition rate. We use this ultrafast laser to get second harmonic

generation from BBO nonlinear crystal and carry out degenerate pump probe experiments on ZnO semiconductors as described in Chapter 6.

2.6.3.2 Chirped pulse amplifier

In many optical experiments, strong ultrafast laser pulses (up to mJ per pulse) are needed for either nonlinear effect like self phase modulation (white light generation) and parametric amplification or for high carrier density generation in samples. Most of our experiments were done with the Clark-MXR 2001 CPA. However, because of reliability problems the Clark –MXR laser was later replaced by the Coherent laser in early 2007.

The current Coherent Legend-F chirped pulse amplifier (CPA) is set up in cell 3 at DC facility for research in ultrafast magneto optics. Fig. 2-14 shows the schematic diagram of this CPA femtosecond laser system. This CPA itself consists of three basic components: a pulse stretcher, a regenerative amplifier cavity, and a pulse compressor (see Fig.2-14). There are two external lasers for this CPA system, a Coherent Vitesse oscillator (similar to the Mira described above), which generates a high repetition rate ultrafast seed pulse train for amplification and an Evolution, which is a Q switch laser used to pump Ti:Sapphire crystal inside regenerative amplifier cavity at a variable (but typically 1 kHz) repetition rate with a 10mJ pulse. This CPA system functions in the following manner. First, a 150 fs seed pulse train is generated in Vitesse laser and sent into pulse stretcher. This seed pulse is stretched to approximately 100 ps, so that it will not destroy the Ti:Sapphire crystal in regencavity as it get amplified. A Pockel cell (PC1 in Fig. 2-14) then picks off one pulse from the train within the regenerative amplifier cavity for amplification. The pulse undergoes several roundtrips within the cavity and through the Ti:Sapphire crystal which is prepumped with the Evolution laser and

experiences a total gain of approximately 10^6 . Once the amplification of seed pulse reaches its maximum (around 2 mJ per pulse), it is switched out of the regencavity by a second Pockel cell (PC2 in Fig. 2-14) within the cavity. Finally, the amplified pulse propagates through a grating compressor (see Fig.2-14) to compress the pulsewidth back down to 150fs. At the output, we obtain 150fs laser pulses at a 1 kHz repetition rate and 2 mJ per pulse from this CPA system. As we discuss in Chapter 5, this laser is used to study PL from high density of carriers in $\text{In}_x\text{Ga}_{1-x}\text{As}/\text{GaAs}$ MQW in high magnetic field.

2.6.3.3 Optical parametric amplifier

The Ti:Sapphire oscillator and CPA laser can provide us with ultrafast pulse, however, their wavelength ranges are limited. Therefore, an optical parametric amplifier (OPA) is required to convert light to different wavelengths while preserving the short duration of the pulses. Fig.2-15 shows the layout of a Quantronix OPA laser. This is a five pass system in total. The first three passes of the pulse occur through a beta barium borate (BBO) nonlinear optical crystal for frequency conversion, and a signal pulse (at frequency ω_{signal}) and idler pulse (at frequency ω_{idler}) are generated. In the forth and fifth passes through the BBO crystal, signal and idler pulse are parametrically amplified with a fraction of CPA pulse. The relation between fundamental CPA, signal and idler pulse is given by

$$\omega_{CPA} = \omega_{\text{signal}} + \omega_{\text{idler}} . \quad 2-17$$

After parametric amplification by CPA pulse, the signal and idler pulses are then used to generated ultrafast pulses at different wavelength through second harmonic generation (SHG), $\omega=2\omega_{\text{signal}}$ or $2\omega_{\text{idler}}$, fourth harmonic generation (FHG), $\omega=4\omega_{\text{signal}}$ or $4\omega_{\text{idler}}$, and different frequency mixing (DFG),

$$\omega_{CPA} = \omega_{signal} - \omega_{idler} .$$

2-18

The five nonlinearly optical processes mentioned above cover wavelength range from 300 nm to 20 μm .

2.6.3.4 Streak camera

In many cases, time-resolved photoluminescence is a very important method to study the carrier dynamics since it provides a direct measurement of the radiative emission of photons as carriers recombine in semiconductors. A picosecond streak camera is the proper device to measure time resolved photoluminescence. Fig. 2-16 shows the operation principle of a streak camera. We are currently setting up a Hamamatsu Streak Camera at the NHMFL ultrafast facility. In Fig.2-11 we can see that conceptually, a PL pulse generated after excitation of a sample is steered into the slit and then focused on a photocathode, where it is converted into an electron pulse of the same duration. The electron pulse is then accelerated and passes through a very fast sweep electrode, which is synchronized with the PL pulse, so that electrons at slightly different time will be deflected at different angle by the AC high voltage and hit the CCD at different position. Using this method, the temporal profile of a PL pulse is spatially mapped on CCD in a spatial profile. By placing a spectrometer at the front end of the streak camera, the PL can be spectrally and temporally resolved.

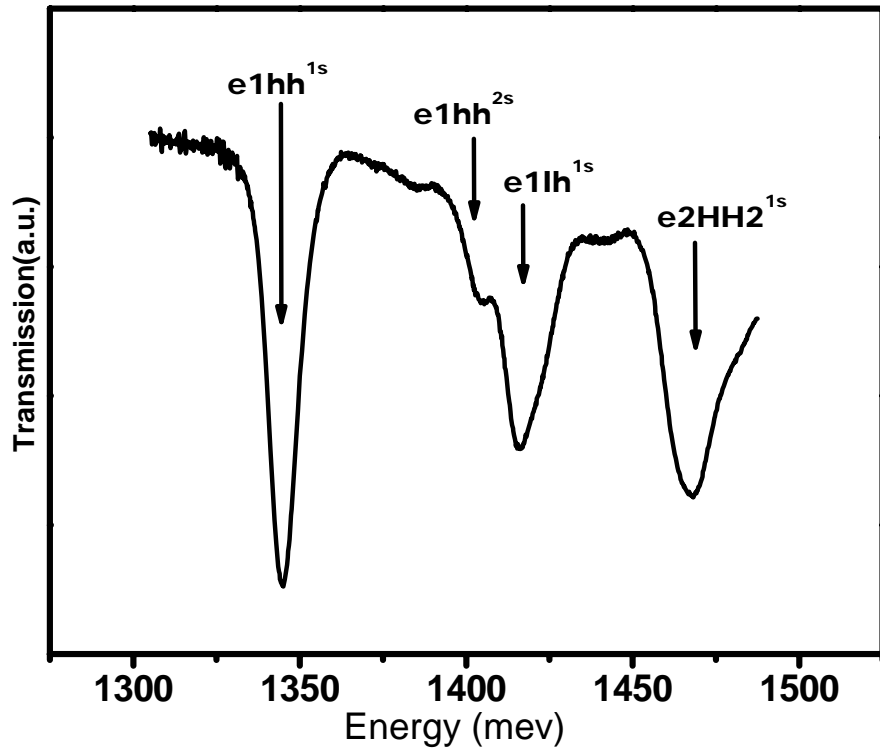


Figure 2-1. Transmission spectrum of InGaAs/GaAs MQW at 30 T and 4.2 K. The energy position of each dip on transmission curve is correspondent to a magneto exciton state. Magneto-excitonic states are labeled according to the convention presented in Chapter 3.

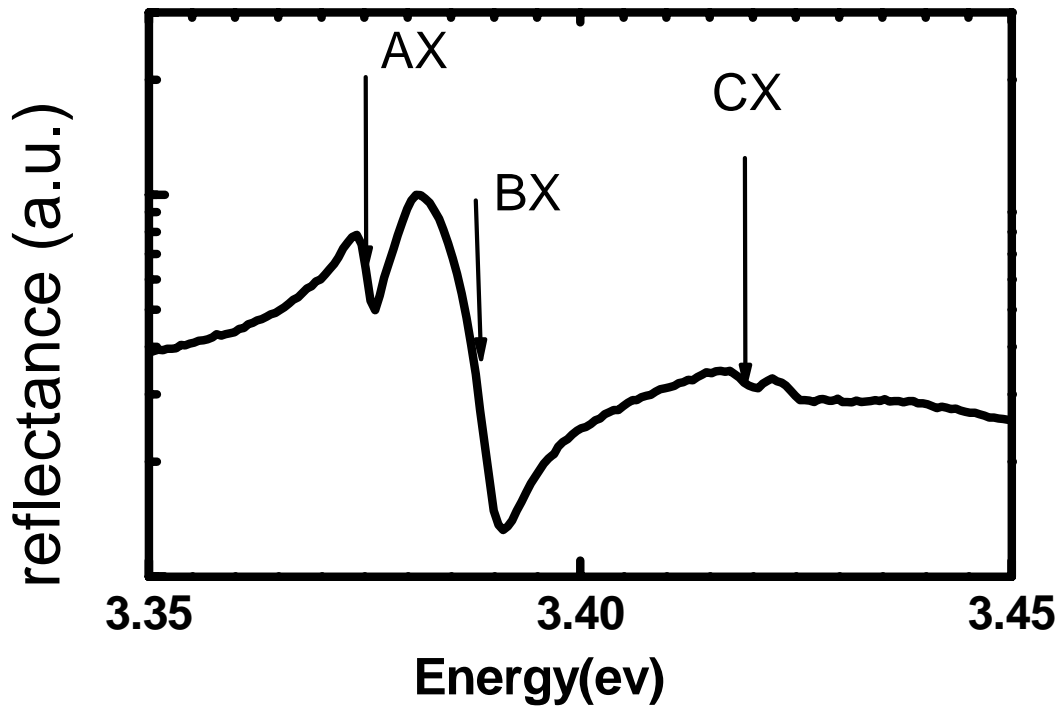
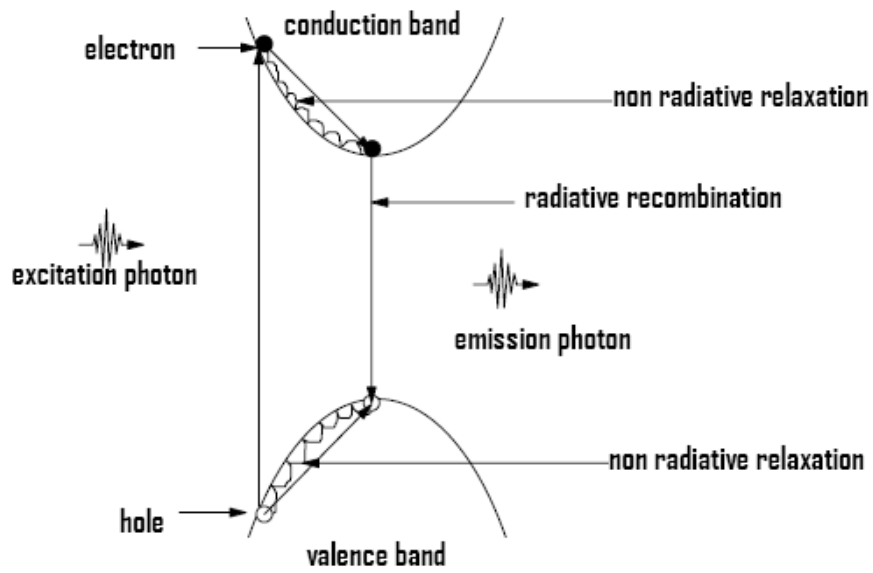
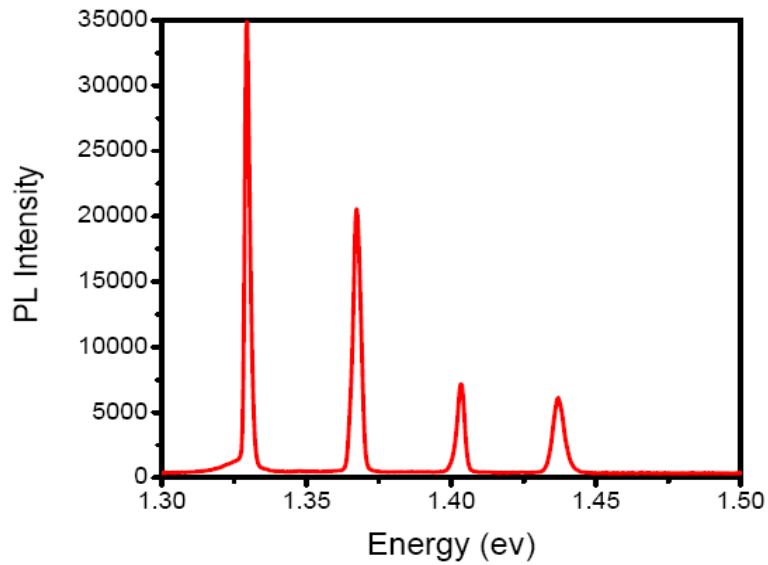


Figure 2-2. Reflection spectrum of ZnO epilayer at 4.2K. Excitonic states and their symmetry are labeled. In the reflection spectrum, the approximate position of an excitonic state is marked with an arrow, which is the middle point between a dip and the peak next to it on the low energy side. on the reflectance curve. This spectrum will be discussed further in Chapter 5.



(a)



(b)

Figure 2-3. e-h recombination process and photoluminescence spectrum in semiconductors. (a) Illustration of Photon induced photoluminescence in a direct bandgap semiconductor, (b) PL of InGaAs/GaAs MQW in high magnetic field 30Tesla excited with an intense femtosecond laser pulse.

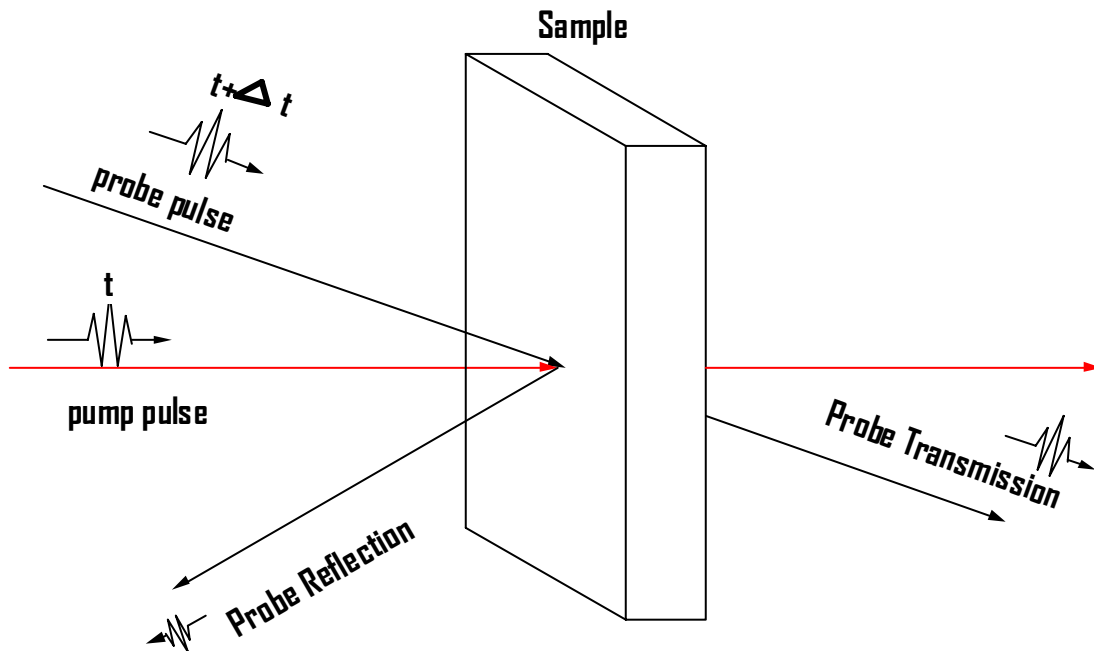
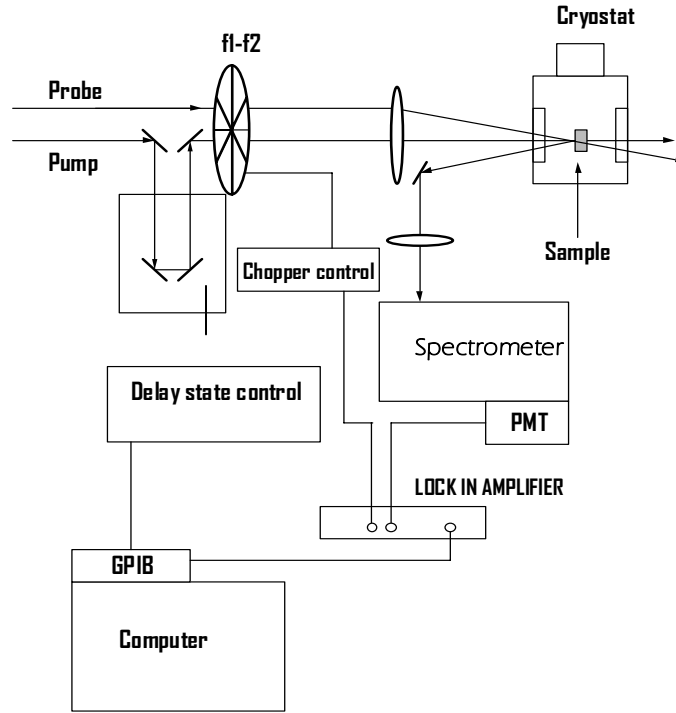
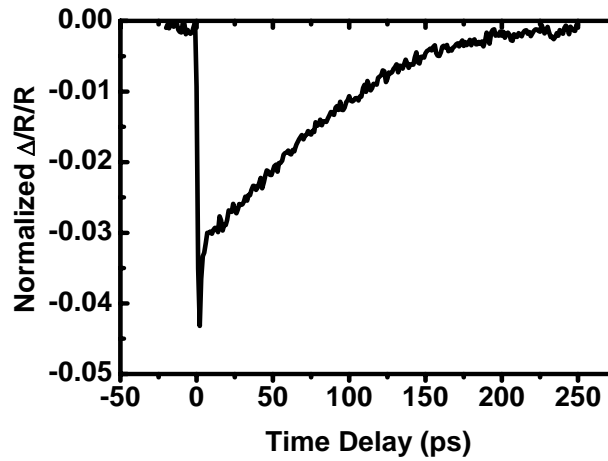


Figure 2-4. Simple illustration of optical pump-probe transient absorption or reflection experiment. Both pump and probe are from pulsed laser and spatially overlapped on the sample. The time delay between pump and probe is Δt . Either the transmission or reflection of probe light is detected. By changing the delay between pump and probe pulse, time resolved transmission or reflection spectrum can be obtained.



(a)



(b)

Figure 2-5. Experimental setup for optical pump-probe spectroscopy and TRDR spectrum of ZnO. (a) Pump probe experimental setup for spectrum resolved time differential reflectivity. Pump and probe are modulated with frequency f_1 and f_2 respectively, a lock-in amplified is used to acquire the transient reflection signal; (b) Time resolved differential reflectivity of ZnO epilayer at 4.2K. Details will be discussed in Chapter 6.

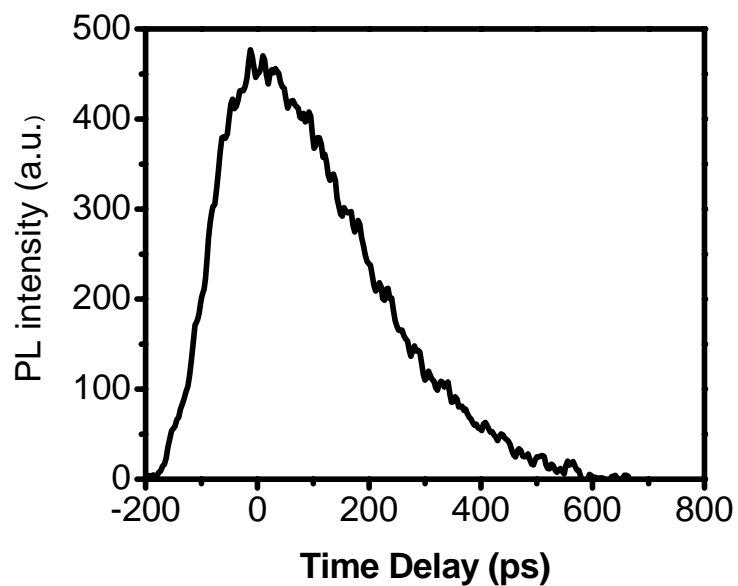


Figure 2-6. Time resolved photoluminescence spectrum of In_xGa_{1-x}As/AlGaAs MQW at 4.2K taken with a Hamamatsu Streak camera. Time resolution is around 5ps.

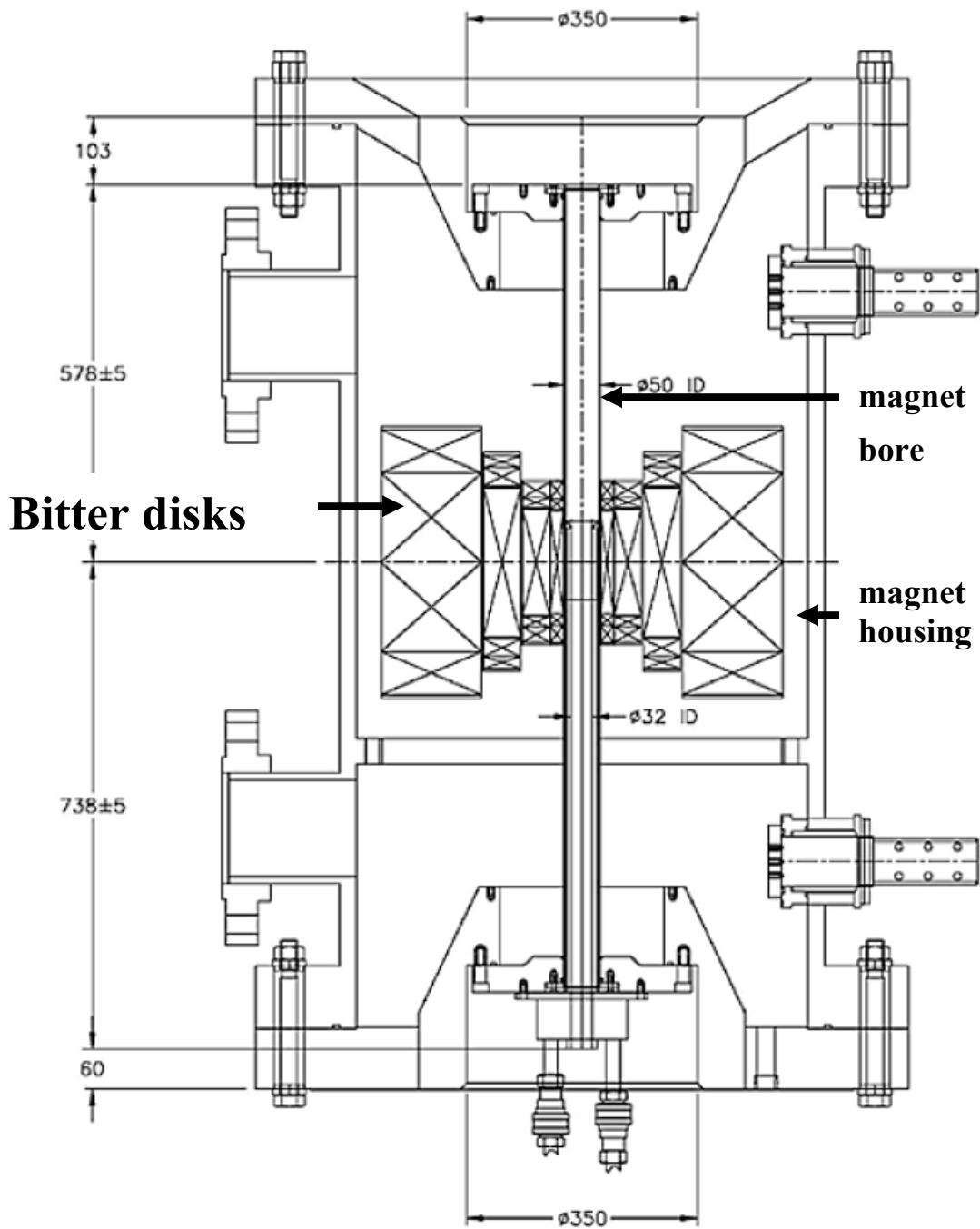


Figure 2-7. Technical drawing of the 30 Tesla resistive magnet in cell 5 at NHMFL. From National High Magnetic Field Laboratory, www.magnet.fsu.edu, side view of 31T / 32mm Resistive Magnet with Gradient Coil (Cell 5), date last accessed September, 2007

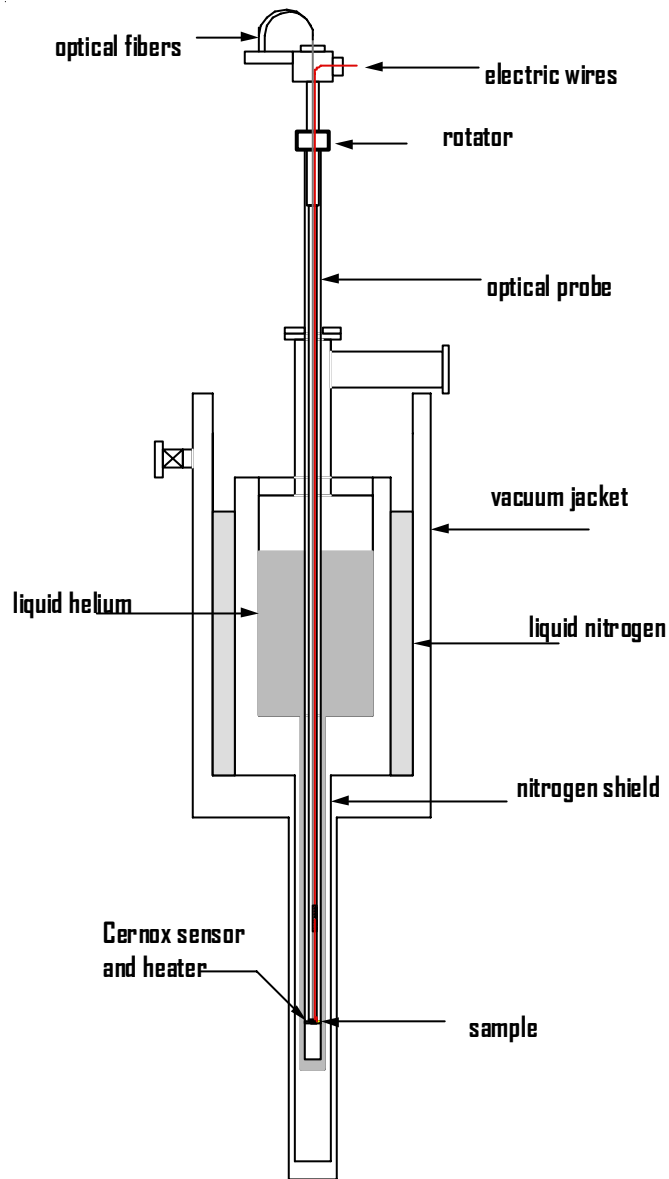


Figure 2-8. Cryostat and optical probe for CW optical spectroscopy at NHMFL. The cryostat has vacuum jacket and liquid nitrogen space for thermal isolation. An optical probe is inserted in the liquid helium (LHe) of the cryostat, sample on the end of the probe is cooled down with He exchange gas, the input light and output light are delivered through multimode optical fibers.

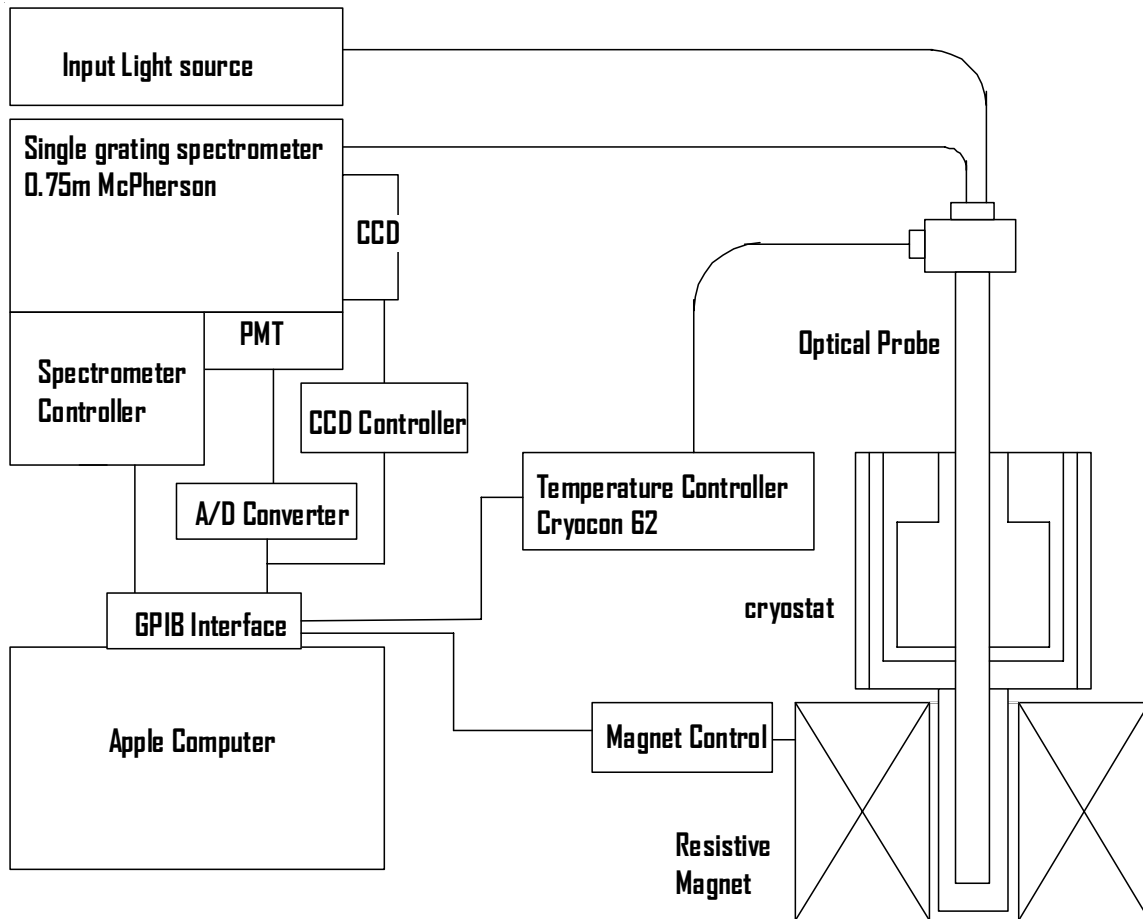


Figure 2-9. CW magneto optical experiment setup at the NHMFL. Input light is delivered to sample in optical probe through fiber, the sample is mounted on an optical probe, positioned at the field center and cooled down with LHe, the output light from sample is sent to a spectrometer and the spectrum is recorded with CCD or PMT. The magnet control and spectrum acquisition from spectrometer is computerized with GPIB interface.

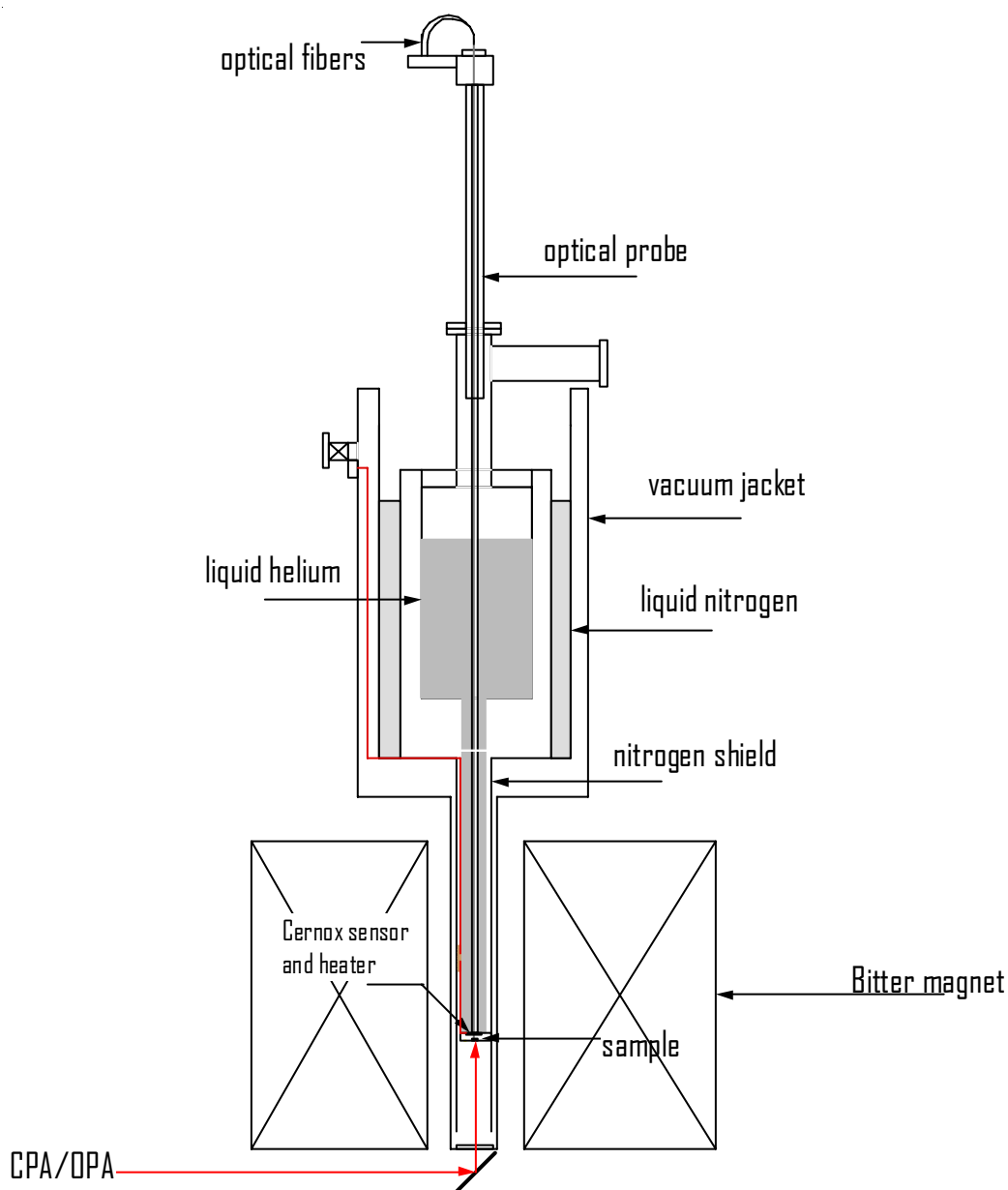


Figure 2-10. Modified magneto optical cryostat for direct ultrafast optics. The optical cryostat is positioned on the top of a resistive magnet and the sample is right at the field center. A sample mount is attached directly on the LHe tail of the cryostat, so that the sample can be cooled down. An optical window is mounted on the bottom of the outer tail of the cryostat, through which the ultrafast laser can reach the sample without being stretched significantly. The PL or probe light is delivered to detector and spectrometer through optical fiber.

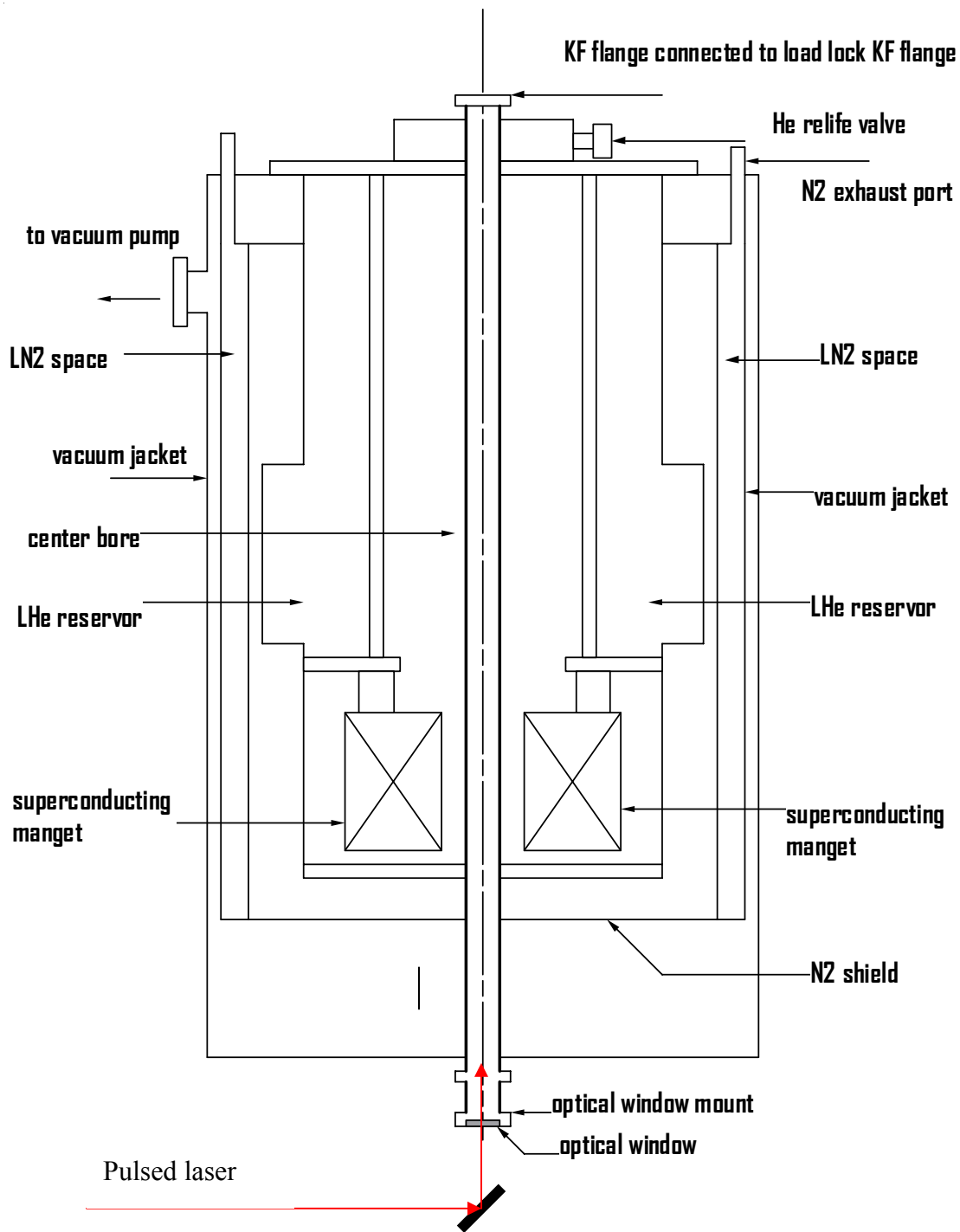


Figure 2-11. Technical drawing of the 17 Tesla superconducting magnet SCM3 in cell 3 at NHMFL. Stainless steel tubing is used as the center bore of this magnet, an optical window is mounted on the bottom of the tubing, samples on probe are positioned in the center tubing. Ultrafast laser is steered in to the bore and excites samples without being stretched much.

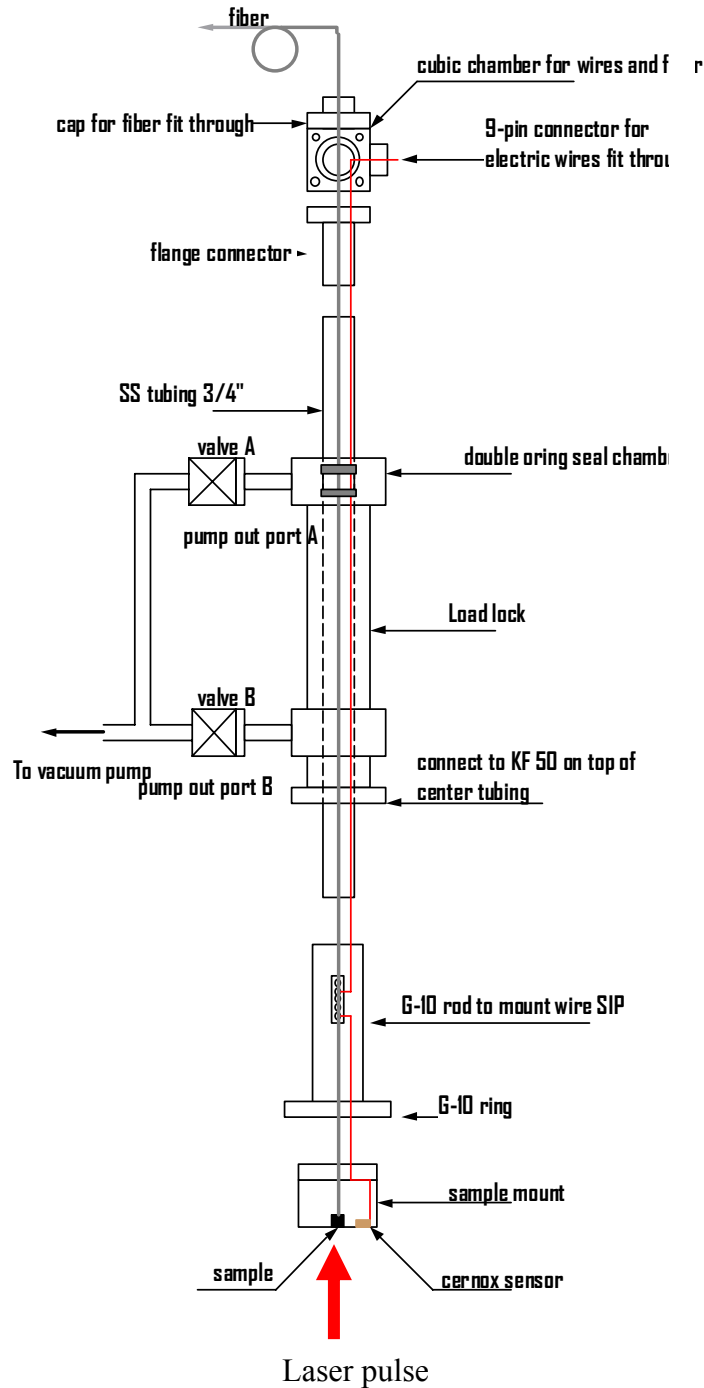


Figure 2-12. Technical drawing of the special optical probe designed for superconducting magnet 3 in cell 3 at the NHMFL. A load lock system is attached on the top part of this probe, the vacuum in the center bore of the magnet is not broken when loading and removing the probe from the cold magnet bore. Temperature of the sample is controlled with a Cernox sensor and electric heater. Ultrafast laser can reach the sample directly and the PL or probe light from sample is delivered outside with fibers.

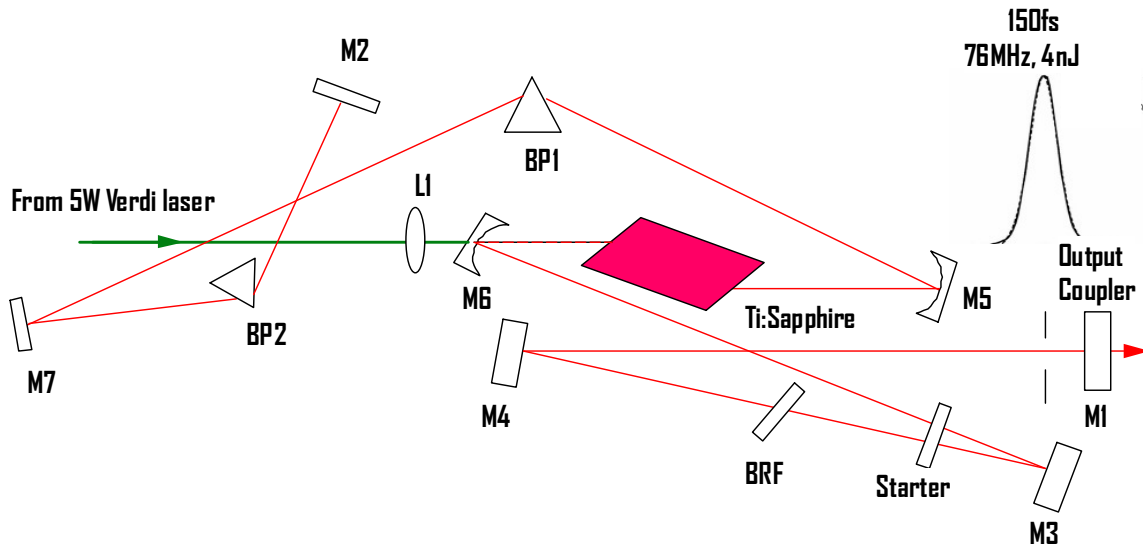


Figure 2-13. Coherent Mira 900F femtosecond laser oscillator. BP1 and BP2 is a Bruster prism pair, M1 and M7 are cavity mirrors, BRF is birefringe filter, M5 M7 are spherical mirrors, M2, M3 and M6 are mirrors, L1 is a lens.

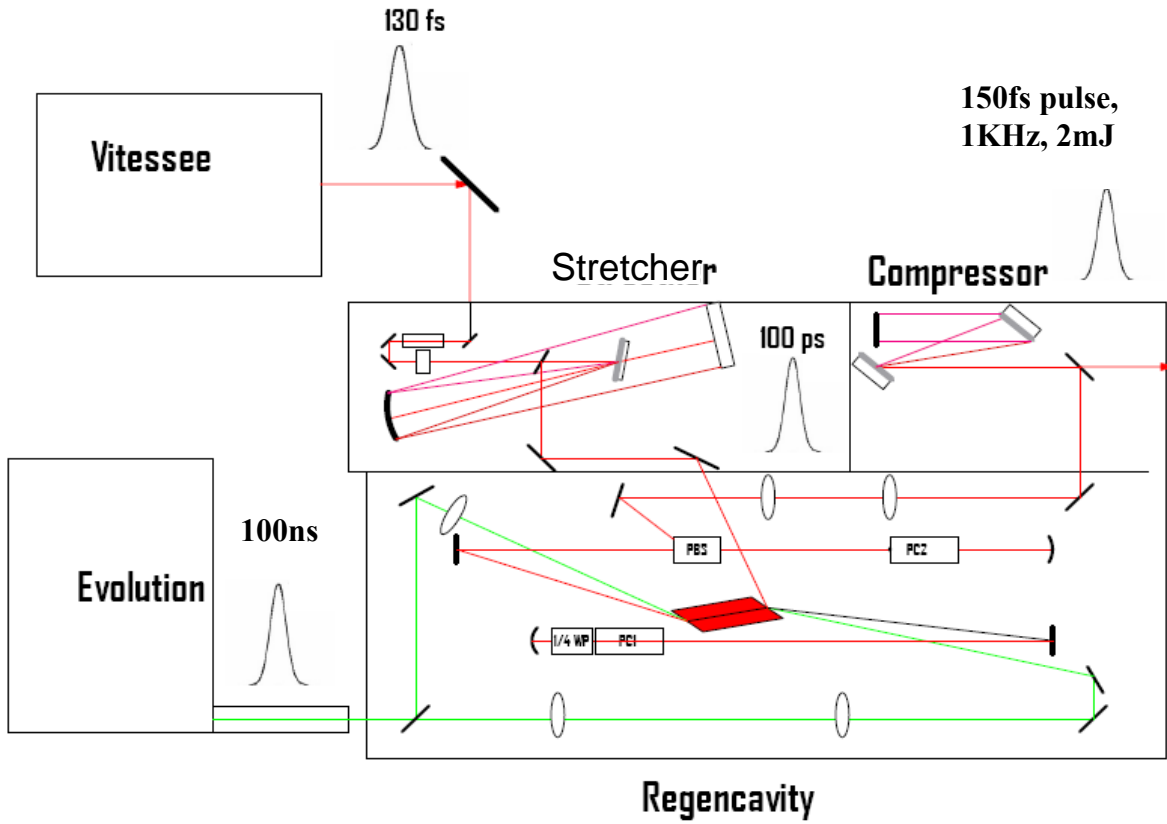


Figure 2-14. Coherent Legendre-F chirped pulse amplifier (CPA). PC is pockell cell, wp is waveplate.

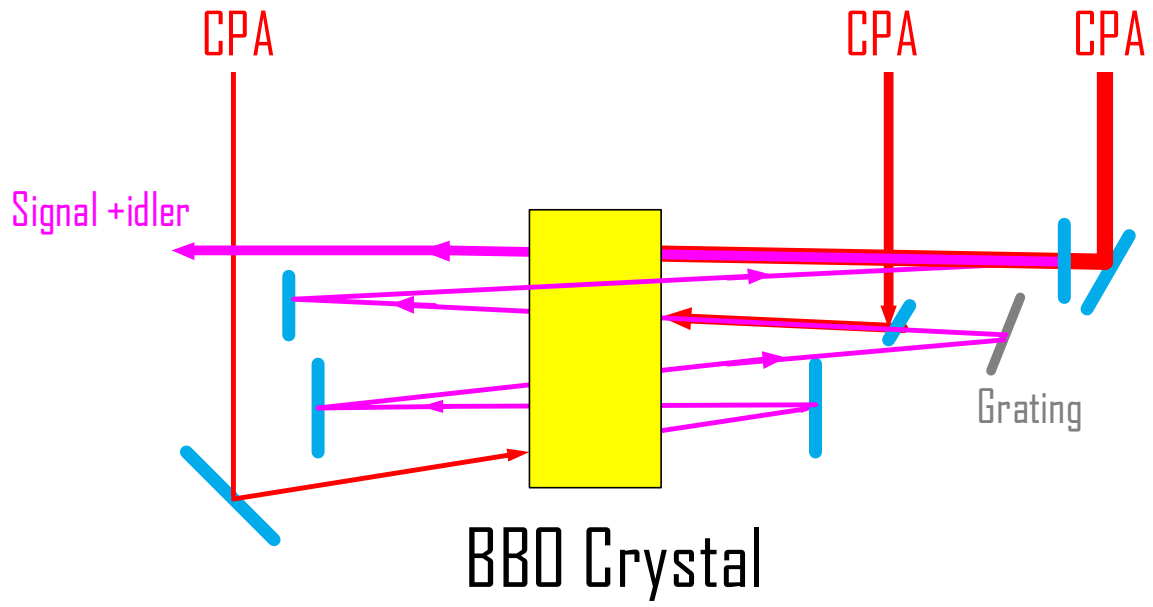


Figure. 2-15. Top view of the optical elements and beam path in TOPAS OPA.

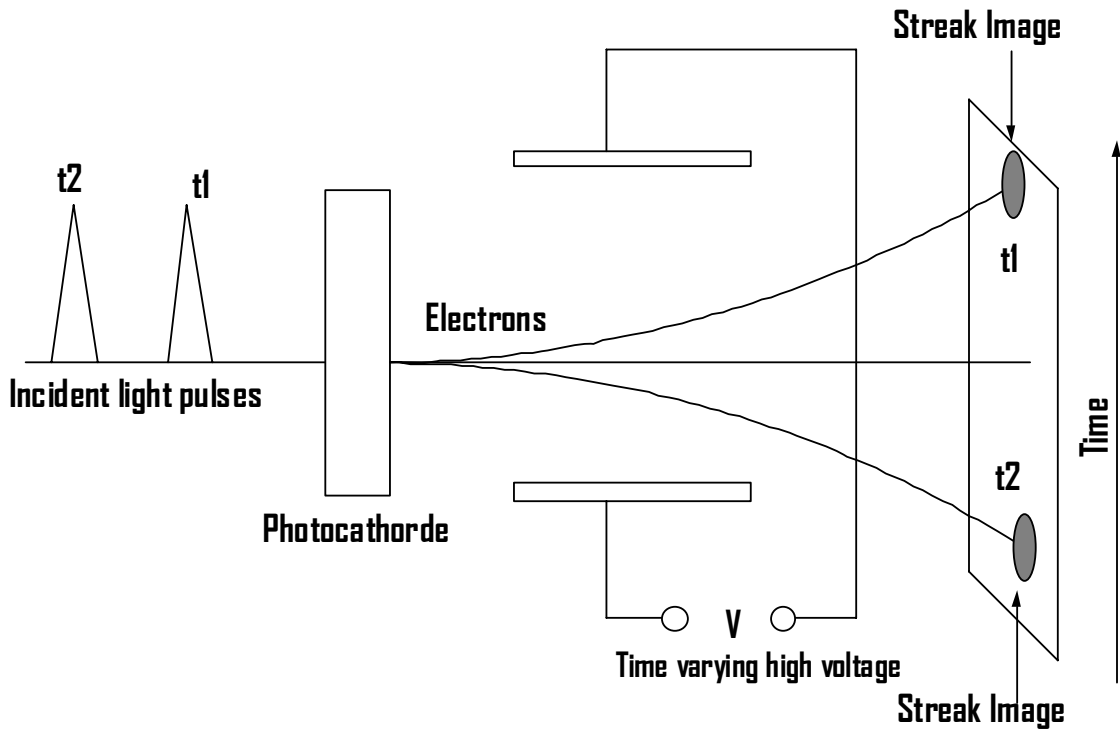


Figure 2-16. Operation principle of a streak camera. The photocathode converts light pulse t_1 and t_2 into two electron pulses, the two electron pulses have different positions for streak images because the high voltage bias is time varying.

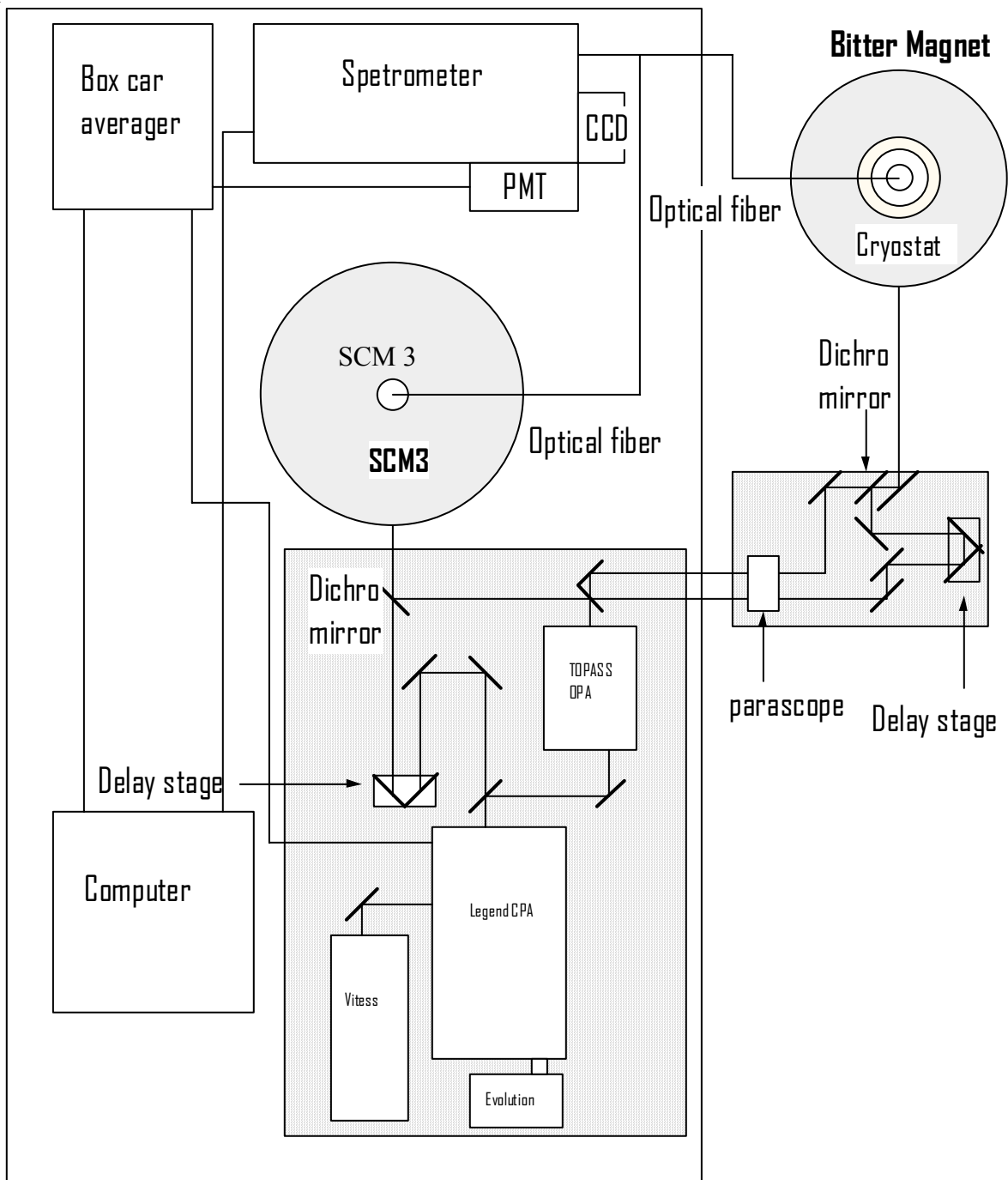


Figure 2-17. Ultrafast optics experimental setup in cell 3 and 5 at NHMFL.

CHAPTER 3 ELECTRONIC STATES OF SEMICONDUCTOR QUANTUM WELL IN MAGNETIC FIELD

3.1 Introduction

This chapter provides a background in the physics and optics of quantum confinement induced by structural modifications (quantum wells) and strong magnetic fields. Optical and electrical transport properties of semiconductor materials are determined by their electronic states. A background in the fundamental band theory of semiconductors is necessary to understand the magneto optical spectroscopy, specifically, of $\text{In}_x\text{Ga}_{1-x}\text{As}/\text{GaAs}$ multiple quantum wells, a typical III-V group semiconductor material, and ZnO (bulk, epilayer and nanorod), typical II-VI group semiconductor material. Band structures of Wurzite symmetry (C_{6v}) ZnO and Zincblende symmetry (T_d) $\text{In}_x\text{Ga}_{1-x}\text{As}$ semiconductors are introduced.

In semiconductor quantum wells, carriers are confined in the two dimensions defined by the barriers, and the electronic states have new characteristics with respect to bulk materials due to quantum confinement. The exciton effect, energy states due to quantum confinement and selection rules of optical transitions in quantum well are given in detail in this chapter.

In a high magnetic field oriented perpendicular to the plane of the quantum wells, further confinement is introduced to a semiconductor quantum well, and the basic theory of magneto optical process of semiconductor quantum well is given to understand the optical processes related with interband Landau level transitions. Also, the density state of 3D, 2D and 1D systems are given in this chapter.

3.2 Band Structure of Wurzite and Zinc Blend Structure Bulk Semiconductors

In a crystalline solid with N atoms, the electronic states of the N electrons make up continuous energy bands separated by finite width band gaps. In a crystal, the electron

wavefunction and periodic potential of this crystal remain unchanged under translational symmetry $R(l, m, n)$, which can be described by the three primitive vectors: \mathbf{a} , \mathbf{b} and \mathbf{c} as

$$R(l, m, n) = la + mb + nc,$$

l, m, n are integers. Because of the translational symmetry, the electronic wave functions in a crystal can be described with “Bloch function” [40]

$$\Psi_{v\mathbf{k}}(\vec{r}) = \frac{1}{\sqrt{N}} e^{i\mathbf{k}\cdot\vec{r}} u_{v\mathbf{k}}(\vec{r}), \quad 3-1$$

v is the index of an electron energy band, \mathbf{k} is a reciprocal lattice vector, N is the total number of primitive cell unit in the crystal and u is a periodic function inside a primitive cell and has translational symmetry

$$u_{v\mathbf{k}}(\vec{r} + \mathbf{R}) = u_{v\mathbf{k}}(\vec{r}). \quad 3-2$$

In equation 3-1, the Bloch function $\Psi_{v\mathbf{k}}$ is normalized over the whole crystal and in Eq. 3-2, $u_{v\mathbf{k}}(\vec{r})$ is a function normalized over the volume of a unit cell. The value of \mathbf{k} is limited to the Wigner-Seitz cell in reciprocal space, which is called “Brillouin Zone”.

Semiconductors are also a kind of solid crystal, which has a finite band gap between the highest and fully occupied valence band and a lowest partially occupied (doped) or totally unoccupied (undoped) conduction band. The band gap values and band structure of semiconductors, which determine many optical and transport properties, are very important parameters. The band gaps of semiconductors vary from near infrared (InAs 0.43eV) to ultraviolet (ZnO 3.40eV). Among most of the III-V group semiconductors such as GaAs and InAs, the typical structure is zinc-blende, while for the II-VI group semiconductors like GaN and ZnO, the most common structure is the Wurzite structure.

In semiconductors, the Hamiltonian of an electron can be described as [71]:

$$H = \frac{\hbar^2 k^2}{2m^*} + V(\vec{r}) + H_{so} + H_{crystal} \quad 3-3$$

where \mathbf{k} is the momentum of electron, m^* is electron effective mass, $V(r)$ is periodic potential in semiconductor crystal, H_{so} is the spin and orbit interaction, and $H_{crystal}$ is the interaction between electron and crystal field in an unit cell. Compared to the first two terms, the later two are relatively small and can be treated as perturbation.

As the prototypical direct gap semiconductor, the first Brillouin zone and band structure of GaAs (fcc structure) are given in Fig.3-1 (a). (We will be working with $\text{In}_{0.2}\text{Ga}_{0.8}\text{As}$ in this disseration, but the descriptions given for GaAs are applicable since GaAs and InAs have same crystal structure.) At the center of the Brillouin zone, the point is labeled as Γ point (0, 0, 0). X (1, 0, 0) on k_y axis, and L (1/2, 1/2, 1/2) are also the fundamental points. The calculated electronic band structure of bulk GaAs is shown in Fig. 3-1 (b). The conduction band in GaAs has absolute minimum value at the Γ -point and two local minima at the L-point and X-point, which are referred as L valley and X valley. The conduction band of GaAs does not split since it is a s-like nondegenerate band, while the valence band split into three bands: heavy-hole, light-hole and split-off bands since they are p-like three folds degenerate [71]. The degeneracy between split-off ($J=1/2$) and heavy-hole and light-hole ($J=3/2$) is lifted due to the interaction (H_{so}) between electron spin ($s=\pm 1/2$) and angular momentum ($l=\pm 1$ for p-like electron). However, at the Γ -point, the degeneracies of light-hole and heavy-hole subbands are not lifted because of the high cubic symmetry (T_d point group) of the GaAs cell ($H_{crystal}=0$).

In a Wurzite structure semiconductor such as GaN and ZnO, the first Brillouin zone and bandstructure are quite different from the zinc-blende structure. Fig 3-2 (a) and (b) present the first Brillouin zone and band structure of a zinc-blende structure GaN semiconductor. At the Γ -point, the valence band of Wurzite structure semiconductors split into three subbands (heavy

hole, light hole, and split-off) due to the hexagonal (C_{6v} point group) symmetry of GaN crystal cell, which gives an additional perturbation part of $H_{\text{crystal}} \neq 0$ and lifts the degeneracy.

In the optical transitions in semiconductors, a photon is either absorbed or emitted. This is based on electron transitions between the top of valence band and bottom of conduction band. The selection rule for this optical transition is $\Delta k = 0$, which expresses the momentum conservation of crystal. Compared to the crystal momentum, the momentum of photon is very small and can be neglected.

For direct bandgap semiconductors such as GaAs and ZnO, the valence band absolute maximum and the conduction band absolute minimum occur at Γ -point, the center of Brillouin zone, where interband and intraband (inter-subband) transitions are observed without phonon emission. The optical transitions from other valley (X or L valley) in conduction band to Γ -point of the valence band must be accompanied by the emission of a phonon to conserve the crystal momentum.

3.3 Selection Rules

In Kane model [72], since in all the II-VI and III-V group semiconductors the chemical bond are formed with outer shell electrons $nsnp$, the wave functions of hybridized s -like band and p -like bands can be represented using 8 band edge Bloch functions (u_0, u_1, \dots, u_8) $|S\uparrow\rangle, |X\uparrow\rangle, |Y\uparrow\rangle, |Z\uparrow\rangle$ and $|S\downarrow\rangle, |X\downarrow\rangle, |Y\downarrow\rangle, |Z\downarrow\rangle$. However, after the spin orbit interaction H_{so} is considered, a new linear combination of these functions can be formed. In the new functions, $\mathbf{J}=\mathbf{L}+\mathbf{S}$ and J_z are good quantum numbers and H can be diagonalized. The new Bloch functions basis set [71] is given in Table 3-1. They are taken as a basis set in a Kane model calculation [72].

The optical transitions between conduction band and valence band due to electro dipole transitions in semiconductor are described by the transition matrix element [71]

$$M_{if} = \int \Psi_f^* \hat{\varepsilon} \cdot \vec{p} \Psi_i d\vec{r} \quad . \quad 3-4$$

where $\hat{\varepsilon}$ is the optical polarization unit vector and \vec{p} is the electron momentum operator. Using the Bloch functions (Eq. 3-2), M_{if} can be expressed approximately as [71]:

$$M_{if} = \hat{\varepsilon} \cdot \langle u_{vf} | \vec{p} | u_{vi} \rangle \cdot \int f_f^* f_i \cdot d\vec{r} + \hat{\varepsilon} \cdot \langle u_{vf} | u_{vi} \rangle \int f_f^* \vec{p} f_i \cdot d\vec{r}, \quad 3-5$$

where u_{vf} and u_{vi} are the wave functions for the initial and final state(see Eq.3-1),

$f = \frac{1}{\sqrt{N}} \exp(i\vec{k} \cdot \vec{r})$ is the envelop function and $\langle u_{vf} | u_{vi} \rangle = \delta_{vf,vi}$, the transition matrix is mainly

determined by first term in Eq.3-5.

The absolute values of the transition matrix elements $\langle S | \hat{\varepsilon} \cdot \vec{p} | u_n \rangle$ are listed in table 3-2, where S is the conduction band wavefunction and u_n is the valence band wavefunction, x, y, and z are the propagation direction of light, ε_x , ε_y and ε_z are light polarization

$$\text{and } P = \frac{-i}{m_e} \langle S | p_x | X \rangle = \frac{-i}{m_e} \langle S | p_y | Y \rangle = \frac{-i}{m_e} \langle S | p_z | Z \rangle.$$

3.4 Quantum Well Confinement

In this thesis, we have focused our study on type I quantum well structure described in chapter 1. The Bloch wave function of an electron or hole confined in the quantum well with periodic potential $V(z)$ is described as [41]

$$\Psi_{\nu\kappa} = e^{i\vec{k} \cdot \vec{r}_\perp} \chi(z) u_{\nu\kappa}(\vec{r}), \quad 3-6$$

here k is the electron wave vector in xy -plane and $\chi(z)$ is an envelop function along the z direction, in which the quantum well is grown. We can separate the wave function (Eq. 3-6) into xy and z directions. In the z direction, we have

$$\left(-\frac{i\hbar^2}{2m^*} \frac{d^2}{dz^2} + V(z) \right) \chi(z) = E_n \chi(z). \quad 3-7$$

The eigenvalues E_n of this equation 3-7 are the energies of different quantum confined subbands. A schematic diagram of the confinement subbands in a type I quantum well is shown in figure 3-3.

For the states in the xy plane, if we use parabolic bands for k_x and k_y , the carrier energies in the quantum wells are given by:

$$E = E_n + \frac{\hbar^2}{2m^*} (k_x^2 + k_y^2). \quad 3-8$$

The Bloch wave function (Eq. 3-6) for a quantum state labeled by n can be expressed as

$$\Psi_n = u_n^v f_n = u_n^v \chi(z) e^{i\vec{k} \cdot \vec{r}_\perp},$$

here, \vec{k} and \vec{r}_\perp are the 2D electron wave vector and position vectors in the xy -plane.

With the envelope functions $\chi(z)$, we can derive the selection rules of the envelope function from equation 3-5,

$$\langle f_f | f_i \rangle = \int e^{i(k^i - k^f)} dr_\perp \int \chi_n^*(z) \chi_m(z) dz. \quad 3-9$$

The first term shows that the optical transition is allowed when the electron momentum k is conserved

$$k^f = k^i.$$

The second term gives us the selection rule for transition between two different subbands [41]

$n-m=even.$

However, the transitions corresponding to $n-m=0$ are far stronger than $n-m=2, 4, 6, \dots$ [41]. The optical transitions processes correspondent to $n-m=0$ are shown in Fig. 3-3.

3.5 Density of States in Bulk Semiconductor and Semiconductor Nanostructures

A consideration of the density of states is very important for understanding the optical response of semiconductors. It expresses how many states are available in the system in the energy interval between ε and $\varepsilon+d\varepsilon$; the maximum number of carriers is reached when all the density of states is occupied up to Fermi level. This will become particularly important for understanding the superfluorescence experiments in Chapter 5. The density of states in a bulk semiconductor is given as [41]

$$g^{3D}(\varepsilon) = \frac{1}{2\pi^2} \left(\frac{2m_0^*}{\hbar^2} \right)^{3/2} \varepsilon^{1/2}. \quad 3-10a$$

In a 2D semiconductor quantum well, the carriers are confined within the well width, so the density of states is described as [41]:

$$g^{2D}(\varepsilon) = \frac{m}{\pi\hbar^2} \sum_j \theta(\varepsilon - \varepsilon_{j0}). \quad j=1, 2, 3, \dots \quad 3-10b$$

Here, j is the index of quantum confined states and $\theta(\varepsilon - \varepsilon_j)$ is the step function.

For a 1D system, the density of states is given by [41]:

$$g^{1D}(\varepsilon) = \frac{1}{\pi} \left(\frac{m_r}{2\hbar^2} \right)^{1/2} \sum_{j_x, j_z} \frac{1}{\sqrt{\varepsilon - \varepsilon_{j_x} - \varepsilon_{j_z}}}. \quad 3-10c$$

Here, j_x and j_z are index of quantum confinement states on z and x direction.

If all the 3 dimensions are quantum-confined for a free carrier, we have a quasi 0D system, and the zero dimensional carrier density of states is given by [41]

$$g^{0D}(\varepsilon) = 2 \sum_j \delta(\varepsilon - \varepsilon_j). \quad 3-10d$$

Here, ε_j is the energy of the j th quantum confinement state and $\delta(\varepsilon - \varepsilon_j)$ is the Dirac delta function.

The density of states curves for 3D, 2D, 1D and 0D system are plotted in Fig.3-4. We can see that for 3D and 2D systems, the density of states is continuous, while in 1D and 0D, the continuums collapse and the density of state get discrete and turn into δ function.

3.6 Magnetic Field Effect on 2D Electron Hole Gas in Semiconductor Quantum Well

In a type I semiconductor quantum well such as $\text{In}_x\text{GaAs}_{1-x}/\text{GaAs}$, electrons and holes are confined in a potential well defined by the xy -plane. In the presence of magnetic field along the z direction, an additional quantum confinement is applied to the electrons and holes in the xy -plane. The Hamiltonian of an electron in a quantum well in the presence of magnetic field along z direction is given by [71]

$$H = \frac{1}{2m} \left(\vec{p} - \frac{e\vec{A}}{c} \right)^2 + V(z), \quad 3-11$$

where $\vec{A} = (0, xB, 0)$ is the vector potential and $V(z)$ is the quantum well confinement potential.

We can separate the electron wave function into xy -plane component and z direction component, so the wavefunction Ψ can be written in the form

$$\Psi(x, y, z) = h(x, y)f(z).$$

Using this wave function, the Schrödinger equation can be separated in two independent equations:

(I) In z -direction (QW growth direction), we have

$$\left(-\frac{\hbar^2}{2m^*} \frac{d^2}{dz^2} + V(z) \right) f(z) = E_n f(z). \quad 3-12$$

This is referred to type I semiconductor quantum well confinement and discussed earlier (see Eqs.3-7, 3-8 and 3-9).

(II) In xy - plane (quantum well plane), we can modify the Schrödinger equation.

Setting $h(x, y) = e^{(iyk_y)}\varphi(x')$, Eq. 3-12 can be modified into [71]

$$\left[\frac{-\hbar^2}{2m^*} \frac{d^2}{dx'^2} + \frac{e^2 B^2 x'^2}{2m^*} \right] \varphi(x') = E_{xy} \varphi(x'), \quad 3-13$$

where $x' = x + \frac{\hbar k_y}{Be}$. This is a typical Schrödinger equation for harmonic oscillators and the solution is well known. The energy of this xy -plane motion is given by [71]

$$E_{xy} = \left(N + \frac{1}{2} \right) \hbar \omega_c \quad N=0, 1, 2, \dots$$

where $\omega_c = \frac{Be}{m^* c}$ is called cyclotron frequency. The quantum states corresponding to the harmonic oscillator energy states are known as Landau levels.

The total energy including both z - and xy in-plane contributions is

$$E = E_n + \left(N + \frac{1}{2} \right) \hbar \omega_c$$

There are some important lengths and densities that define quantum wells in magnetic fields. The magnetic length l_c is defined as $l_c = \sqrt{\frac{\hbar c}{eB}}$. The degeneracy of a Landau level is $2eB/h$,

where the factor of 2 comes from electron (hole) spin. Typical Landau levels evolve from electronic quantum confinement energy levels in a quantum well are shown in figure 3-5. The crossing or anti-crossing effect between 3rd Landau level evolves from E_1 and the 1st Landau level evolves from E_2 state is shown. The crossing or anti-crossing effect depends on the symmetry properties of wave function of the states and the perturbation at the intersecting point.

For a particular magnetic field, the number of electrons populating a LL is finite. The electron density on a fully filled Landau level at a magnetic field is given by [71]

$$n_e = \frac{eB}{h}.$$

The filling factor ν is defined as

$$\nu = \frac{n}{n_e} = \frac{nh}{eB}.$$

Physically $\nu/2$ at any magnetic field gives the number of fully occupied Landau levels. And again, the factor of $1/2$ comes about because each Landau level has two spin states.

3.7 Excitons and Excitons in Magnetic Field

3.7.1 Excitons

As discussed in Chapter 1, an exciton is a pair of an electron and a hole due to the Coulomb interaction between them, and its energy states are very similar to a hydrogen atom.

Therefore, the exciton energy levels are expressed as

$$E_n^{exciton} = \frac{e^4 m^*}{2\hbar^2 \varepsilon^2 n^2} = \frac{R^*}{n^2}, \quad 3-14$$

where ε is the dielectric constant of semiconductor material, m^* is the reduced effective mass of

an exciton, $n=1, 2, 3, \dots$, and $R^* = \frac{e^4 m^*}{2\hbar^2 \varepsilon^2}$ [41] is called the effective Rydberg energy and

$a_B^* = \frac{\varepsilon \hbar^2}{m^* e^2}$ is an effective exciton Bohr radius. Similar to the hydrogen system, for a given

quantum number n , the degenerate state has fine structures due to angular momentum $l=0, 1, 2,$

$3, \dots$. The fine structure of this exciton is also labeled as $1s, 2s, 2p, \dots$.

In semiconductor quantum wells, the exciton binding energy increases with respect to bulk semiconductors because the electrons and hole at the bottom of conduction band and holes at the top of valence band, which form the excitons, are confined in the same well and their wave function overlap is larger than in the corresponding bulk material. Therefore, the exciton binding energy depends strongly on barrier height and the well width.

Unlike the exciton binding energy for the 3D bulk case given in equation 3-14, in a quantum well with well width less than the exciton diameter $2a_B^*$, the confinement has a significant effect on excitons—one layer of electrons and holes gas are confined in a two dimensional plane. In quantum wells with extremely narrow well widths, the exciton binding energy are given by [41]

$$E_{Exciton}^{2D} = \frac{R^*}{\left(n + \frac{1}{2}\right)^2} . \quad 3-15$$

So, in the 2D case, the ground state binding energy of an exciton is $4R^*$, which is four times that of the 3D bulk semiconductor [73-76].

3.7.2 Magneto –excitons

In the presence of magnetic field, the excitons in semiconductors are called magneto-excitons. Due to the existing magnetic field, the electron and holes start to orbit with respect to each other, and the orbit shrinks if the magnetic field increases. We can expect that the hydrogen-like exciton wave functions diminish in radius with increasing magnetic field.

The Hamiltonian of an exciton in a quantum well in the presence of magnetic field perpendicular to the well layer can be depicted as:

$$H = H_e + H_h - \frac{e^2}{\epsilon \left| \vec{r}_e - \vec{r}_h \right|} . \quad 3-16$$

The first two terms are the Hamiltonian of electron and hole in magnetic field, and the third term is the Coulomb interaction, which depends on the separation between electron and hole in an exciton. The first two terms can be expressed as [71]:

$$H_{e,h} = \frac{1}{2m_{e,h}} (\vec{p}_{e,h} \pm e \vec{A}(\vec{r}))^2 + V_{e,h}(\vec{r}) , \quad 3-17$$

where $\vec{A} = \frac{1}{2}(\vec{r} \times \vec{B})$ is the vector potential from magnetic field.

Due to the presence of the potential $\frac{e^2}{\epsilon \left| \vec{r}_e - \vec{r}_h \right|}$, we cannot separate the Hamiltonian in Eq.3-

16 and the wave function into two parts for z direction and xy -plane to get an analytical solution.

However, if perturbation theory is used to treat the exciton ground state in the presence of an external magnetic field, we can consider the effect of low magnetic field as small perturbation. The perturbation caused by magnetic field can be described as [71]:

$$\Delta E_{ground}(B) \approx \frac{1}{2} DR^* \gamma^2 = \frac{\epsilon^2 \hbar^4}{4c^2 e^2 m^{*3}} B^2, \quad 3-18$$

where γ is a dimensionless effective magnetic field in the form of $\gamma = \frac{\hbar \omega_c}{R^*}$, which is the ratio of cyclotron energy and excitation binding energy, $\omega_c = (\omega_{ce} + \omega_{ch}) = \frac{eB}{m^* c}$ is the combination of electron and hole cyclotron energy and D is the dimensionality parameter for the excitons. Equation 3-18 is often called “diamagnetic shift of exciton” and only valid for $\gamma < 1$ [71].

In the case of high magnetic field limit, where the magnetic field effect is larger than exciton effect and $\gamma \gg 1$, the magneto-exciton is more similar to a free electron hole pair in magnetic field, and the binding energy R_y^* is considered only as small perturbation (See Eq. 3-16). Therefore, in high magnetic fields, the energy shift due to magnetic field is given by:

$$\Delta E_{ground}(B) = \frac{1}{2} \hbar \omega_c.$$

For a GaAs semiconductor quantum well, where R^* is 5.83 meV [77], the value of γ is around 5 T. This is a significant point--if we want to study the optical magneto-excitations in GaAs,

it is necessary to use high magnetic fields in excess of 20 T, since the magnetic field effect is 4 times larger than the Coulomb effect.

Figure3-6 shows the calculation results of free electron hole transition energy and exciton energy of $\text{In}_x\text{GaAs}_{1-x}\text{GaAs}$ (including the band gap E_g) in magnetic field. The solid line are excitonic, which includes the Coulomb interaction between electron and hole pairs that populate at different Landau levels, while the dashed line are Landau energy levels correspondent to free electron and hole populate on different Landau levels.

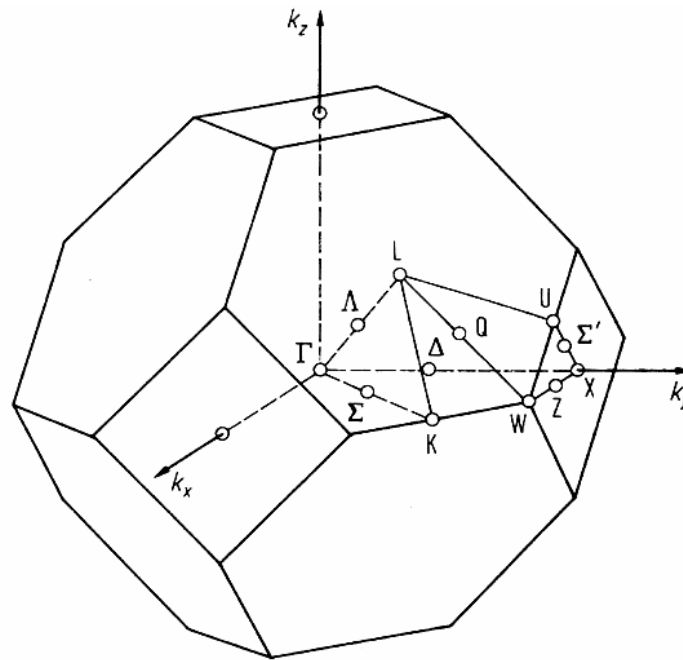
Using this theoretical basis, we turn now to a study of the magneto-optical properties of excitons in $\text{In}_{0.2}\text{Ga}_{0.8}\text{As}/\text{GaAs}$ quantum wells with the goal of understanding emission from highly excited quantum wells in high magnetic fields.

Table 3-1. Periodic parts of Bloch functions in semiconductors

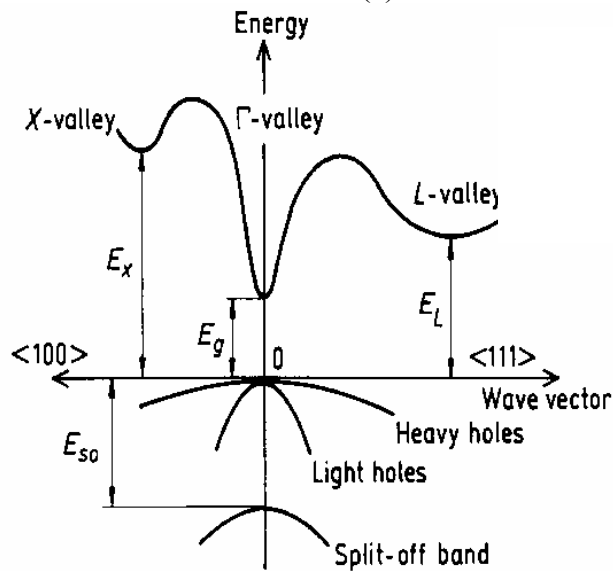
	Quantum number	Wavefunction
u_1	$ s, \frac{1}{2}, \frac{1}{2}\rangle$	$i S\uparrow\rangle$
u_2	$ s, \frac{1}{2}, -\frac{1}{2}\rangle$	$i S\downarrow\rangle$
u_3	$ p, \frac{3}{2}, \frac{3}{2}\rangle$	$\sqrt{\frac{1}{2}} (X+iY)\uparrow\rangle$
u_4	$ p, \frac{3}{2}, -\frac{3}{2}\rangle$	$\sqrt{\frac{1}{2}} (X+iY)\downarrow\rangle$
u_5	$ p, \frac{3}{2}, \frac{1}{2}\rangle$	$\sqrt{\frac{1}{6}} (X+iY)\downarrow\rangle - \sqrt{\frac{2}{3}} Z\uparrow\rangle$
u_6	$ p, \frac{3}{2}, -\frac{1}{2}\rangle$	$-\sqrt{\frac{1}{6}} (X+iY)\uparrow\rangle - \sqrt{\frac{2}{3}} Z\downarrow\rangle$
u_7	$ p, \frac{1}{2}, \frac{1}{2}\rangle$	$\sqrt{\frac{1}{3}} (X+iY)\downarrow\rangle + \sqrt{\frac{1}{3}} Z\uparrow\rangle$
u_8	$ p, \frac{1}{2}, -\frac{1}{2}\rangle$	$-\sqrt{\frac{1}{3}} (X-iY)\uparrow\rangle + \sqrt{\frac{1}{3}} Z\downarrow\rangle$

Table 3-2. Selection rules for interband transitions using the absolute values of the transition matrix elements

Propagation direction	ϵ_x	ϵ_y	ϵ_z	Transition
Z	$\frac{P}{\sqrt{2}}$	$\frac{P}{\sqrt{2}}$	Impossible	hh \rightarrow e
X		$\frac{P}{\sqrt{2}}$	Forbidden	hh \rightarrow e
Y	$\frac{P}{\sqrt{2}}$	$\frac{P}{\sqrt{6}}$	Forbidden	hh \rightarrow e
Z	$\frac{P}{\sqrt{6}}$	$\frac{P}{\sqrt{6}}$		lh \rightarrow e
X		$\frac{P}{\sqrt{6}}$	$\sqrt{\frac{2}{3}}P$	lh \rightarrow e
Y	$\frac{P}{\sqrt{6}}$		$\sqrt{\frac{2}{3}}P$	lh \rightarrow e
Z	$\frac{P}{\sqrt{3}}$	$\frac{P}{\sqrt{3}}$		Split-off \rightarrow e
X		$\frac{P}{\sqrt{3}}$	$\frac{P}{\sqrt{3}}$	Split-off \rightarrow e
Y	$\frac{P}{\sqrt{3}}$		$\frac{P}{\sqrt{3}}$	Split-off \rightarrow e

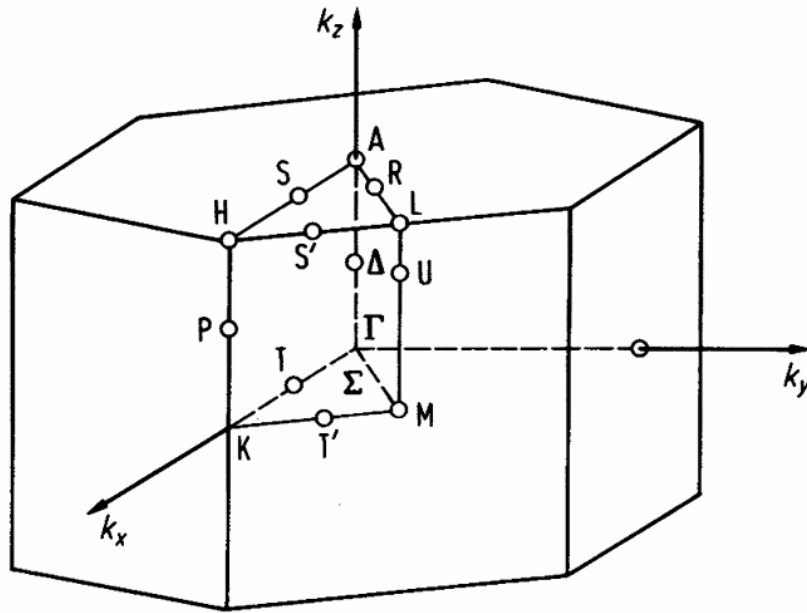


(a)

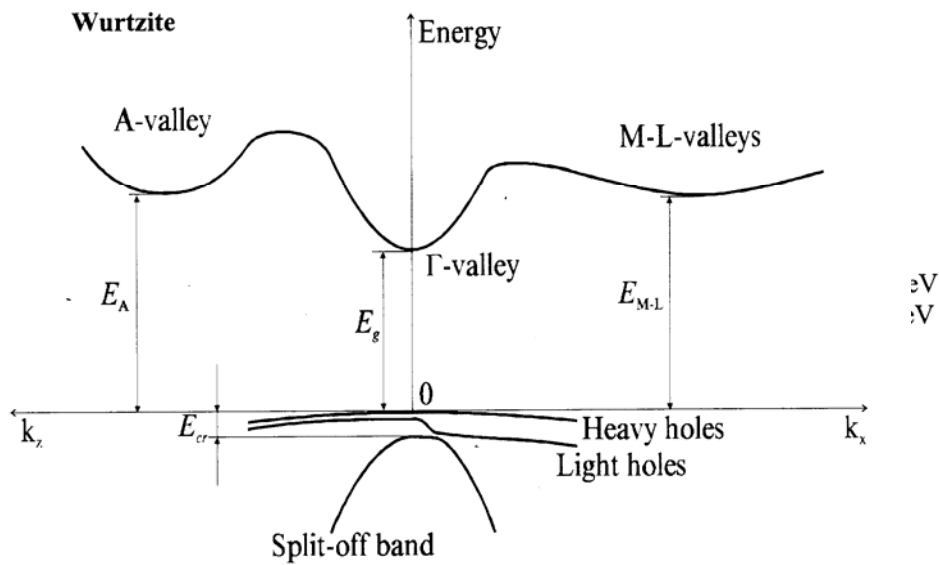


(b)

Figure 3-1. Band structure of Zinc blend semiconductors. (a) Brillouin zone of zinc blend structure. (b) Band structure of Zinc blend structure semiconductor in $\langle 100 \rangle$ and $\langle 111 \rangle$ direction. Γ , X and L valleys of conduction band are shown. Light hole and heavy hole are degenerate at Γ point. From Electronic archive of New Semiconductor Materials, Characteristics and Properties, Ioffe Institute, Russia [78]



(a)



(b)

Figure 3-2. Band structure of wurzite structure semiconductors. Brillouin zone of a wurzite structure. (b) Band structure of a wurzite structure semiconductor in k_x and k_z direction. Γ , A and M-l valleys of conduction band are shown. Degeneracy between heavy hole and light hole at Γ point is lifted. From Electronic archive of New Semiconductor Materials, Characteristics and Properties, Ioffe Institute, Russia [79].

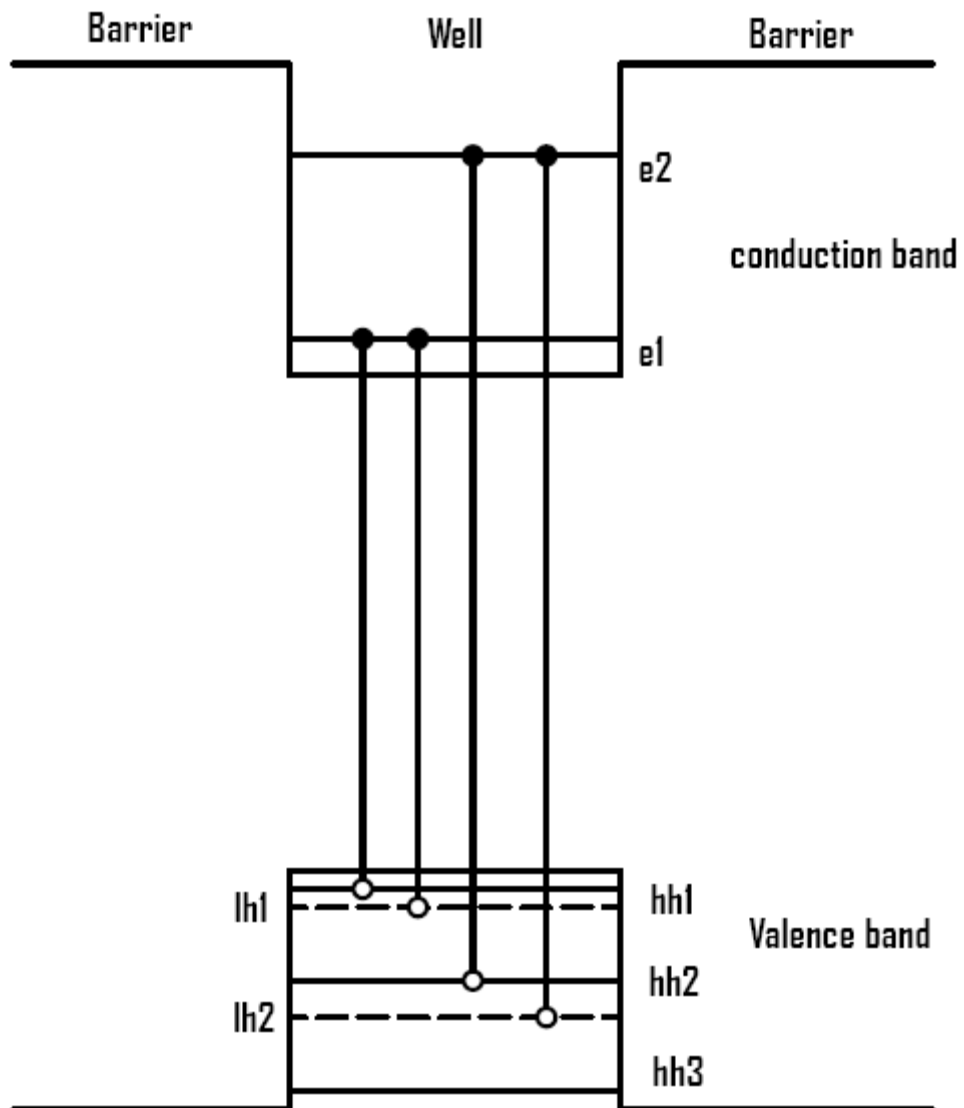
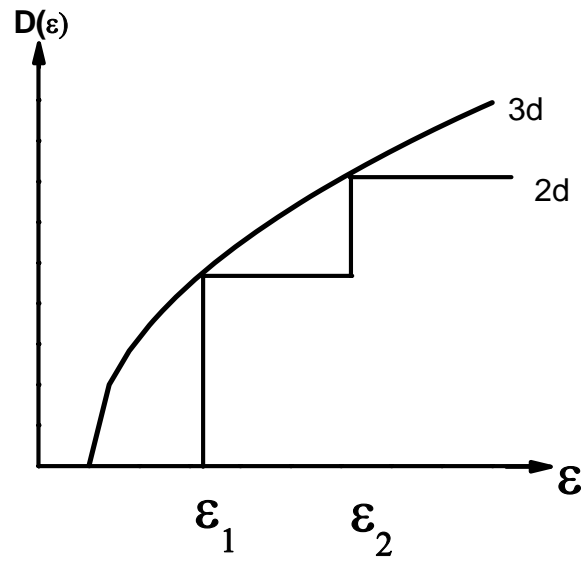
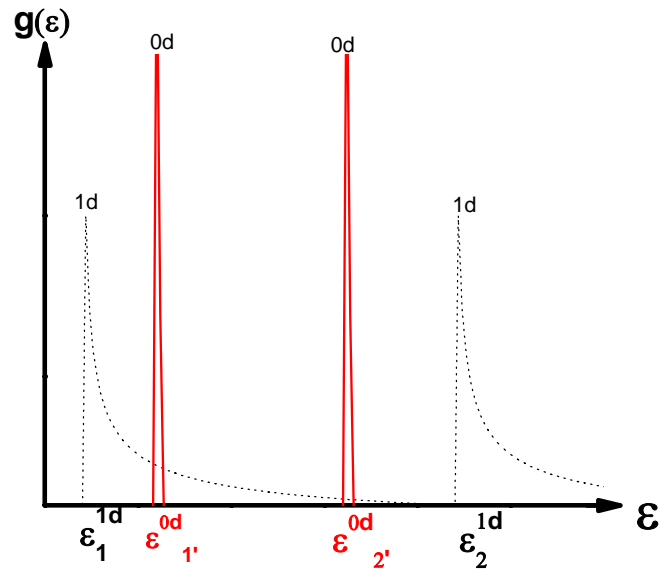


Figure 3-3. Band alignment and confinement subbands in type I semiconductor quantum well. e1 and e2 are subbands in conduction band, hh1, hh2 are the heavy hole subbands in valence band, lh1 and lh2 are light hole subbands in valence band. The solid lines between conduction and valence band are correspondent to the allowed optical transitions.



(a)



(b)

Figure 3-4. Density of states in different dimensions. (a) Density of states in 3D bulk semiconductor and 2D QW; (b) density of states in 1D (dot line) semiconductor quantum wire and 0D (solid line) semiconductor quantum dot (d).

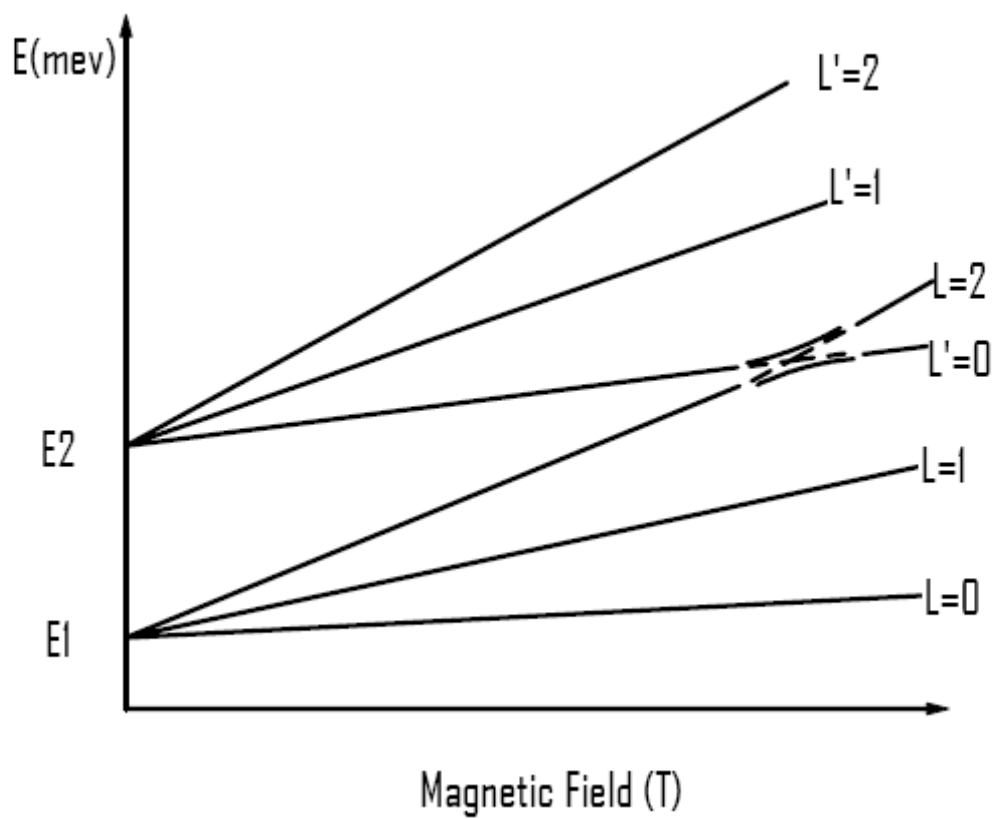


Figure 3-5. Electronic energy states in a semiconductor quantum well in the presence of a magnetic field. The dashed line corresponds to crossing behavior and solid line corresponds to anti-crossing.

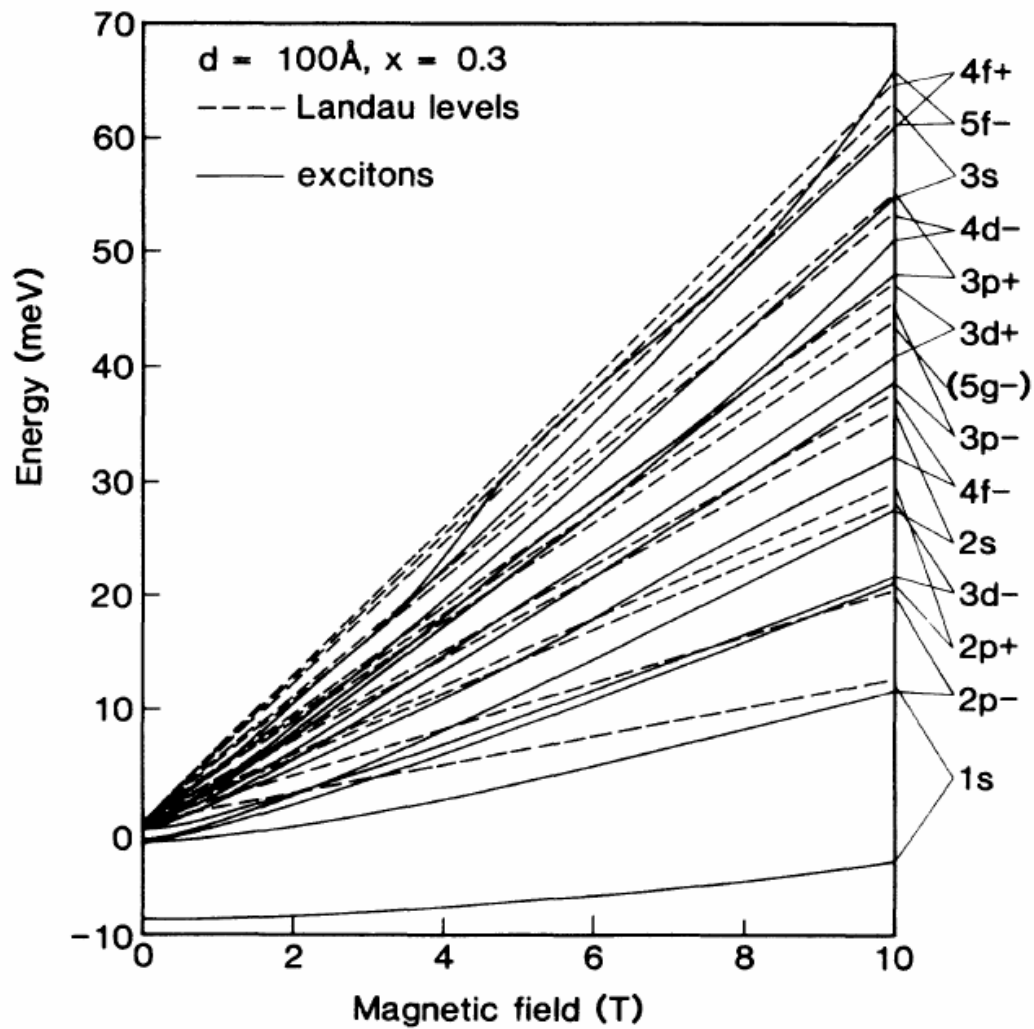


Figure 3-6. Calculation of free electron hole pair energy (dash line) and magneto exciton energy (solid line) of $\text{In}_x\text{Ga}_{1-x}\text{As}/\text{GaAs}$ QW as function of magnetic field. s, p, d, f are different magneto excitonic states. Solid lines are for the e-h pair with consideration of Coulomb effect and dash lines are for the e-h pair without considering Coulomb interaction. Reprint with permission from T. Ando *et al.*, Phys. Rev. B 38, 6015-6030, (1988), figure 7 on page 6022.

CHAPTER 4 MAGNETO-PHOTOLUMINESCENCE IN INGAAS QWS IN HIGH MAGNETIC FIELDS

4.1 Background

Optical phenomena arising from interband and intraband transitions in 2D electron-hole gases in III-V semiconductor quantum well have been studied intensively and extensively in theory and experiments during the past several decades owing to the intense interest in the physics of low dimension system and their potential applications [81].

In a magnetic field, the quantum-confined states in the conduction and valences band split into different Landau levels, resulting in electrons and holes populating different Landau levels, thus, the interband Landau level transitions will dominate optical transitions in magnetic fields. By observing and analyzing inter-*LL* optical transitions, we can study the optical transitions of 2D electron hole gas such that detailed information about the conduction and valence band structures, carrier effective mass and carrier interactions between different Landau levels (such as crossing and anti-crossing) can be acquired [82-84]. This work will serve as a background to the next chapter on the nature of light emission from dense magneto-plasmas in quantum wells.

Using relatively weak light sources such as tungsten and xenon lamps, we can measure the absorption spectrum of optical transitions from valence band Landau levels to conduction band Landau levels in semiconductor QWs in magnetic fields and determine the energy peaks of each inter-Landau level transition. In the absorption spectrum, these optical transitions are still predominantly excitonic, since the separation between two electron hole pairs is relatively larger than the exciton Bohr radius ($d \gg a_{exciton}$), so that the Coulomb interaction between electron and hole in a exciton system are not screened.

PL due to recombination of electrons on a conduction Landau level with holes on a valence band Landau level is necessary to study the Landau level physics of magneto-excitons (at low

densities) or magneto-plasmas (at high densities). In this case, CW excitation (for example, with a He-Ne laser) is not sufficient since it cannot create a large number of carriers to populate in higher Landau levels; the only photon emission channel is due to the transition lowest electron Landau level to highest hole Landau level. Therefore, pulsed lasers such as Q-switched or mode locked lasers are needed to generate a sufficiently high carrier density so that interband transitions due to higher Landau levels are observed. During the excitation, the laser pulse transfers large amount of energy to the semiconductor in a very short time (\sim ps), and carriers can reach high densities before their recombination, which deplete the higher *LLs*.

III-V group semiconductor quantum wells, especially composed of GaAs or $\text{In}_x\text{Ga}_{1-x}\text{As}$, are widely used to study the physics of magneto-excitons [85]. This group of materials has a relatively small effective mass $m^* \sim 0.067m_0$ (m_0 is the free electron mass), which makes it easy to observe transitions between higher Landau levels, since the Landau level splitting between two consecutive levels is given by

$$\Delta E = \hbar\omega_c = \hbar \frac{eB}{m^*c} . \quad 4-1$$

In addition, for $\text{In}_x\text{GaAs}_{1-x}/\text{GaAs}$ quantum wells, the degeneracy of heavy hole and light hole is lifted at Γ point due to the existence of strain in the well. This is an effect of degenerate perturbation in quantum mechanics. The lattice mismatch between well and barrier material cause a crystal lattice distortion and induce a new static electric field in the Hamiltonian of electrons on valence bands. This perturbation lifts the degeneracy between heavy hole and light hole subband.

Since the heavy hole and light hole are separated by ~ 100 meV, we can observe transitions between electron *LLs* and *LLs* originating from heavy hole and light hole subbands respectively.

Before we start to investigate the inter-*LL* transitions, the labeling of the inter-Landau level transitions needs to be defined. A diagram of interband *LL* transitions is plotted in Fig.4-1(b), which describes the optical processes of each peak in absorption spectrum. We use the hydrogen-like excitonic notation to represent the transitions, and the meaning of each term is given as following.

en is an electron on the n th subband, hn is a hole on the n th subband, l or h means heavy hole or light hole subband and ns means that both electron and hole are on the n th *LLs* originate from a subband. This notion well represents the hydrogen like $e-h$ pair bond with Coulomb interaction. However, under high excitation density, we use 0-0, 1-1 and 2-2 to represent the $e-h$ inter *LL* transitions (see Fig. 4-2(a)), since the electron and holes density is high and Coulomb interaction between electron and hole in an $e-h$ pair is screened so that the electron hole pair is plasmonic instead of excitonic [89, 86-88].

Ando and Bauer [90], and Yang and Sham [91-92] have theoretically studied magneto-excitons in 2D electron hole gas in GaAs quantum wells from low to high magnetic field. Valence band complexity, which due to the mixing between different subbands in valence band (shown in Fig.4-2(a)) is considered in their calculation of inter-*LL* transitions to account for diamagnetic shift at low field, linear dependence of magnetic field at high field and other experimental results.

Using nanosecond pulsed laser excitation at high powers, Butov, *et al.* have studied the photoluminescence of interband -*LL* transitions in $\text{In}_x\text{Ga}_{1-x}\text{As}$ quantum well up to 12 T in details [93]. In his experiments, the photoexcited electron-hole gas is considered as a magnetoplasma instead of magneto-excitonic at high laser excitation powers (carrier density up to 10^{13}cm^{-2} in the quantum well). In addition to 0-0 transitions, transitions between higher *LLs* are also observed in

the PL spectrum, as shown in Fig. 4-2(a). In Fig. 4-2(a), the peaks of the *LL* transitions (*n-n*) shift to the low energy side with the increasing of carrier density. This is caused by carrier-induced bandgap renormalization (BGR), which is considered to be many body effects and can be interpreted using many body theory instead of single particle theory [93].

4.2 Motivation for Investigating PL from InGaAs MQW in High Magnetic Fields Using High Power Laser Excitation

While these prior magneto-photoluminescence experiments have revealed several insights about the physics of high densities of carriers in Landau levels, they were performed in relatively low fields (less than 12 T) using either CW optical measurements or nanosecond pulsed laser excitation, with excitation densities of few GW/cm². A drawback of using nanosecond excitation for these experiments is inter-LL carrier relaxation can occur during the excitation pulse, resulting in an equilibrium distribution of filled *LLs*. In addition, inter-*LL* recombination can actually occur during pumping, reducing the carrier density.

In order to investigate these PL effects in QW in new regimes with higher densities and larger *LL* separation (i.e. higher magnetic fields and high pump power excitation), new facilities are required. As discussed previously in Chapter 2, we have developed an ultrafast spectroscopy laboratory at the DC High Field Facility of the National High Magnetic Field Laboratory, with the capability of probing over the 200 nm–20 μ m wavelength range with 150 fs temporal resolution in fields up to 31T.

In high magnetic fields, the density of states of 2D electron hole gas will evolve into a 0D hydrogen like system owing to magnetic field confinement (See Chapter 3). We can expect that all the electron and hole states will populate a very small energy range in a width ΔE about the energy E of the *LLs*, resulting in each energy level of this 0D system having a very high density

of state (see Fig.3-4). New optical phenomena are expected in this high-density electron hole gas system at high magnetic field since the Coulomb interaction between e-h is screened.

4.3 Sample Structure and Experimental Setup

$\text{In}_x\text{GaAs}_{1-x}/\text{GaAs}$ with $x=0.20$ semiconductor QW samples were grown via molecular beam epitaxy (MBE) method on GaAs substrates. The samples consist of a GaAs buffer layer grown at 570°C followed by 15 layers of 8 nm $\text{In}_{0.2}\text{Ga}_{0.8}\text{As}$ quantum well separated by 15 nm thickness GaAs barriers, all were grown at substrate temperature between 390 to 435° . Samples were provided by Glenn Solomon from Stanford University. The sample structure is shown in figure 4-4.

Using the CW optics setup and resistive magnet described in Chapter 2 at the NHMFL, the absorption spectra were measured at 4.2K up to 30 Tesla. The white light source used for absorption spectrum is tungsten lamp and excitation light source for the CW PL spectroscopy is a He-Ne laser at 632nm wavelength. Using the ultrafast optics facility and a 31T resistive magnet, the photoluminescence spectrum was measured for the same sample at $T=10$ K. The excitation light sources are the CPA and a tunable OPA as described in Chapter 2. The CPA laser operates at 775 nm and the OPA was tuned to 1100 nm and 1300 nm respectively. We excite the sample with different power up to $25 \text{ GW}/\text{cm}^2$. In both absorption and PL experiments, we chose the Faraday geometry shown in Fig. 4-5, in which the magnetic field is perpendicular to the quantum well plane and the propagation of light is parallel to the magnetic field.

4.4 Experimental Results and Discussion

4.4.1 Prior Study of $\text{In}_x\text{Ga}_{1-x}\text{As}/\text{GaAs}$ QW Absorption Spectrum

As a prelude to our investigations, Jho and Kyrychenko [82] have previously studied $\text{In}_x\text{Ga}_{1-x}\text{As}$ QW samples used in our high field experiments in high magnetic fields to understand the complex mixing behavior. For reference, the energy levels of this InGaAs quantum well are

shown in Fig.4-6. The magnetic field-dependent absorption spectrum of InGaAs quantum is shown in Fig 4-1(a). At zero fields, three exciton levels, e1hh1, e1lh1 and e2hh2, are clearly resolved, and the shape of absorption curve is a step function, corresponding to a 2D e-h gas density of state. Between the exciton levels, continuum absorption is also observed. We can see that the splitting between h1 and l1 hole state is relatively large (~100 meV), induced by the strain on $\text{In}_x\text{Ga}_{1-x}\text{As}$ QW, which is caused by the mismatch of crystal lattice between InAs and GaAs semiconductor. This energy separation reduces the wavefunction mixing between h1 and l1 hole states and permits unambiguous study of the e1lh1 exciton, since e1hh1 and e1lh1 exciton states can be considered separately.

With increasing magnetic field strength, the e1hh1 and e1lh1 exciton states split into magneto-exciton states e1hh11s, e1hh12s, e1hh13s and e1lh11s..., using the description of the magneto-exciton states given above. The corresponding inter-Landau level transitions are given in Fig.4-1(b). At higher magnetic fields, we can see from spectrum that the continuum states between exciton steps collapse and the absorption spectrum curve evolves into 0D-like density of states, indicating that e-h gas system has evolved into a quasi 0D system (see Fig. 4-1).

In the absorption spectrum, each excited magneto-exciton state (2s,3s,4s) originating from the e1lh1 state shows anti-crossing –like splitting when it intersects with e1lh11s state, indicated with arrows. Jho and Kyrychenko have previously modeled this anti-crossing effect [83]. They found that each excited state shows anti-crossing like splitting when it meets a dark state. This splitting behavior is independent of polarization, and sensitive only to the parity of the quantum confined states. They also attribute the origin of this effect (~9meV) to Coulomb interaction between e-h pair instead of hole valence band complexity. In Fig. 4-4, an example of valence band mixing is shown. In this figure, the dispersion curve of heavy hole subband crosses the light

hole subband at certain k value, which causes the wavefunctions of heavy hole and light hole get mixed also.

4.4.2 PL Spectrum Excited with High Peak Power Ultrafast Laser in High Magnetic Field

We now contrast the above spectrum with PL observed using ultrafast laser pulses. Fig. 4-7 shows magnetic field dependent PL spectrum from $\text{In}_x\text{Ga}_{1-x}\text{As}$ QW excited with 775 nm, 150 fs laser pulses of 10 GW/cm^2 , which generates carrier density $\sim 10^{12} \text{ cm}^{-2}$. At zero field, we observe e1h1 and e2h2 interband transitions, and with the increasing of magnetic field these two PL peaks split into inter-LL transitions ('Landau fan'). We observed PL from well defined inter-LL transitions up to e1h15s, but the anti-crossing-like splitting between e^1h^1 ns and e^1l^1 ns in the absorption spectrum are not observed in this PL spectrum. As mentioned above, the anti-crossing effect is due to the Coulomb interaction between electrons and holes, therefore, the absent of mixing of LL states indicated that the Coulomb interaction is screened at high e-h density so that the corresponding transitions between LL states in Fig.4-7 are not purely excitonic.

For comparison, we plot the Landau fan diagram comparing the absorption spectrum and PL spectrum under high power excitation in Fig. 4-8. The Landau fan diagram of PL is very different from the Landau fan diagram of absorption even at high magnetic field. First, for the same inter-LL transition, the energy position of each PL peak has red shift with that of the CW absorption peak, which we attribute to carrier density-induced bandgap renormalization [93]. This band gap renormalization is caused by the many body effect of carriers and this many-body effect gets stronger at high carrier density. Second, at high magnetic field, since the excitonic effect can be neglected, we have the following form for the energies:

$$E = E_g + \frac{\hbar e B}{m^* c} (n+1), \quad 4-2$$

where E is the energy position of peak of a LL at given magnetic field B , E_g is the band gap, m^* is e - h pair effective mass and n indicates the n th LL . We can see that in equation 4-2, E is linearly proportional to B and $1/m^*$ is the slope, fitting result shows $m^*=0.0672m_0$, m_0 is the electron effective mass. From Fig.4-8, we can see that for a trace of given LL , the effective mass in the absorption spectrum should be higher than that in the PL line, which indicates that the m^* is higher at low carrier density. Third, in the case of free e - h pairs with no excitonic coupling, such as in e - h plasma, the traces of all the LL s originate from same subband should converge at zero field since the Coulomb interaction bind e and h is screened. This effect is consistent with the traces of LL s in PL spectrum. However, in absorption spectrum, the line of LL s peak positions do not converge at zero field because of the existing of e - h binding energy. Thus, the magneto-PL of $\text{In}_x\text{Ga}_{1-x}\text{As}/\text{GaAs}$ QWs excited with high power ultrafast laser pulses is most likely plasmonic instead of excitonic.

In Fig.4-9, we plot the magneto-PL excited with different excitation intensity for three wavelengths (a) 1300 nm, (b) 1100 nm and (c) 775 nm at 25 T. For each wavelength, we denote the lowest and highest excitation intensity in GW/cm^2 . The peak position are assigned from lower energy side 0-0 to higher energy side 1-1, 2-2 and respectively. From the Fig.4-9, we can see that the excitation with 1.1 μm and 1.3 μm are below InGaAs QW bandgap so that the PL originates from carriers excited via two-photon absorption into the GaAs barrier and capping layer as well as the continuum states of $\text{In}_x\text{Ga}_{1-x}\text{As}$ QW. For 775 nm as well as 1.1 and 1.3 μm excitation, PL emission occurs after excited carriers relax down to the QW subbands. In Fig. 4-9, the peak energies of each LL remain at fixed positions and do not show any red shift at high pumping intensity. This indicates that the many particle interaction effect is not resolved and the bandgap renormalization effect is suppressed at low excitation power.

In Fig4-9 (a), (b) and (c), we can see that the character of energy peaks 1-1 and 2-2 are very different from 0-0 peak. At low excitation powers, broad and weak peaks from 1-1 and 2-2 are seen in (b) and (c). With increasing the excitation laser intensity, a narrow peak starts to appear on the high-energy side of 1-1 and 2-2 peaks and become dominant at high excitation power. The linewidth of narrow peak of 1-1 is 2.3 meV, smaller than that of 0-0 peak (9 meV), implying a different emission origin for these two peaks. In addition, we do not observe these narrow peaks in the magneto-exciton absorption spectrum shown in Fig.4-1.

We plot the 775 nm, 1.1 μm and 1.3 μm laser excitation power dependence of PL intensity for 0-0 transitions, 1-1 transition, including broad and narrow peaks, in Fig4-9 (d) to (f). For 775nm excitation, the PL intensity from all the three states rise up rapidly at low power ($<2\text{GW}/\text{cm}^2$) and then saturates. At 1.1 μm and 1.3 μm excitations, the PL intensity from 0-0 transition and tail of 1-1 transition increases proportionally to I_{pump}^2 , since the excitation requires a two photon absorption which scales as the square of laser intensity. However, the narrow peak of 1-1 transition shows very different scaling. In Fig.4-9 (d), the narrow peak of 1-1 LL transition shows no emission until threshold pump intensity ($\sim 13 \text{ GW}/\text{cm}^2$), which might be an evidence of stimulated emission processes.

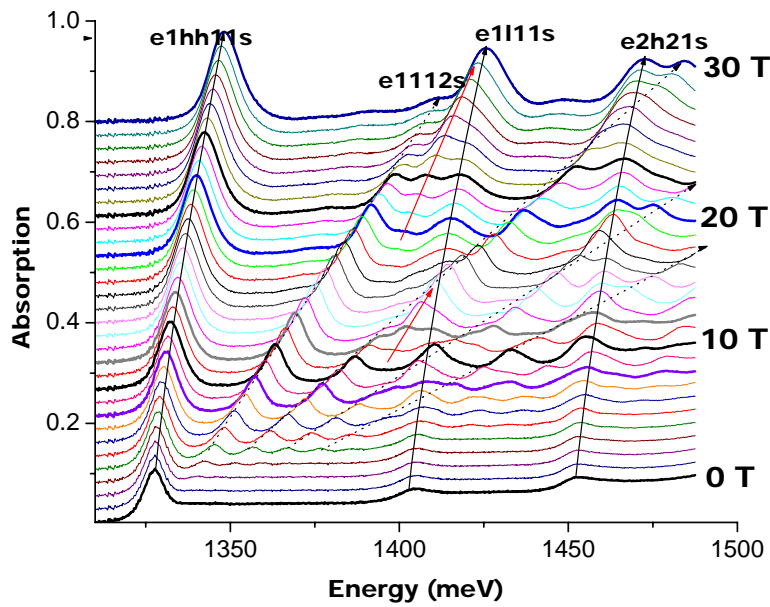
To understand the many particle effect in the high density of electron hole gas generated with femtosecond lasers, we plot the magnetic field dependent spontaneous emission calculated with an 8 band in Pidgeon-Brown effective mass model [94](for details, see appendix B) in Fig.4-10 (a). Fig. 4-10(b) is the correspondent experimental results. By comparing the two curves, we estimate that the actual carrier density is between $10^{12}/\text{cm}^2$ and $10^{13}/\text{cm}^2$ in our experiments. However, there are several discrepancies between theoretical calculation and our experimental results.

- (I) The energy peaks of higher LL levels are shifted due to the single particle theory, in which the Coulomb interactions between electron hole and renormalization effects are neglected.
- (II). Spin induced splitting in magnetic field is not observed experimentally due to the large inhomogeneous broadening of the PL peaks.
- (III) The theory does not predict the emergence and power scaling of the narrow emission peaks at 1-1 LL transition,

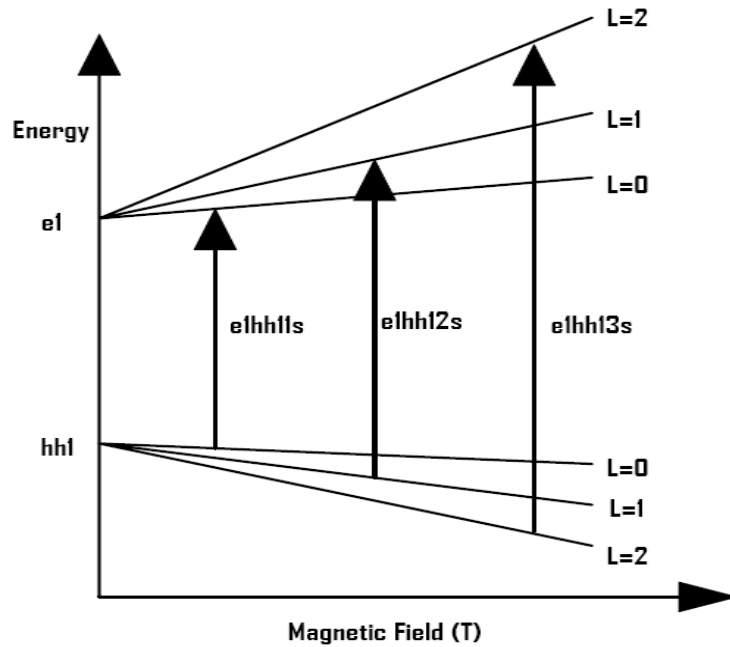
We suggest that the experimental curves are induced by new emission processes at higher lying LL s. More systematic studies are presented in the next chapter to elucidate the origin of these phenomena.

4.5 Summary

With the underlying theory of LL physics, we have elucidated the conduction and valence band structure of $\text{In}_x\text{Ga}_{1-x}\text{As}/\text{GaAs}$ QW. The anticrossing behavior between LL s originate from different subbands has been discussed. Previous investigation shows that the anticrossing is due to Coulomb interaction between $e-h$ excitonic pair. Furthermore, by comparing the CW experimental magneto-absorption spectrum and magneto-PL spectrum with ultrafast high power laser excitation, it is found that the interaction between $e-h$ is plasmonic rather than excitonic. Also new sharp features emerge in the PL spectrum of interband LL transitions, which implies new optical process in the PL emission. That is the subject of Chapter 5.



(a)



(b)

Figure 4-1. Magneto absorption spectrum and schematic diagram of interband Landau level transitions. (a) Magneto absorption spectrum of $\text{In}_x\text{Ga}_{1-x}\text{As}/\text{GaAs}$ quantum well in Faraday geometry at 4.2 K up to 30 T, magneto excitonic states are labeled; (b) Energy diagram of the optical transition in the magneto absorption spectrum of $\text{In}_x\text{Ga}_{1-x}\text{As}/\text{GaAs}$ quantum well. Each transition corresponds to a peak in the absorption spectrum.

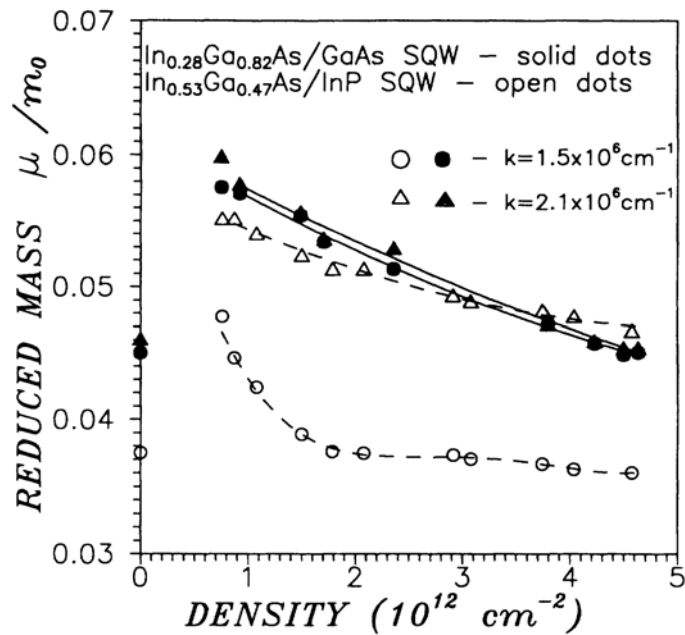
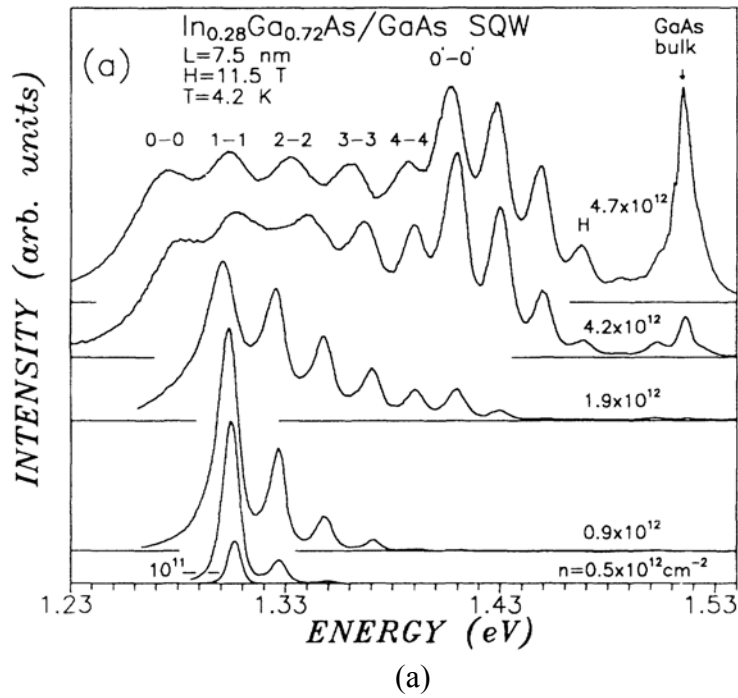


Figure 4-2. Magnetophotoluminescence experimental results of band gap change and effective mass change. (a) Band gap renormalized at high carrier density, (b) Reduced effective mass renormalized at high carrier density in $\text{In}_x\text{Ga}_{1-x}\text{As}$ semiconductor QW. Reprint with permission from L. Butov *et al.*, Phys. Rev. B 46, 15156 - 15162 (1992), Figure 2 on page 15158 and Figure 8 on page 15161

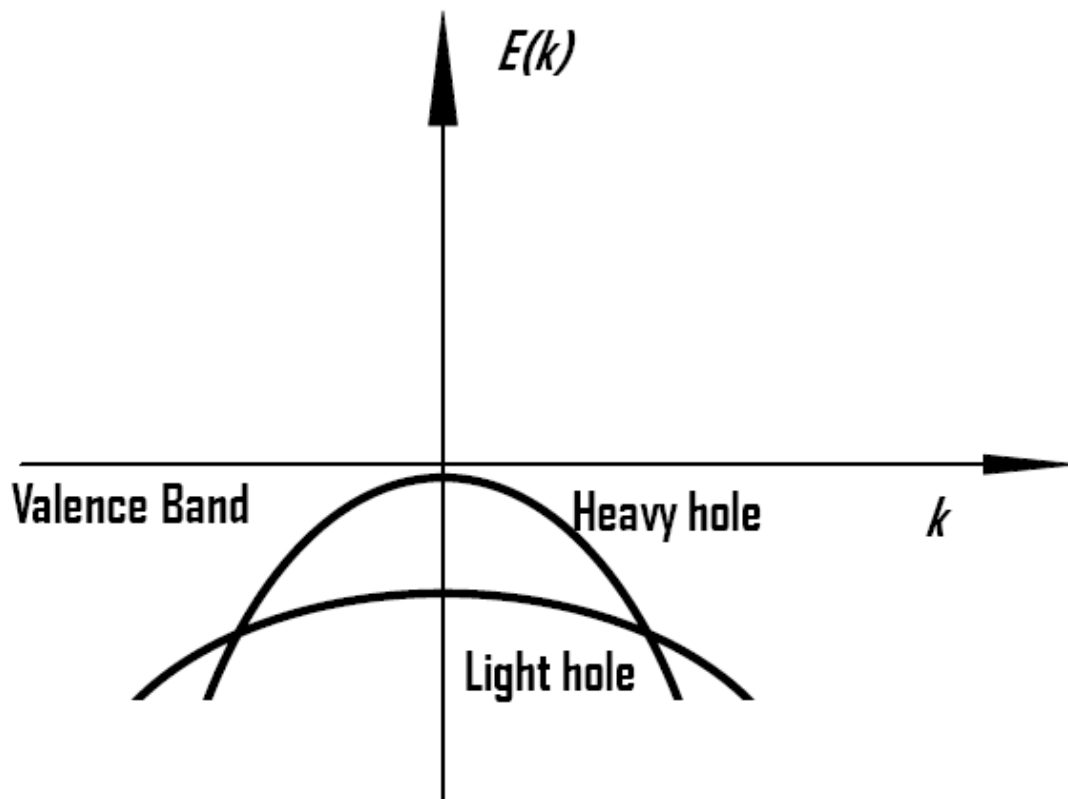


Figure 4-3. Valence band mixing of heavy hole and light hole subbands in semiconductor quantum well. Light hole subband crosses with heavy hole subbands.

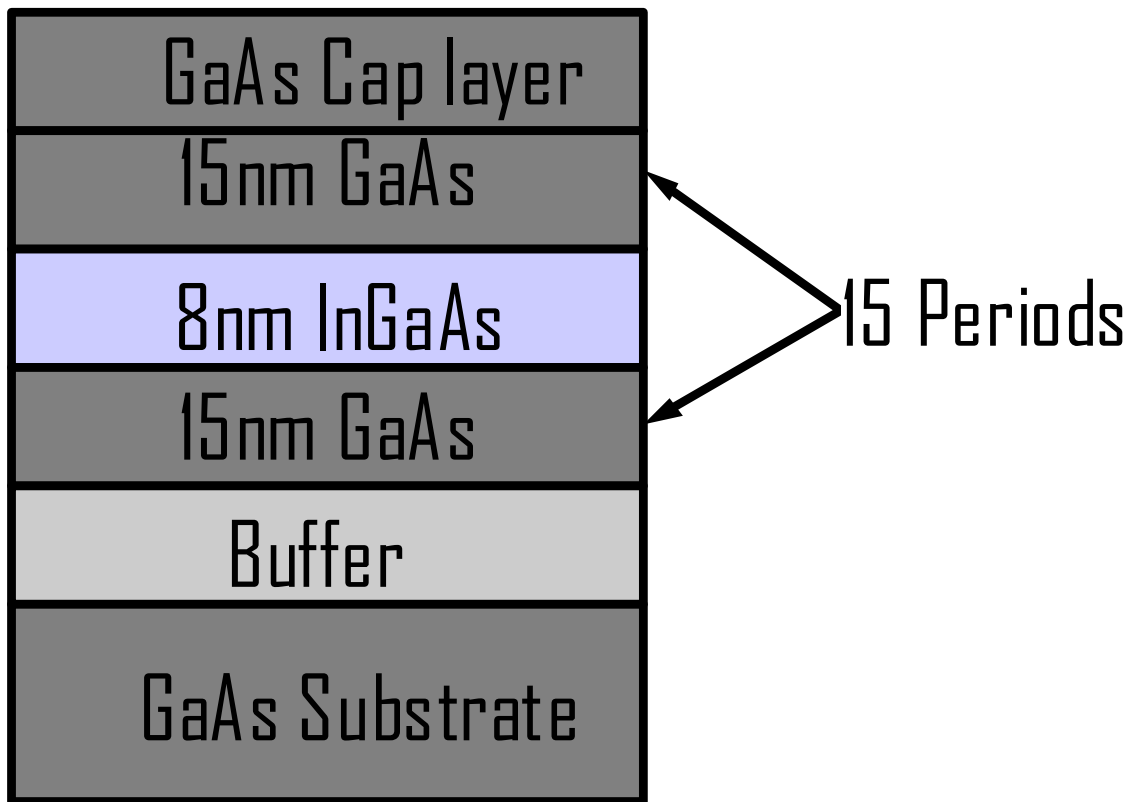


Figure 4-4. Structure of In_{0.2}Ga_{0.8}As/GaAs multiple quantum well used in our experiments.

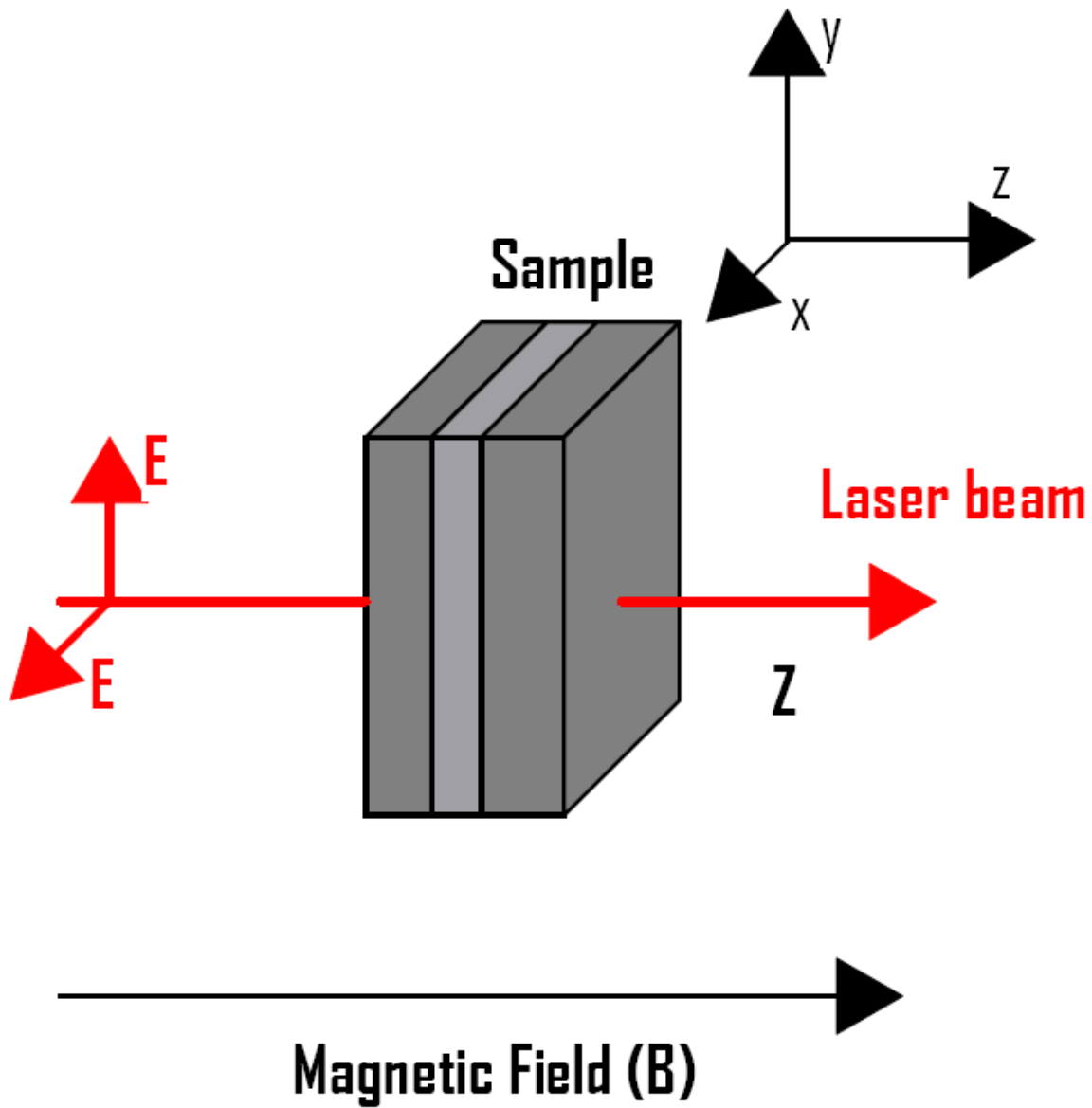


Figure 4-5. Faraday configuration in magnetic field. The light propagates in the direction of the magnetic field B and the electric field polarization E is perpendicular to the magnetic field.

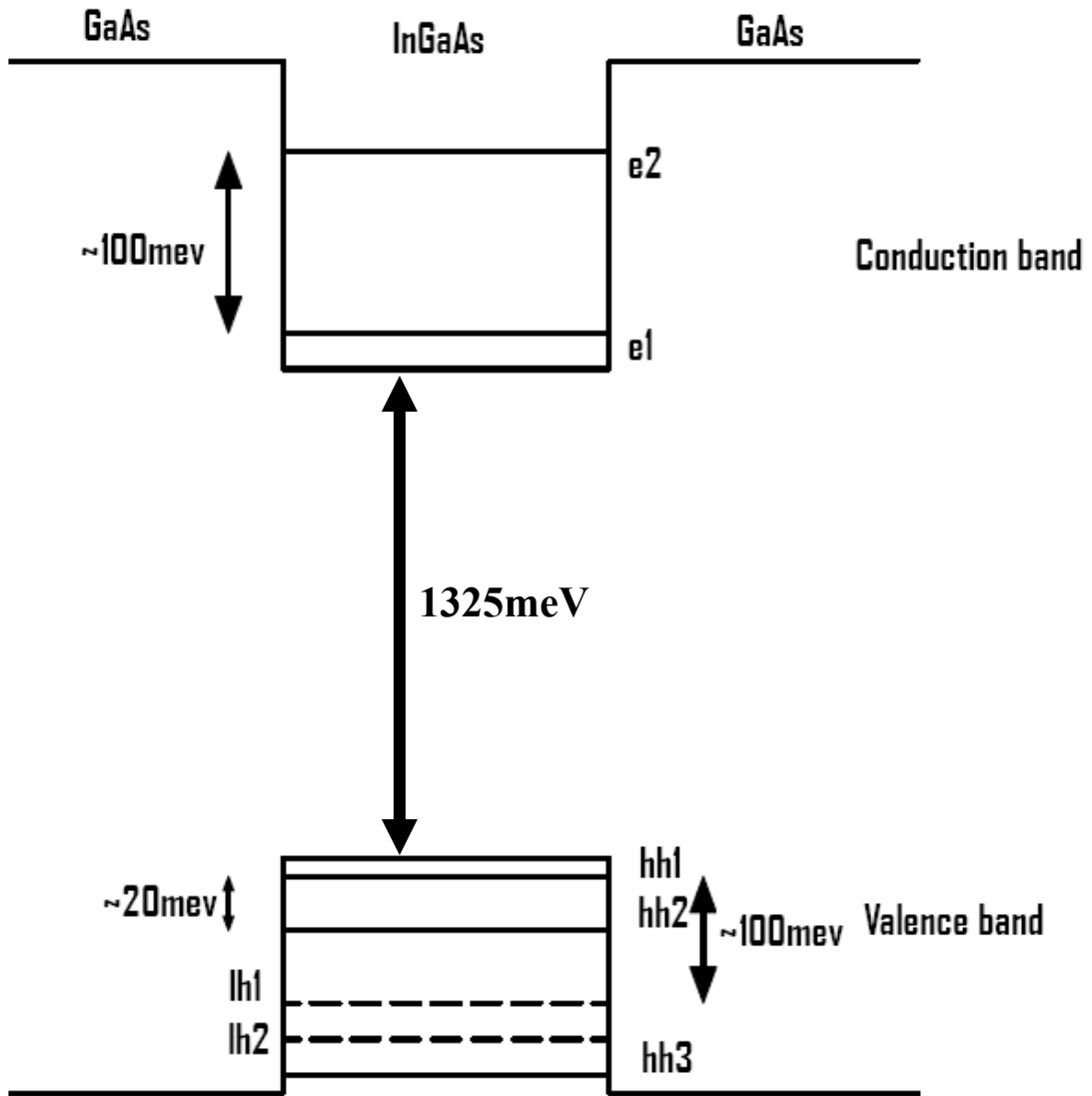


Figure 4-6. Energy levels of electron and hole quantum confinement states in $\text{In}_x\text{Ga}_{1-x}\text{As}$ quantum wells. e1,e2, hh1, hh2 denote the electron and hole states due to quantum confinement.

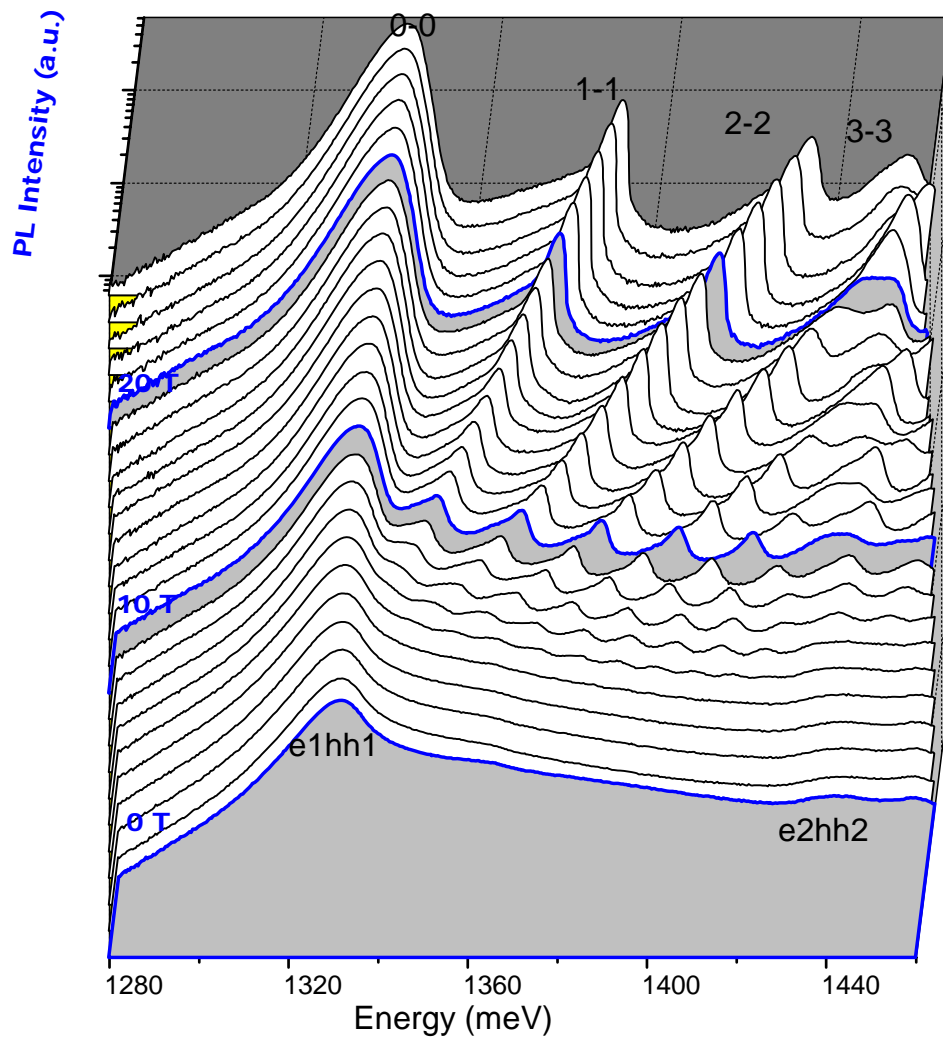


Figure 4-7. Magneto-photoluminescence spectrum of $\text{In}_x\text{Ga}_{1-x}\text{As}$ quantum well at 10K. The excitation laser source is a 775 nm CPA laser with 150 fs duration and excitation power of 10 GW/cm^2 .

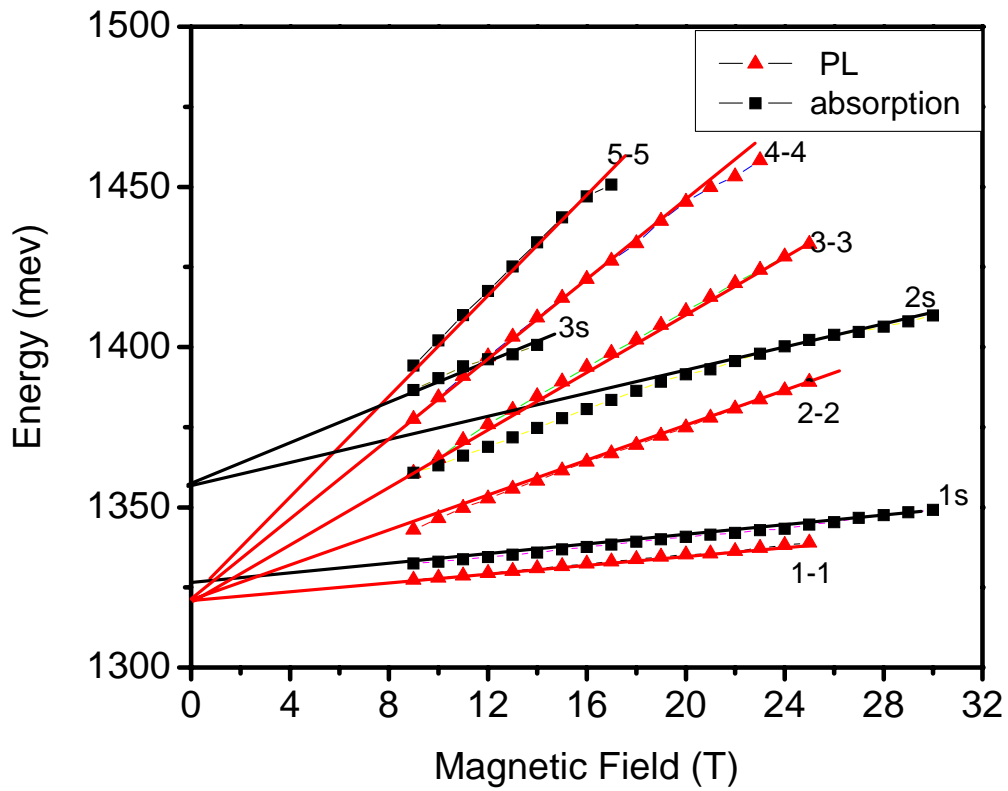


Figure 4-8. Landau fan diagram of absorption and PL spectrum of $\text{In}_x\text{Ga}_{1-x}\text{As}$ quantum well in magnetic field up to 30 T. The solid squares are the energy positions of interband LL transitions from absorption and the solid triangles are energy positions of interband- LL transitions from PL spectrum.

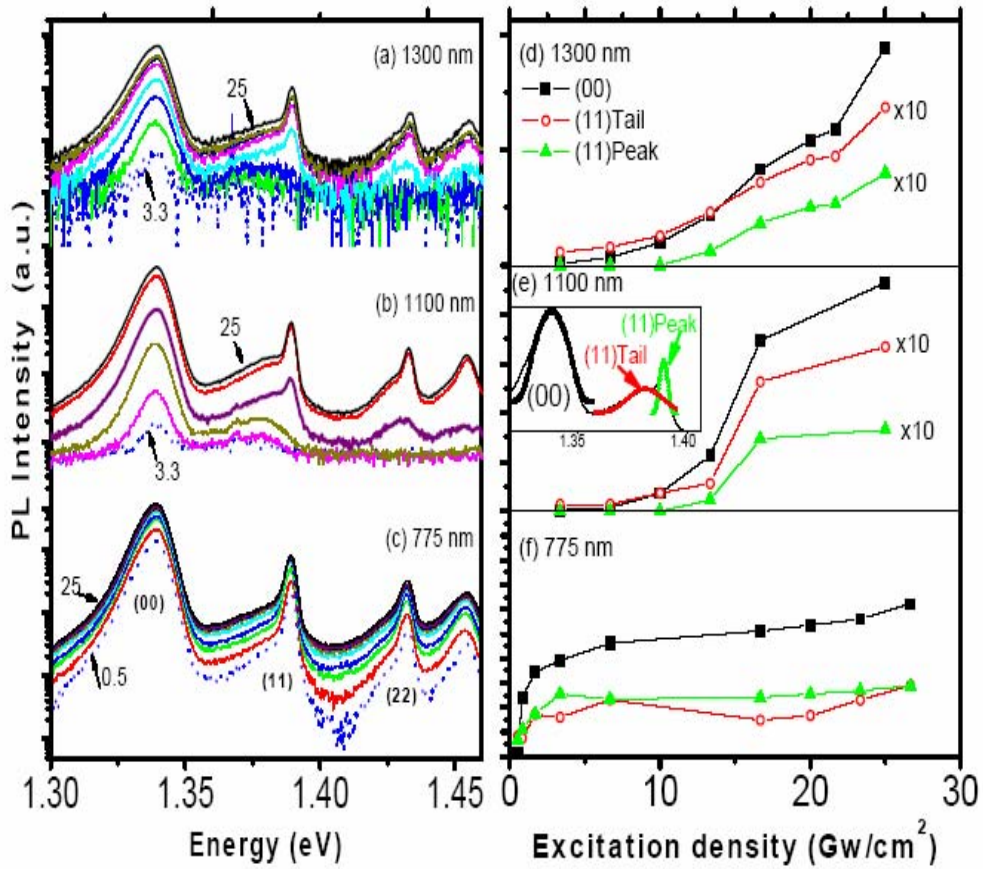


Figure 4-9. Magneto-PL (a-c) and excitation density dependence (e-f) of the integrated PL signal in $\text{In}_x\text{Ga}_{1-x}\text{As}$ quantum wells at 20 T and 10 K. The left side plots the PL spectra on a semilog scale excited at (a) 1300 nm, (b) 1100 nm, (c) 775 nm, the excitation density is marked with arrows. The right side displays the excitation density dependence at (d) 1300 nm, (e) 1100 nm and (f) 775 nm.

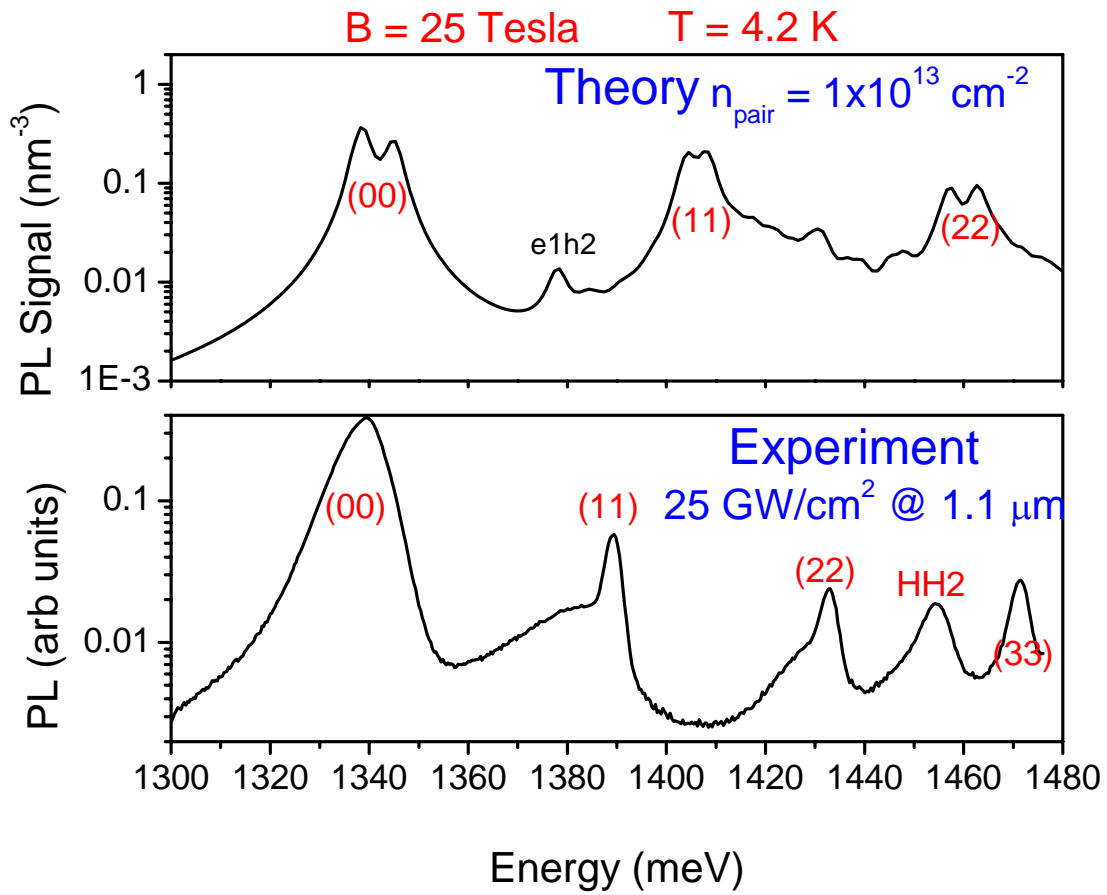


Figure 4-10. Theoretical calculation and experimental results of PL in high magnetic field. Theoretical calculation of the PL spectrum based on an 8 band Pigeon Brown model (top panel, from Gary Sanders) and experimental results (lower panel) of magneto-PL emitted from $\text{In}_x\text{Ga}_{1-x}\text{As}$ with high excitation density at 25 Tesla and 4.2 K.

CHAPTER 5
INVESTIGATIONS OF COOPERATIVE EMISSION FROM HIGH-DENSITY ELECTRON-
HOLE PLASMA IN HIGH MAGNETIC FIELDS

5.1 Introduction to Superfluorescence (SF)

In this chapter, we consider the unique nature of cooperative electro-magnetic emission made possible using ultrafast laser excitation of quantum wells placed in high magnetic fields. This combination allows us to create atomic-like behavior between electrons and holes at carrier densities well above those which support excitons. As such, these ‘simulated atoms’ can emit light cooperatively via superfluorescence.

The nature of the emission of light from atoms and atom-like systems depends sensitively on the physical environment surrounding them, and can be tailored by controlling that environment [96-98]. At the most fundamental level, atom-photon interactions can be modified by manipulation the number density, phase, and energies of atoms and photons involved in the interaction. A very common example is the laser, in which mirrors are used to provide coherent optical feedback to a population inverted atomic system, resulting in the emission of photons with well-defined spatial and spectral coherence properties. Less common but equally fundamental examples are the “superemission” processes, superradiance (SR) and superfluorescence (SF), cooperative spontaneous emission from a system of N inverted two-level dipoles in a coherent superposition state.

Experiments probing these phenomena in atomic systems have provided significant insight into the fundamental physics of light-matter interactions [99]. In our experiments, by manipulating the coherent interactions of electrons and holes in a semiconductor quantum well using intense ultrashort laser pulses and strong magnetic fields, we generate superfluorescence in a completely new and unexplored regime. Our experiments begin to approach the question of whether atom-photon interactions in semiconductors are truly “quantum” as they are in atoms.

5.1.2 Spontaneous Emission and Amplified Spontaneous Emission

The simple illustration of spontaneous emission process is shown in Fig.5-1 (a). For a two level atom system with a high energy excited state E_2 and a low energy ground state E_1 , the atoms populating the E_2 state might spontaneously transit to E_1 state without any external electromagnetic field perturbation. A photon is emitted with energy $\hbar\omega = E_2 - E_1$, where ω is the angular frequency of an emitted photon. We can describe this spontaneous emission as [120]

$$\frac{dN}{dt} = -A_{21}N, \quad 5-1$$

in which N is the number of atom on excite states E_2 and A_{21} is called spontaneous emission probability or Einstein A coefficient. The solution of this equation is an exponential decay function given by

$$N = N_0 e^{-\frac{t}{\tau_{21}}}, \quad 5-2$$

where N_0 is the initial number of atom on E_2 state and τ_{21} is the life time of this transition.

Comparing Eq. 5-1 with 5-2, we have $\tau_{21} = A_{21}^{-1}$.

As we know, if atoms are far enough from each other and the interactions between atoms are neglected, the spontaneous emission that occurs in one atom on excited state is also isolated from the spontaneous emission from another atom on excited state. Therefore, spontaneous emission has random directionality. Also as we see from equation 5-1, the intensity of spontaneous emission is proportional to N , the total number of atoms involved in the transition. The instinct properties of the atomic system determine the value of τ_{21} , which ranges from μs for rarified gases to ns for semiconductors. [100-102]

Fig.5-1(b) shows the transition process of amplified emission. In a two-level atom system as described above, an atom populates the excited state E_2 . Before this atom relaxes down to the

ground state E_1 through spontaneous emission, it can be perturbed by the electro-magnetic field of an incident photon, which is emitted from spontaneous emission with energy $h\nu = E_2 - E_1$. Under the perturbation, this atom might transit to ground state E_1 , emitting a photon with energy $h\nu = E_2 - E_1$. This photon emission process is called amplified spontaneous emission (ASE). After this transition, one photon $h\nu$ is turned into two photons.

ASE process can be described with the following equation [121]

$$\frac{dN}{dt} = -B_{21}\rho(\nu)N, \quad 5-3$$

where B_{21} is a stimulated emission probability, called Einstein B coefficient and $\rho(\nu)$ is the distribution function of radiation density of photons at frequency ν .

The relationship between A_{21} and B_{21} is given by [121]

$$\frac{A_{21}}{B_{21}} = \frac{\hbar\omega^3}{\pi^2c^2}. \quad 5-4$$

One important optical property of ASE is that the emitted photon is exactly same as the incident photon [121]. These two photons have the same optical frequency, spatial phase, optical polarization, and direction of propagation, which results in the coherence between them. Through ASE process, weak spontaneous emission can be amplified coherently in active medium.

However, ASE can occur for any photon created from spontaneous emission, and in a medium with a sufficiently large density of excited states, many spontaneously emitted photons can be exponentially amplified in different regions, such that light from different spatial regions are incoherent since they have different phases, polarizations and propagation directions. If an optical cavity is used to select a specific mode of ASE, a lasing effect can be observed since all other ASE processes are suppressed except the preferentially selected ASE mode.

In ASE process, in the low intensity regime, where $I(z) \ll I_s$, the amplification of emission intensity in the propagation direction z is written as

$$I(z) = I(0)e^{g_0 z}, \quad 5-5$$

in the high intensity saturated gain regime, where $I(z) \gg I_s$, the emission intensity is described by

$$I(z) = I(0) + I_s g_0 z. \quad 5-6$$

In equations 5-5 and 5-6, $I(0)$ is the intensity of light propagating in the medium at $z=0$, I_s is the saturation intensity (which depends on the medium and density of excited states), z is the light propagation direction, and $g_0 \approx N_2 \sigma_{21}$ is called optical gain, where σ_{21} is a probability factor called the stimulated-emission cross-section and usually very small $\sim 10^{-20} \text{ cm}^2$ [96].

From the two equations 5-5 and 5-6, we can see that in low intensity regime, the light intensity grows as an exponentially along the z direction; in high intensity regime, the intensity grows linearly along the z direction. The gain is said to saturate in high-intensity regime.

5.1.3 Coherent Emission Process--Superradiance or Superfluorescence

In SE or ASE processes, the separation between two atoms on excited states are relatively large, so that the electro-magnetic field induced by one atom does not interact with the other atom, and the electric dipole of each transition is not aligned nor has the same phase in the oscillation, which results in incoherence between different SE processes or ASE originating from different spontaneous emission processes, also resulting in incoherent emission.

However, in a N -atom ensemble, if the atoms in excited states are brought closer and closer, so that the electro-magnetic field radiated interact with many excited atoms (in macroscopic scale) simultaneously and all the atomic electro dipoles oscillate in phase before they start uncorrelated spontaneous emission, a coherent macroscopic dipole state can exist for a

short time. A very short burst of emission will occur, radiating strong coherent light. This ‘superemission’ process is called superradiance (SR) or superfluorescence (SF), depending on the nature of the initial formation of the macroscopic coherence. For SR, the coherence of atoms is from the external excitation source, i.e. polarized laser pulse, and excited atoms preserve the coherence before they emit photons. For SF, the atoms on excited state are initially incoherent, the coherence develop in the N atoms due to the interaction between them.

The SF emission is a macroscopic coherent effect in an ensemble of N atoms, in which all the N atoms radiate photons cooperatively and coherently. Fig.5-2 shows the processes of SF emission. Initially, an ensemble of N atoms populates the ground state. With photoexcitation from a laser pulse, the N atoms are excited and populate higher energy states. The N atoms preserve the coherence from the coherent laser pulses for a very short time and then lose the coherence before they start to transit to ground state. In this situation, the electro dipoles of N atoms are not aligned in phase. However, if the density is high enough, the electro dipoles could develop the coherence and get aligned and start to oscillate in phase spontaneously due to the interaction between them. A small number of electro dipoles of the N atoms could be aligned in phase spontaneously due to quantum fluctuation or thermal effect, and then this coherence of electro dipoles is developed to all the atoms through a very high gain mode ($\alpha \cdot L \gg 1$). The N atoms in the coherent state will emit coherent photons in a very short burst of pulse.

SR was first predicted theoretically by Dicke in 1954 [35] and first observed experimentally by Skribanovitz *et al.* [103] in hydrogen fluoride (HF) gas in 1973. Many experiments about SR and SF have been performed and reported in atom gas system [104-106]. In addition to experiments of SF, more theoretical work elucidating the nature of SF under

different conditions has also been done with either quantum field theory [107] or semiclassical theory [108].

In Dicke's SR theory, the cooperative emission of electro dipoles takes place under the following condition,

$$V \sim \lambda^3. \quad 5-7$$

Where V is the volume that excited atoms are confined and λ is the emission light wavelength.

From this condition, cooperative emission exists in a very small active medium volume.

However, Bonifacio *et al.* [107] and MacGillivray and Feld [108] extended the SF theory to optically thick medium (on the order of mm or cm), either a "pencil shape" geometry, in which the Fresnel number ($A/L\lambda$, where A is the cross section and L is the length of active medium) is not larger than 1 or a "disk shape", in which Fresnel number is much larger than 1.

In the description of SF, there are five time scales are involved: the "dephasing" times T_2 and T_2^* , the photon decay time τ_E , cooperative time τ_c and SF radiation time (or duration) τ_R , and coherent delay time τ_d . τ_E is the time of a photon transit time in the active medium, T_2 and T_2^* are the coherence relaxation time due to homogeneous and inhomogeneous broadening effect, τ_c is the characteristic exchange time of electro dipole coupled to radiation field, τ_R is the pulse duration of SF emission, and τ_d is the delay time, during which the spontaneous emission evolves into coherent emission.

The expressions of these time scales τ_c , τ_R and τ_d are given by [108]

$$\begin{aligned} \tau_R &= T_{spontaneous} (8\pi A / N\lambda^2 L) \\ \tau_c &= (g_0 \sqrt{N})^{-1}, g_0 = g_{k_0} = (ck_0 \mu^2 / 2\hbar)^{1/2}, \\ \tau_d &\approx \frac{T_R}{16} \ln(2\pi N)^2 \end{aligned} \quad 5-8$$

where T_{sp} is the spontaneous radiation time of an atom transits from high energy state to the lower energy state, N is the number density of atomic system, λ is the transition wavelength, g_{k0} is the coupling factor between electromagnetic field and electric dipole, which is a key factor in the evolution of coherent emission, k_0 is wave vector of central frequency of optical transition and μ is the dipole moment of atomic dipole. Another critical factor in the cooperative coherent emission is the cooperative length L_c , within which all the dipole oscillates in phase, resulting in the coherent emission. The expression of L_c is given by [108]

$$L_c = c / 2g_0 \sqrt{\rho}, \quad 5-9$$

where ρ is the density of atoms.

In Bonifacio's theory, the condition for cooperative emission of N atoms ensemble is given by [108]

$$\tau_c \ll \tau_R \ll \tau_d < T_2, T_2^*. \quad 5-10$$

Under this condition, initiated by quantum fluctuations or thermal radiation, a small number of atomic dipoles oscillates in phase and emit photons spontaneously, then through the coupling between atomic dipoles and electromagnetic field, the N atom oscillators ensemble develop into oscillatory phase matching state in delay time τ_d and radiate a short burst of coherent emission with pulse width τ_R . Eq. 5-10 stresses that the emission takes place before the N atoms oscillator become dephased at time T_2, T_2^* and the N atom oscillators develop into coherent state before they start to recombine.

Bonifacio also mentioned in his theory that the relationship between active medium length L and critical cooperative length L_c

In the case $L \ll L_c$ or $\tau_E < \tau_c$, photons leak out of the active medium before they interact with the atoms, the N atomic oscillators emit a pure SF, the intensity of pure SF is given below [108]

$$I(t) = \frac{g_0^2 N^2}{2kV} \exp\left(-\frac{1}{T_2^*}\right) \text{sech}^2\left(\frac{1}{\tau_R}(t - \tau_d)\right). \quad 5-11$$

We can see that the peak intensity of SF is proportional to N^2 and emission peak is at $t = \tau_d$.

In the case $L < L_c$, where $\tau_E > \tau_c$ the photons travel inside the active medium when the SF emission takes place, SF is still observable, however the emission pattern is oscillatory pattern instead of *sech*² pattern [108].

In the case $L > L_c$, the SF emission starts to get weaker and disappear, the emission process is dominated by ASE [108].

As shown in Eq.5-10, several requirements and characteristics for a system need to be satisfied to make SF emission observable. SF pulse duration τ_r and delay time between excitation and SF burst τ_d are much shorter than the spontaneous emission time $T_{\text{spontaneous}}$ and inhomogeneous dephasing time T^* ($\tau_r, \tau_d \ll T_{\text{spontaneous}}, T^*$) so that the electric dipoles can maintain their phase relation and emit coherent light before spontaneous emission occurs. Based on these requirements, rarified gas atom systems are the most favorable to observe SF emission, since they have relatively long $T_{\text{spontaneous}}$ and ($\sim \mu\text{s}$), and the SF pulse width and delay time is on the order of nanoseconds. Table 5-1 shows some of the time constant in the SF experiment done in Rb gas. By controlling the pressure of the atomic gas, SF emission pattern can be clearly resolved [109, 110]. However, in a solid-state system, i.e. semiconductors, the dephasing time T_2, T_2^* are extremely small ($\sim 1\text{ps}$) [111], and the conditions in 5-10 are very difficult to satisfy. Thus, up until this work, it has been impossible to observe SF emission in semiconductors.

5.1.4 Theory of Coherent Emission Process--SR or SF in Dielectric Medium

In 1964, A. P. Kazantsev [112] reported the first theoretical results of collective emission processes in a two level system of a dielectric medium, such as a semiconductor. He found that if the electromagnetic field interacts with two level systems resonantly, the field amplitude is modulated with a characteristic frequency Ω , which is the coupling between electric field and two level systems. The two prerequisites in Kazantsev's theory can be expressed as

$$\gamma = \frac{E^2}{N\hbar\omega_0} \leq 1, \quad 5-12$$

$$\Omega\tau \geq 1, \quad 5-13$$

where τ is the relaxation time of two level system, $N\hbar\omega_0$ is the energy stored in N atom system.

Also, three simplifications of the two level system in Kazantsev's theory are made, (1) the dielectric medium is infinite and sufficiently rarefied, in which case the $\Omega \ll \omega_0$, (2) the medium is a two level system and (3) there is no dissipation in the two level system so that $1/\tau \sim 0$, only the early time ($t \ll \tau$) is considered.

With the conditions shown above, the intensity of radiation is given by

$$|E(t)|^2 \sim |E_0|^2 \exp(t\Omega)$$

$$\Omega^2 \sim Nd^2\omega_0, \quad 5-14$$

where E_0 is the initial value of electric field, d is dipole momentum, N is the density of activated atoms and ω_0 is the transition frequency. It can be seen that the intensity of field increases exponentially and dramatically if the collective modulation frequency Ω is large enough.

Zheleznyakov and Kocharovsky [113] applied the idea of cooperative frequency, which couples the electric magnetic field and optical polarization P in the medium, to the coherent

process of polarization wave function in dielectric medium, and the cooperative frequency is given by

$$\omega_c = (8\pi d^2 \Delta N \omega_0 / 3\hbar), \quad 5-15$$

Where $\Delta N = N_2 - N_1$, which represents the maximum population inversion density in the two level system.

Belyanin *et al.* [114-118] calculated the Maxwell-Bloch equations for resonant interactions between active medium and radiation field in semiconductors. In the mean field approximation, the slowly varying electromagnetic field $E(k)$, macroscopic polarization wave P_k , and inversion density ΔN_k can be described via a coupled set of equations:

$$\frac{d^2 E}{dt^2} + \frac{1}{T_E} \frac{dE}{dt} + \omega_0^2 E = -4\pi P_k, \quad 5-16a$$

$$\frac{d^2 P_k}{dt^2} + \frac{2}{T_2} \frac{dP_k}{dt} + \omega_0^2 P_k = -\frac{\omega_c^2 E}{4\pi}, \quad 5-16b$$

$$\frac{d\Delta N_k}{dt} + \frac{(\Delta N_k - \Delta N_k^p)}{T_1} = \frac{2}{\hbar\omega_0} E^* \frac{dP_k}{dt}. \quad 5-16c$$

Here, E is the electric field and P_k is the optical polarization oscillating at frequency ω_0 . The subscript k refers to electron-hole pair with quasi-momentum k , T_E is the photon life time for a given field mode, T_1 is the relaxation time of excited state, T_2 is the dephasing time of dipoles, d is the transition dipole moment, n is the refractive index, and ΔN_k^p is the inversion density excited by pumping.

From these three equations, we can see that E and P are coupled, with the cooperative frequency ω_c (and thus the density) determining the coupling strength and resulting emission. The left hand side of 5-16 (a) and (b) for E and P are harmonic oscillators with damping factors

T_E , T_2 , and right hand sides are driving force on the oscillators. However, the increasing rate of E and P strongly depends on the value of ω_c , which couples the E and P and dominates the increasing rate of E and P . The driving force ω_c on RHS of 5-16 (b) should be associated with excited atom density and electric dipoles, and transition frequency in the E and P resonant interaction, as shown in Eq.5-15. If an initial value of ω_c is sufficiently large, equation 5-16 exhibit instability with respect to the growth of small initial oscillations of the E and P .

Given that

$$\frac{\omega_c}{2} > \frac{1}{T_E}, \quad 5-17$$

equations 5-16 can be solved approximately in two regime [111].

First is amplified spontaneous emission regime. In this case, we have

$$\frac{\omega_c}{2} \ll \frac{1}{T_2}, \quad 5-18$$

and the growth rate is given by

$$\omega'' = \frac{\omega_c}{4} T_2 - \frac{1}{T_E}. \quad 5-19$$

In order to get amplified, then we should have $\omega'' = \frac{\omega_c}{4} T_2 - \frac{1}{T_E} > 0$.

Second is SF regime. In this case, we have

$$\frac{\omega_c}{2} \gg \frac{1}{T_2}, \quad 5-20$$

and the maximum growth rate of emission intensity is given by

$$\omega'' \approx \frac{\omega_c}{2}. \quad 5-21$$

The SF pulse width τ_R and coherent length L_c can be estimated with the value of ω_c , also the delay time τ_D , which characterize the coherent generation can be given as [111]

$$\begin{aligned}\tau_R &\sim \frac{2}{\omega''} \\ L_c &\approx \frac{c}{\omega'' n} \times \text{Log}(factor10 - 20). \\ \tau_D &\sim \frac{1}{\sqrt{2\omega''}} \log(E_{\max} / E_{\min})\end{aligned}\tag{5-22}$$

From the cooperative frequency ω_c , many parameters can be derived. The SF pulse duration scales as

$$\tau_{SF} \sim \frac{1}{\omega_c} \sim N^{-\frac{1}{2}},\tag{5-23}$$

and the peak intensity of SF scales as

$$I_{SF} \sim \frac{\hbar\omega N}{\tau_{SF}} \sim N^{\frac{3}{2}}.\tag{5-24}$$

The line width of cooperative recombination, which is determined by the band filling of particle states in QW or QD scales as

$$\Delta\omega \sim \Delta\omega_c \sim N^{\frac{1}{2}}.\tag{5-25}$$

5.2 Cooperative Recombination Processes in Semiconductor QWs in High Magnetic Fields

Naturally, in solid-state systems such as semiconductors, it is quite difficult to observe SR or SF since T_2 in solid-state system is very small (on the order of ps). The ensemble of dipole oscillators formed by electrons and holes cannot build up coherence before they undergo phase breaking, since the electron and holes are not localized and easily be involved in collisions such as electron-phonon, electron-electron, and electron-hole collisions. However, Belyanin pointed out that in quantized semiconductors, such as a semiconductor QW in high magnetic field or QD,

the electron and hole are spatially confined. This confinement reduces the collision probability and can dramatically increase the dephasing time T_2 . Meanwhile, the density of states of QW and QD increase dramatically compared to that of a 3D bulk semiconductor (see chapter 3, equation 3-10 and Fig.3-4). This effect implies that instead of populating in the continuum states in a bulk semiconductor, electrons and holes mainly confine themselves around the quantized energy levels because the continuum states are depleted in QW and QD structure. In this case, the number of dipoles formed by electrons and holes increase significantly at QW energies level E_1 , E_2 , which satisfy the high density of “atoms” requirement of SF (see equation 5-20).

In a high magnetic field, the electron-hole pairs in a $\text{In}_x\text{GaAs}_{1-x}$ QW are effectively confined in a quasi-zero dimensional state, and manifests this 0D effect in the absorption spectrum and PL spectrum (see Fig. 4-4 and 4-7). The electron-hole pair only populate at discrete LL states, ensuring that the spreading of the electron-hole pair energies is small, favoring SF generation. Moreover, the density of state of LL levels for $\text{In}_x\text{GaAs}_{1-x}/\text{GaAs}$ QW is high ($\sim 10^{12}/\text{cm}^2$ at 20T, see Chap. 4, equation 4-13), which also give rise to the generation of cooperative phenomena.

5.2.1 Characteristics of SF Emitted from InGaAs QW in High Magnetic Field.

As mentioned before, semiconductor nanostructures such as QWs or QDs are an ideal system to observe cooperative recombination of electron-hole pairs, therefore we chose $\text{In}_x\text{GaAs}_{1-x}/\text{GaAs}$ multiple QWs as our emission medium, using ultrafast excitation and high magnetic field in combination to observe SF. The structure of this sample has been discussed in 4-3 and Fig.4-2.

According to the results shown above (Eqs. 5-17 to 5-21), the key term that determines the growth rate of emission intensity I , which corresponds to the cooperative emission process is the cooperative frequency ω_c .

In a two-dimensional semiconductor quantum well structure, the cooperative frequency is modified into the following form [114],

$$\omega_c = \sqrt{\frac{8\pi^2 d^2 \Delta N \Gamma c}{\hbar n^2 \lambda L_{QW}}} \quad 5-26$$

Here L_{QW} is quantum well of thickness, λ is emission wavelength, Γ is the effective overlap factor of electromagnetic field with the quantum well in the direction perpendicular to well plane, n is the refractive index and d is the transition dipole. The maximum photo excited electron-hole density is $\Delta N \sim N_{e-h}$.

Based on the theory presented above, we can estimate the parameters for SF emission in the $\text{In}_x\text{GaAs}_{1-x}/\text{GaAs}$ used in these experiments.

The photon decay time is $\tau_E \sim \frac{Ln\sqrt{F}}{c} \sim 2 \times 10^{-13} \text{ s}^{-1}$, where L is the active medium length, F is the Fresnel number. In reality, $4 \times 10^{-13} \text{ s}^{-1}$ seems to be a better estimate because the excited medium can guide the SF emission into the active medium. This waveguide effect is generated after medium is excited, due to an enhancement in the refractive index medium in the active area from the magneto-plasma, In this case the electro magnetic field will couple more with optical polarization.

The cooperative frequency at initial time is given by equation 5-26, where ΔN is carrier density in the quantum well plane, and Γ is around 1/3. The estimation of cooperative is

$\omega_c \sim \sqrt{\frac{N}{10^{12} \text{ cm}^{-2}}} \times 3 \times 10^{13} \text{ s}^{-1}$. In equation 5-20, in order to make the condition for SF satisfied, T_2 is $\sim 10^{-13} \text{ s}^{-1}$, and we need $N > 5 \times 10^{11} \text{ cm}^{-2}$, which can be realized at high magnetic field (~ 20 Tesla) and ultrafast pumping (see chapter 3, equation 3-14).

Below, we present investigations of the magneto-PL spectrum obtained from high-density electron-hole plasmas in $\text{In}_x\text{GaAs}_{1-x}/\text{GaAs}$ QW in high magnetic fields, in which propagation of PL is perpendicular and parallel to the QW plane. Perpendicular to the QW plane, abnormally sharp and strong emission lines from 0-0 and 1-1 LLs are observed as discussed in chapter 4. As we have discussed above, there is possibility that this emission is from ASE or macroscopic cooperative recombination--SF. Since the electron-hole pairs are mainly populating in the QW plane, the in-plane PL should be much stronger than the PL collected perpendicular to the plane because the spontaneous emission should be amplified when propagating in the in-plane path. Thus, we have developed experiments in new configurations to measure the in plane PL from $\text{In}_x\text{GaAs}_{1-x}/\text{GaAs}$ QW.

In order to show definitive evidence of cooperative recombination in QWs in high magnetic fields, there are a number of experimental signatures that uniquely characterize SF emission. These are listed in Table 5-2. For comparison, we also include the ASE characteristics in the Table 5-2, since PL emission in $\text{In}_x\text{GaAs}_{1-x}/\text{GaAs}$ QWs at high magnetic fields could be due to either emission mechanism. From these six characteristics, we can distinguish a pure SF process from ASE processes, and they are given as follows.

5.2.2 Single Shot Random Directionality of PL Emission

In an SF emission process, the coherent collective emission builds up stochastically from spontaneous emission, which can be emitted in any direction, and a specific SF burst will follow the propagation direction that the first spontaneous emission takes. It is essential to note that since this is a probabilistic quantum electro-dynamic process, each SF burst forms independently on each subsequent excitation laser pulse. By contrast, in ASE processes many spontaneous emissions could be amplified, therefore, in a single shot, the PL emission should equally distribute in all direction and no random directionality is expected.

5.2.3 Time Delay between the Excitation Pulse and Emission

As we seen in Eq. 5-21, the SF emission is given after the excitation pulse, the delay time between is τ_d , during which the spontaneous emission develops into SF through an extremely high gain mode. This delay occurs because of the inherent build up time for the coherence form from the initially incoherent dipole population. In ASE, the emission process start in a short time (on the order of $nl / c < \tau_d$, where c is the speed of light and l is the length of activated medium and n is the refractive index) immediately after the excitation pulse disappears, therefore, no time τ_d delay is expected to be observed.

5.2.4 Linewidth Effect with the Carrier Density

In the formation of ASE, spontaneous emission is amplified when travels through medium, however, the amplified emission linewidth depends on the gain function $G(\omega)$, which is given below,

$$I(\omega) = I_0(\omega) \bullet \exp(G(\omega)L). \quad 5-27$$

Where $I_0(\omega)$ is the initial intensity function in frequency domain and L is active medium that light get amplified. Usually, $G(\omega)$ has Gaussian or Lorentz shape, which result in the center frequency in $I(\omega)$ get amplified more than frequency off center. This gain narrowing effect reduces the emission linewidth in ASE process.

In SF process, as mentioned above in Eq. 5-22, the linewidth of cooperative emission is broadened at high densities, $\Delta\omega \sim N_{e-h}^{1/2}$, since more carriers are involved in the cooperative emission.

5.2.5 Emission intensity Effect with Carrier Density

In an ASE process, emission is amplified linearly with N , so that the emission intensity should increase linearly with the increasing of carrier density N . In an SF process, according to

equation 5-23 the emission is a short burst and given coherently, superlinear increasing of the emission intensity is expected when carrier density N is increased.

In magnetic field, the carrier density N depends on the magnetic field strength B (see chap.3, equation 3-14), the linear relation between them is $N \sim B$, so a superlinear relation, $I \sim B^{3/2}$, between emission intensity and magnetic field is expected in SF emission.

5.2.6 Threshold Behavior

Both ASE and SF exhibit threshold behavior with respect to laser excitation intensity. However, in ASE, the threshold is at the point where optical gain $G > 0$, while in SF, the threshold is the point where coherence is built up among carriers.

5.2.7 Exponential Growth of Emission Strength with the Excited Area

Both ASE and SF will be amplified in the form of $I \sim I_0 \exp(\alpha \cdot L)$, so that the emission strength increases exponentially with respect to the excited area. Therefore this doesn't distinguish between ASE and SF, but does show that an exponential process is occurring.

We expect to see cooperative emission from high carrier density electro-hole plasma in $\text{In}_x\text{GaAs}_{1-x}/\text{GaAs}$ QW in high magnetic field, however, in order to fully fill the LL and make the carriers populate on LL before they start to recombine (time scale $\sim 100\text{ps}$), a high power (GW/cm^2) ultrafast CPA laser is needed to generate enough carrier density in a very short time ($\sim \text{ps}$). It is also critical to note that the initial excitation at 800 nm, is well above (240meV) the 0-0 LL levels that we probe (at 920nm). In fact we excite electrons carrier into GaAs barrier continuum states and $\text{In}_x\text{Ga}_{1-x}\text{As}$ well continuum states., Most of electrons carriers populating in barrier are dumped into the $\text{In}_x\text{Ga}_{1-x}\text{As}$ QW layer and increase the carrier density in well layers. Carriers in QW layers will relax down to 0-0, 1-1... LL levels and there are many collisions during the energy relaxation (and momentum relaxation) which completely destroys the initial

coherence of carriers imposed by the laser. Thus, we can be truly probing SF as opposed to SR. After energy relaxation to the QW LLs, the carriers, now tightly confined both in space and energy, develop into a coherent state with interacting with the electromagnetic field from initial spontaneous emission and give a burst of SF emission. This process shows the key signature of SF instead of SR.

5.3 Experiments and Setup

To understand the PL emission processes in $\text{In}_x\text{GaAs}_{1-x}/\text{GaAs}$ QWs excited with high intensity short laser pulses at high magnetic fields, several experiments have been carried out.

- Magnetic field and excitation power dependent in-plane PL
- Single shot experiment for random directionality of in-plane PL
- Control of coherence of the in plane PL from $\text{In}_x\text{Ga}_{1-x}\text{As}$ QW in high magnetic field.

In all the experiments, we use the ultrafast magneto-optics facility developed by us at the NHMFL (see chap2, Figs.2-2, 2-3, and 2-4.). All the experiments are done at liquid helium temperature with the Janis optical cryostat designed for a resistive magnet. The $\text{In}_x\text{GaAs}_{1-x}/\text{GaAs}$ QW sample is mounted on the liquid He tail of cryostat for direct optics, in which laser beam can travel in free space and then excite the sample without being chirped.

For most of the experiments, the ultrafast CPA laser system is the excitation light source, which has been introduced in Chap.4, 4.3. The excitation laser is focused on the $\text{In}_x\text{Ga}_{1-x}\text{As}$ QW sample with one 1 m focal length lens, and the spot size on sample is around $500 \mu\text{m}$.

The configuration of the in plane PL collection geometry is shown in Fig. 5-3. In order to collect the PL travels in the QW planes, a small right angle roof prisms is mounted on the edge of the QW sample, which can steer the in plane light into the optical multimode fiber mounted right on the top of the prism. The area of prism is $1.0 \times 1.0 \text{mm}^2$, and the fiber diameter is $600 \mu\text{m}$.

The collection angle for this prism is approximately 40° . With this configuration, PL emission travels in the QW plane is effectively and efficiently collected and delivered to a McPherson spectrometer for analysis. In addition, for comparison with the in-plane PL, PL emission perpendicular to the QW planes is collected via a fiber on the back face of the sample.

The magnet used for study of cooperative emission is Bitter resistive magnet located in cell 5 at NHMFL, a 25 Tesla (upgraded to 31 Tesla now) wide bore (50 mm) magnet (see Fig.2-1).

Most of our spectra were collected by averaging over multiple shots (1000 shots in most cases). However, to probe the directionality of the emission, in which the PL propagation is different from pulse to pulse, single shot experiments need to be performed to resolve this phenomenon. Thus, we measured the PL from $\text{In}_x\text{GaAs}_{1-x}/\text{GaAs}$ QWs excited by one single laser pulse. An electro-optical Pockel cell was employed in this experiment. As shown in Fig. 5-4, the laser beam propagates through two crossed polarizers and gets rejected at the second polarizer. However, there is fast transient high voltage bias nonlinear crystal positioned between the two polarizers, which operate as a transient half wave plate when the high voltage bias is on. Each time when the high voltage is on, the high voltage biased crystal changes the polarization of laser beam by 90 degree and let it go through the second polarizer. With this device, we can control the number of laser pulses and the repetition rate of the pulses that are sent to the sample and collect PL from a single excitation pulse.

Also, in order to compare the PL intensity at different in plane directions, two small right angle prisms are mounted at cleaved edges 90° apart of InGaAs/As QW, which will simultaneously collect the PL excited with one CPA pulse and steer into two fibers mounted on top of roof prism. The excitation geometry of single shot measurement is shown in Fig.5-8

5.4 Experimental Results and Discussion

5.4.1 Magnetic Field and Power Dependence of PL

We measured the field dependency in plane PL emission spectrum of $\text{In}_x\text{Ga}_{1-x}\text{As}/\text{GaAs}$ QW excited with 150fs CPA laser pulses at a constant laser fluence ($F_{\text{laser}} \sim 0.62 \text{ mJ/cm}^2$) up to 25 Tesla. Experimental result is shown in Figure 5-5(a). For comparison, PL collected at the same conditions with the center fiber is also shown in Fig. 5-5(b). The sharp in the edge collection PL spectrum is a lot stronger than the PL from center collection. Broad PL emissions due to spontaneous emission from inter band LL transition are observed up to 12 Tesla. This broad linewidth ($\sim 9 \text{ meV}$) is due to inhomogeneous broadening, which originates from the inhomogeneities and possibly defects in the multiple QW layers. The magnetic field dependent PL features above 13 T change dramatically, and sharp peaks (around $\sim 2 \text{ meV}$) are observed on high energy side of broad feature of each interband LL transition. These sharp peaks dominate the PL at high magnetic field. However, each inter LL transition PL peak consist of overlapping broad and sharp peaks, shown in Fig.5-6. The sharp peaks are believed to be ASE or SF and their linewidth is determined through homogeneous broadening, since the emission concentrates around a narrow frequency. We fit the field dependent PL strength of 0-0 LL transitions with a combination of Gaussian function (for inhomogeneous broadening line width) and Lorentz function (for homogeneous broadening line width) given below.

Gaussian function

$$I(\omega) = A \exp\left(-\frac{(\omega - \omega_0)^2}{w}\right), \quad 5-28$$

where $1.386 w$ is the FWHM (full width at half maximum) linewidth, ω_0 is the center frequency of PL transition.

Lorentzian function

$$I(\omega) = B \left(\frac{w}{(\omega - \omega_0)^2 + w^2} \right), \quad 5-29$$

where w is the FWHM and ω_0 is the center frequency of PL transition.

The fitting results of sharp peak emission strength (black dot) and linewidth (red dot) of PL from 0-0 LL transitions vs. the magnetic field strength are shown in Fig.5-5 (c). In Fig.5-7(a) at a fixed magnetic field of 20 T, the PL spectrum of interband LL transition vs. excitation laser fluence is plotted. It is observed that below certain laser fluence (0.01 mJ/cm^2), only broad PL peaks with linewidth ($\sim 9 \text{ meV}$) exist, but with the increasing of laser Fluence, a sharp peak starts to emerge on the high energy side of broad peak. At the highest excitation laser fluences, the sharp peak dominates the PL emission spectrum. With the same fitting procedure as used for the magnetic field dependent PL spectrum, laser fluence dependent emission strength and linewidth of sharp PL peak from interband 0-0 LL transition are obtained and shown in Fig 5-7(b).

Identical field and laser fluence dependent PL spectra are seen when collecting from the center fiber above the pump spot, i.e., out of plane, although at a much lower signal level ($\sim 1/1000$). Also, increasing or decreasing the pump spot size resulted in the emergence of sharp PL features in the spectra at a given fluence. Thus, the observed behavior is not due to a spatially or spectrally inhomogeneous distribution of carriers.

Comparing the fitting results in Fig. 5-5(b) and 5-7(b), we can see similar patterns in curves of magnetic field or laser fluence dependent emission strength and linewidth. There are a few regimes in the two set of curves. First, below 12 T (or 0.01 mJ/cm^2), narrow emission is not observed. In the range 12–14 Tesla or ($0.01\text{--}0.03 \text{ mJ/cm}^2$), the narrow peak signal strength S grows linearly ($S \sim B$ or F_{laser} , see green lines)) with respect to both B and F_{laser} . Second, above 14 T (0.03 mJ/cm^2), the emission strength S starts to show a superlinear increase ($S \sim B^{3/2}$, see blue lines) with respect to B or F_{laser} . Above 0.2 mJ/cm^2 (see Fig. 5-7(b)), the signal resumes a linear

scaling. Also, the field and F_{laser} dependent PL linewidths curve (red circles) plotted in Figs. 5-5(b) and 5-7(b) reveal a remarkable correlation with the field and fluence dependent emission strength curve. In the linear regime, the linewidth decreases monotonically both versus B and F_{laser} until the emission becomes superlinear at the threshold point ($B=12\text{T}$ and $F_{\text{laser}}=0.01\text{mJcm}^{-2}$), where the PL linewidth begins to increase.

At a 20 Tesla, setting the excitation spot diameter at 0.5mm, 0.1mm and 3mm, we also measured on fluence dependent PL spectrum respectively. The fitting results of emission strength and linewidth at different excitation spot sizes are plotted in Fig. 5-8 (b) (c) and (d), narrow emission was observed, but both the integrated signal S and the linewidth exhibited qualitatively different scaling for each different spot size. The curve in Fig. 5-8(b) shows the increasing pattern with increasing laser fluence as shown before (See Chap. 5-4, II), however, the emitted signal S in (c) and (d) shows an almost linear relation with respect to the F_{laser} ($S \sim F_{\text{laser}}$), and in both of (c) and (d), and the linewidth curves monotonically decreased with increasing fluence.

5.4.2 Single Shot Experiment for Random Directionality of In Plane PL

With an optical Pockel cell, we are able to reduce the repetition rate of CPA laser to very low frequency ($\sim 20\text{Hz}$) so that we can use the mechanical shutter (speed $\sim 20\text{ms}$) on McPherson spectrometer to record the PL spectrum from a single CPA laser pulse excitation. Also we collect the in plane PL with two optical fibers simultaneously (the fibers are mounted on QW edges perpendicular to each other (see Fig. 5-4)), then deliver them to spectrometer to resolve the PL spectrum propagating in different directions in QW. This measurement is crucial for determining the correlation of the emission and single shot directionality of the in plane PL emission. Figure 5-4 presents the directionality measurements of the emission for a single pulse excitation. Figure 5-9 (a) illustrates a series of spectra upon single pulse excitation at a given fluence in the

superlinear emission regime ($F_{\text{laser}} 9.7 \text{ mJ/cm}^2$, $B=25 \text{ T}$) for a 0.5 mm diameter spot size. The spectra are collected through fibers on edge 1 (black) and edge 2 (red). We can see that the relative height between the red and black curve changes from shot to shot, which indicates that the propagation direction of in plane PL could be different from pulse to pulse since the two optical fibers are mounted to collect PL propagating in different directions. Since the two optical fibers have different collection efficiency, in Fig.5-9 (b) we displayed the maximum peak height from each edge (normalized to 1.0) versus shot number for the pumping conditions shown in Fig. 5-10(a). The maximum observed emission strength in Fig. 5-9(b) fluctuates as much as 8 times the minimum value, far greater than the pump laser pulse fluctuation ($\sim 2\%$). This strong anticorrelation between signals received from different edges indicates a collimated but randomly changing emission direction from pulse to pulse, as expected for cooperative spontaneous emission.

At a lower excitation fluence in linear increasing regime $F_{\text{laser}} \sim 0.02 \text{ mJ/cm}^2$ (obtained with a 3 mm spot), we also measured the shot to shot PL spectra collected with the same configuration discussed above and show it in Fig 5-10(a). We observed qualitatively different emission strength behavior from high power excitation shown in 5-10(a). In Fig.5-10(a), the emission strength of different shot from the same optical fiber do not fluctuate as much as high power excitation. In Fig.5-10(b) we can see that the normalized (to 1) shot to shot PL emission strength at different collection direction are highly correlated instead of anti-correlated in high power excitation. Fig. 5-10(b) shows omnidirectional emission on every shot, as expected for ASE or SE.

5.4.3 Control of Chherence of In Plane PL from InGaAs QW in High Magnetic Field

As discussed in Chap. 5.3, the intensity of cooperative emission or ASE increases exponentially with respect to the active length of medium in the propagating direction. We

shaped the excitation laser pulse and probed the spatial and directional characteristics of the PL emission process (see Fig.5-11). Using a cylindrical lens to focus the excitation laser beam on the QW sample, we generate an elliptically shaped spot ('pencil geometry') for the excitation region. When the cylindrical lens is rotated, we change the active medium length of PL emission propagating towards the two right angle roof prisms. The emission strength collected from the prisms should change according to the rotation angle. We define the 0 degree angle at the point where in plane PL from edge one is at maximum. We measured the signal as a function of angle from 0 to 180 degree for $F_{\text{laser}} \sim 0.02 \text{ mJ/cm}^2$ and $B \sim 25 \text{ T}$ (shown in Fig. 5-12), from which we can see that the PL emission strength change dramatically with respect to the angle cylindrical lens. In the experiment, the maximum signal from edge one, which correspondent to activated length 1.5mm is at 90 degree, the minimum signal from edge one is at 0 degree, correspondent to activated length 0.5mm. The ratio of signal strength $\frac{I_{\text{max}}}{I_{\text{min}}} = 20$ corresponds to $\exp(1.5/0.5) \sim 20$, which is consistent with exponential increasing of emission strength vs. activated medium length in ASE or SF..

5.4.4 Discussion

With the analysis of all the experimental result shown in Fig. 5-5, 5-7, 5-8 and 5-10, we found that for the interband 0-0 LL transition, the scaling of the emission strength S , the linewidth evolution, and single shot emission directionality indicate the following evolution processes as excitation power F_{laser} and magnetic field strength B are increased: (i) In the low-density limit ($B < 12 \text{ T}$, $F_{\text{laser}} < 5 \mu\text{J/cm}^2$), excited $e-h$ pairs relax and radiate spontaneously through interband recombination. The emission is isotropic with an inhomogeneous Gaussian shape linewidth of $\sim 9 \text{ meV}$. This broad spontaneous emission can be seen in both Fig.5-5(a) at low magnetic field and in Fig. 5-7(a) at low laser fluence. (ii) At a critical fluence 0.01 mJ/cm^2

(at 20 T) and magnetic field $B \sim 12$ T (at $F_{laser} \sim 0.6$ mJ/cm²), a carrier population inversion is established with increasing magnetic field and excitation laser fluence, which increases the carrier density in QW (since $N \sim F_{laser}$ and $N \sim B$, see equation 3-14). In this case, ASE develops, leading to the emission of amplified pulses. Fig. 5-10 shows that ASE is simultaneously emitted in all directions in the plane. The reduction in linewidth with increasing fluence results from conventional gain narrowing discussed in section 5-2-1, in which spectral components near the maximum of the gain spectrum are preferentially amplified than components with greater detuning [see Figs. 5-5(a) below 17 T and Fig.5-7(a) below 0.03mJ/cm²]. In this high-gain regime, the spectral width reduces to 2 meV (FWHM), still larger than $2/T_2$. (iii) If we keep increasing the magnetic field and laser fluence, since the DOS and physical density in QW are sufficiently high at high magnetic field (at $B \sim 20$ T, $N \sim 10^{12}$ cm⁻²), the cooperative frequency ω_c exceeds $2/(T_2 T_2^*)^{1/2}$, the build-up time of coherence between transition dipoles are shorter than the decoherence time. The $e-h$ pairs establish a macroscopic dipole after a short delay time and emit an SF pulse through cooperative recombination (or a sequence of pulses, depending on the pump fluence and the size of the pumped area).

According to the theoretical expression of $\Delta\omega$ in cooperative emission regime, the linewidth of emission increase with increasing of laser fluence due to reduced pulse duration of cooperative emission, until eventually saturation (due to the filling of all available states) halts the further decrease in pulse duration (shown in Fig.5-7(b), above 0.2mJcm⁻²). The transition from ASE to cooperative emission at 0.03 mJ/cm² at 20 Tesla is shown in Fig. 5-7(b), we can see that the linewidth of emission starts to increase significantly, which is consistent with $\Delta\omega$ increasing with increasing of carrier density (predicted in Eq. 5-29).

In ASE, the spontaneous emission is amplified during propagation in certain direction. However, since there are many spontaneous emission photons propagating in different directions with subsequent amplification, we observe that in a single shot measurement, ASE emission distribute in all directions. Significantly, we find that unlike ASE, which should be emitted in all directions with the same intensity [see Fig. 5-10(b)], in this super linear regime the initial quantum fluctuations grow to a macroscopic level to establish coherence and lead to strong directional fluctuations from shot to shot [see Fig. 5-9(b)] This is consistent with the random direction distribution discussed in Chap5, 5.2.1 a. The linear scaling of linewidth vs F_{laser} above 0.1 mJ/cm^2 is a combined result of absorption saturation of the pump and saturation of SF emission.

As discussed in Chapter 5, the intensity of cooperative emission increasing super linearly with respect to increasing of carrier density ($I \sim N^{3/2}$). Since the carrier density is proportional to F_{laser} or B , we should expect observe $I \sim B^{3/2}$ or $I \sim F_{laser}^{3/2}$ in the experiments. However, since the data was collected in a time-integrated fashion with spectrometer and CCD, we cannot directly probe the peak SF intensity scaling mentioned before because the SF emission is on the order of hundreds femtoseconds. However, there are two lines of evidence indicating that the observed superlinear scaling is related to the formation of multiple SF pulses from the 0-0 LL transition. The superlinear increase for the 0-0 LL emission is accompanied by an emission decrease from higher LLs, indicating a fast depletion of the 0-0 level through SF followed by a rapid relaxation of $e-h$ pairs from higher LLs and subsequent reemission. Also, in the single pulse measurements shown in Fig. 5-9, data shows that the PL emissions collected from two fibers on different edges of QW sample are either correlated or anticorrelated in roughly equal proportion. This result indicates that fast relaxation from higher LLs refills the 0-0 LL, resulting in a second pulse of SF

emission in a random direction. On average, the two SF pulses in one excitation pulse are collected in two different edge takes 50% shots, and for the other 50% shots, the two SF pulse from one excitation go to the fiber on only one edge. This is in qualitative agreement with observations, in which 50% shots are correlated and 50% are anticorrelated.

One could argue about whether the observed emission characteristics are consistent with pure ASE (“lasing”), but this can be ruled out by examining the excitation power dependent experiments at 20 T at different excitation spot sizes. In Fig. 5-8(b), (c) and (d) three spot sizes 0.5 mm, 0.1 mm and 5 mm are selected for the experiments. We can see that, only in the S vs. F_{laser} curve with excitation with 0.5mm spot size, linear and super linear increasing behavior (the signature of cooperative emission) emerge. Also a gain region of 0.5 mm is consistent with the theoretical prediction of coherent length $L_c \sim c \tau_{\text{SF}} \text{Ln}(I_{\text{SF}} / I_{\text{SE}})$, which is found to be a few hundred micrometers. However, in the $S \sim F_{\text{laser}}$ curve with 5mm excitation spot size, we only observe linear increasing behavior, this is a typical ASE process, also the linewidth of the PL emission keeps decreasing with increasing of F_{laser} , which is the gain narrowing effect in ASE. In the curve with excitation spot 0.1mm, we can see that the linewidth decreases up to certain F_{laser} , ($\sim 0.6 \text{mJcm}^{-2}$), then it stop decreasing. Also we can see that the emission strength S is neither linearly nor superlinearly increasing with F_{laser} , increasing. The PL emission with 0.1 mm excitation spot might be a combination of ASE and SF or early stage in SF. In the case that the excitation spot size is either much larger or much smaller than the coherent length, and none optical cooperative emission signature is observed.

We can conclude that collimated, randomly directed emission and superlinear scaling are observed *only* when the pumped spot is 0.5 mm, approximately equal to the theoretically

predicted coherence length for SF emission in QWs. They are not observed for 0.1 and 3 mm spot sizes.

Finally, contrary to popular opinion in the quantum optics community, pure SF does not require a rod like geometry. As shown in ref. [119], cooperative recombination is not constrained by the geometry of the excitation region, omnidirectional superfluorescent emission has been observed in cesium. Moreover, the disk-like geometry of the pumped active region allows us to observe the key evidence for SF, namely, strong shot-to-shot fluctuations in the emission direction. Previous experiments almost exclusively employed a rod-like geometry, in which the only direct signature of SF is the macroscopic fluctuations of the delay time of the SF pulse and pulse duration.

In a semiconductor system the SF pulse duration and delay time for cooperative emission would be manifested on the ps and sub-ps scale and we need to employ ultrafast spectroscopic method such as pump probe spectroscopy, time resolved upconversion PL spectroscopy and time resolved PL spectroscopy with a streak camera to observe these time parameters. Those experiments are underway at present.

5.5 Summary

In this chapter we have reported on a series of experiments to generate SF in semiconductor quantum wells. Excited with high peak power CPA laser, we observed extraordinarily strong in-plane PL emission from $\text{In}_x\text{Ga}_{1-x}\text{As}/\text{GaAs}$ multiple quantum wells at high magnetic field. With increasing carrier density, there are three regimes in emission from the interband 0-0 LL transition, spontaneous emission, amplified spontaneous and cooperative superfluorescent emission. In the SF regimes, all the experimental observations are in consistent with the optical signatures of cooperative emission process.

Table 5-1. Some experimental conditions for observation of super fluorescence in HF gas. The time unit is nanoseconds, L is the length of activated gas, and d is the size of laser beam.

Active length (cm)	d (μm)	T_2^*	τ_E	τ_R	τ_D	αL
5.0	432	5	0.17	0.15	6-20	35
3.6	366	32	0.07	0.15	5-35	180
2.0	273	5	0.35	0.12	6-25	45

Reprint with permission from M. Gibbs *et al.*, Phys. Rev. Lett. **39** (1977), page 549.

Table 5-2. Characteristics of SF emitted from InGaAs QW in high magnetic field

Characteristics	Superfluorescence(SF)	Amplified Spontaneous Emission(ASE)
Shot to shot random directionality	Yes	No
Pulse delayed by τ_d (~10ps)	Yes	No
Emission linewidth increase with carrier density N	Yes	No
Emission strength increase with excitation density	Superlinear ($\sim I^{1.5}$)	Linear ($\sim I$)
Threshold behavior	Yes	Yes
Exponential growth with area ($\sim \exp(gL)$)	Yes	Yes

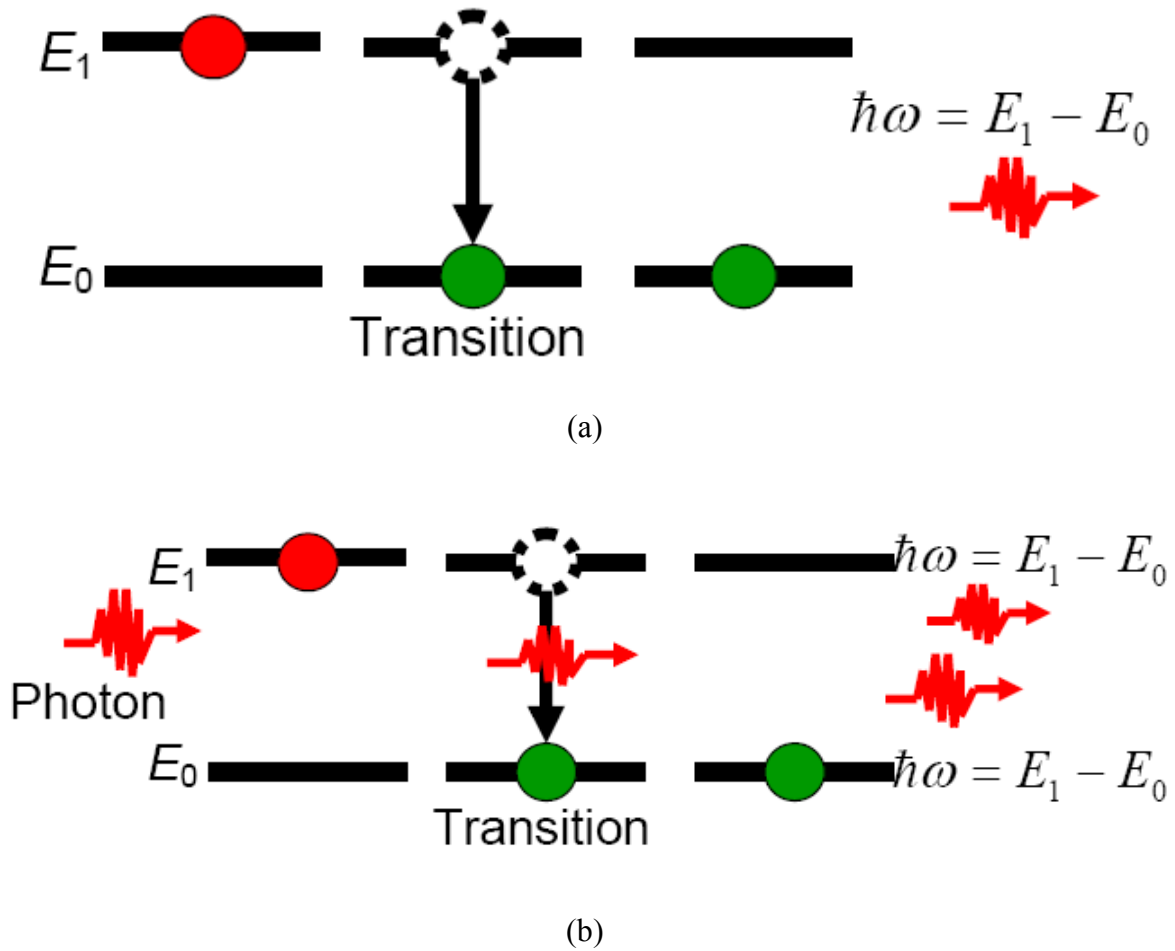


Figure 5-1. Spontaneous emission and amplified spontaneous emission process of a two level atom system.(a) Spontaneous emission (SE); (b) Amplified spontaneous emission (ASE).

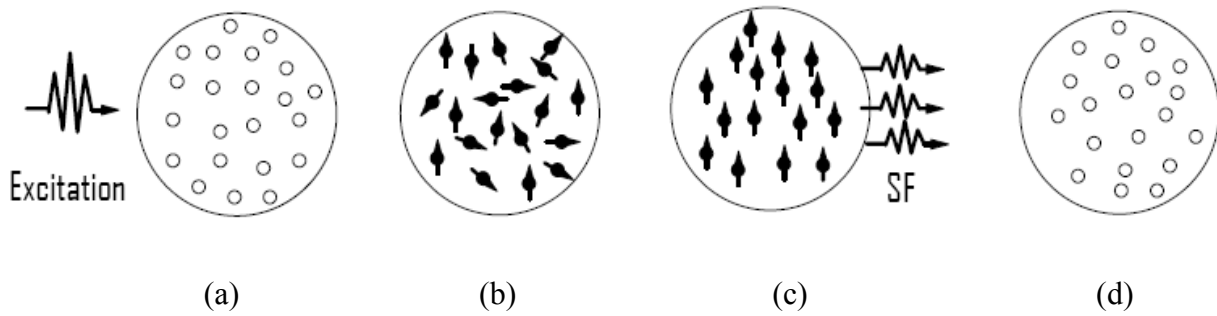


Figure 5-2. Four steps in the formation of collective spontaneous emission--SF in Natom system. (a) N atoms are excited by light absorption;(b) After excitation, the dipoles of the N two level atom randomly distribute in all direction; (c) Electric dipoles are aligned and phase matched; (d) All the electric dipoles emit simultaneously a burst of coherent light pulse.

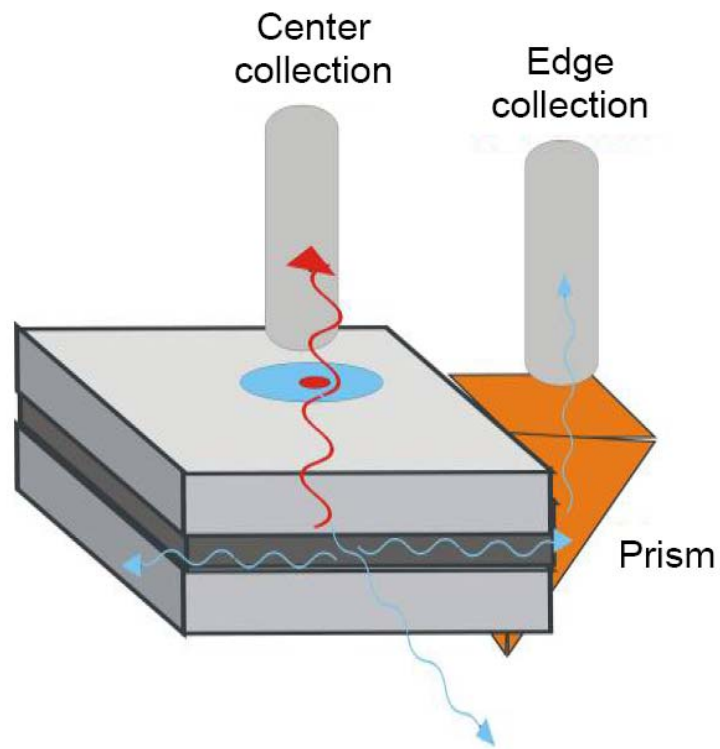


Figure 5-3. Configuration for collection of in plane PL from InGaAs multiple QW in high magnetic field. One right angle prism is positioned at the edge of QW sample to collect in plane PL.

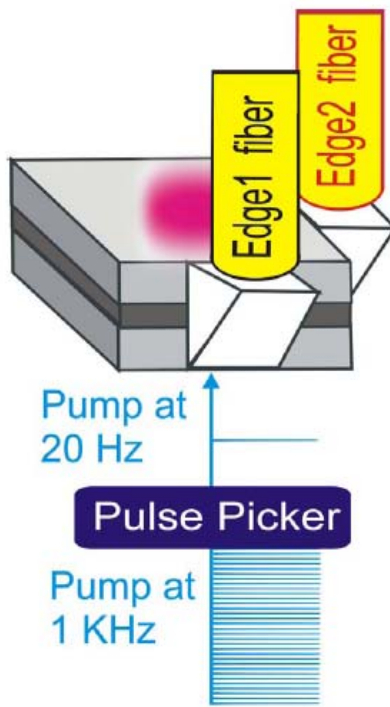


Figure 5-4. Configuration for a single shot experiment on $\text{In}_x\text{Ga}_{1-x}\text{As}$ Multiple QWs.

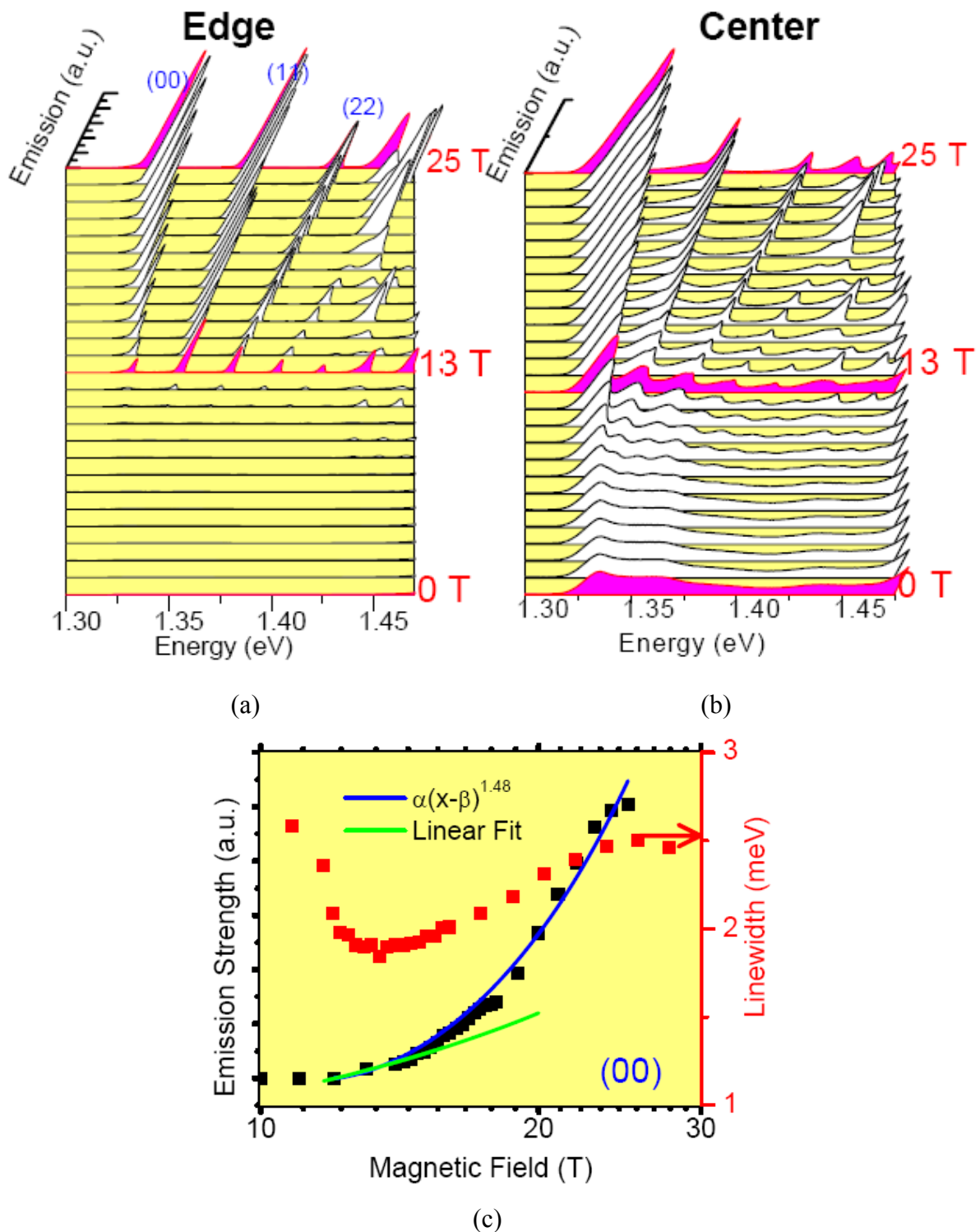


Figure 5-5. Magnetic field dependent PL spectrum and fitting results of in plane emission. (a) Field dependent PL emission spectrum from edge collection; (b) Field dependent PL emission spectrum from center collection and (c) Fitting results of emission strength and linewidth.

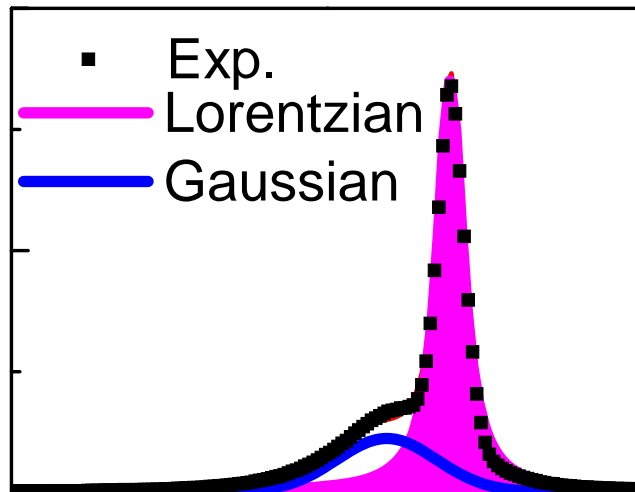


Figure 5-6. Fitting method to determine line widths using a Lorentzian and Gaussian function for the sharp peak and broader lower-energy peak. The broad peak (blue line) is Gaussian shape originates from spontaneous emission, while the sharp peak (pink line) is Lorentz shape originates ASE or SF.

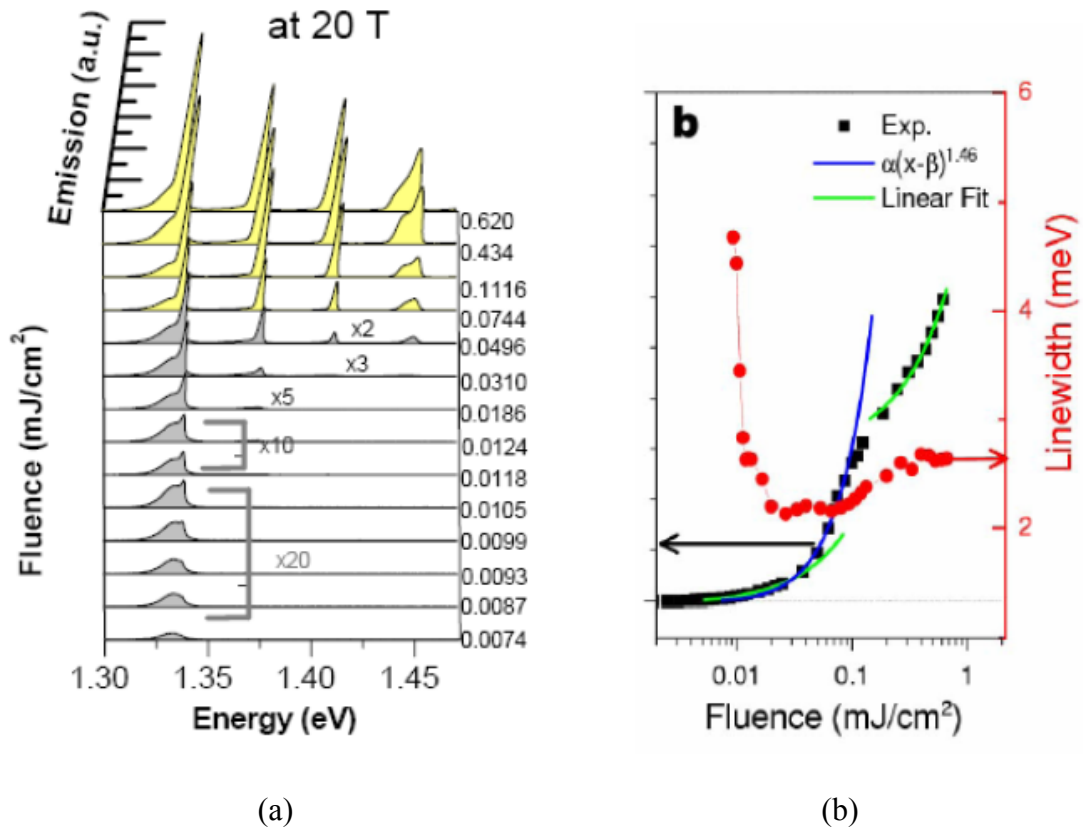


Figure 5-7. Excitation power dependent PL spectrum and fitting results of in plane emission. (a) excitation power dependent PL emission spectrum at 20 Tesla and (b) fitting results of emission strength and linewidth.

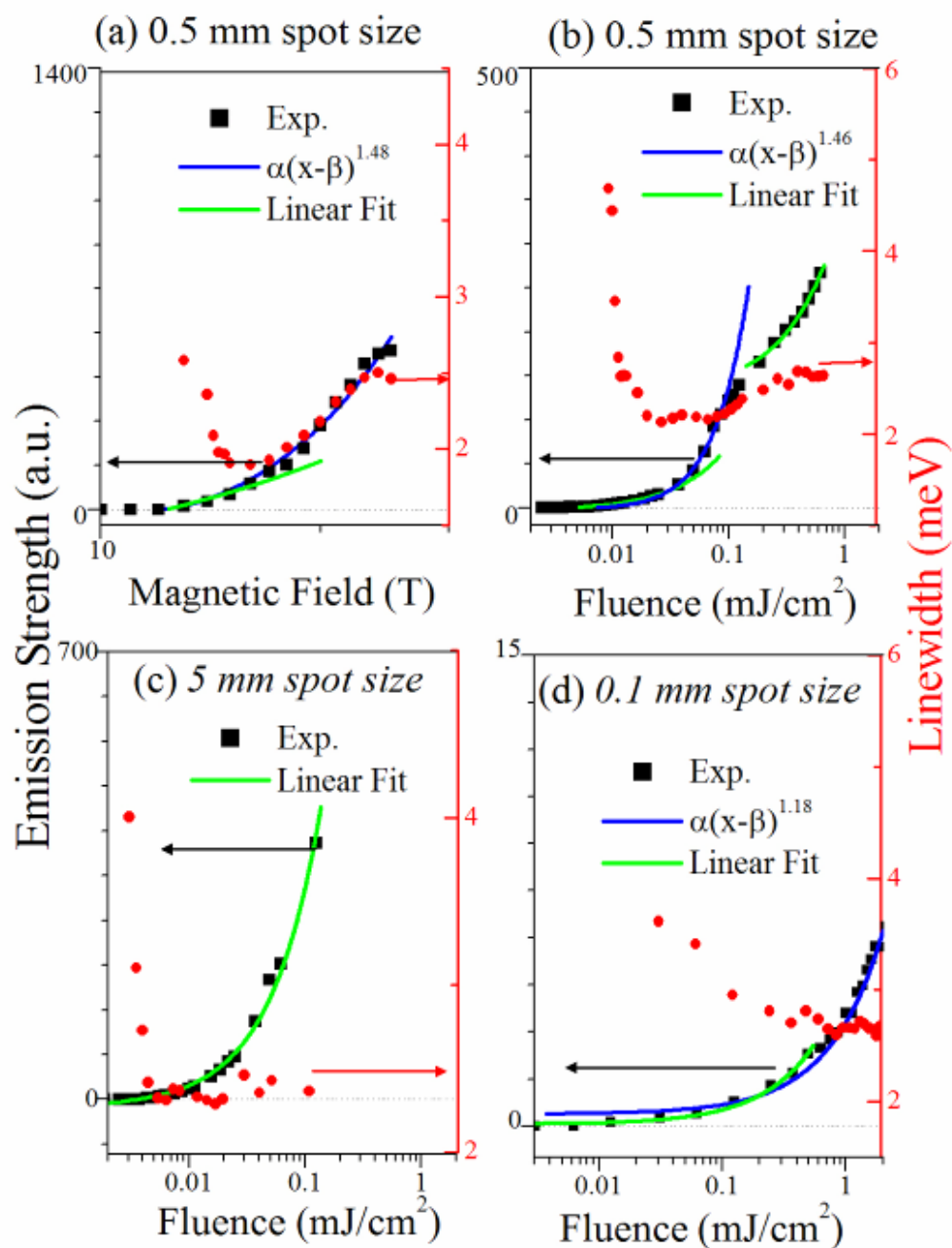
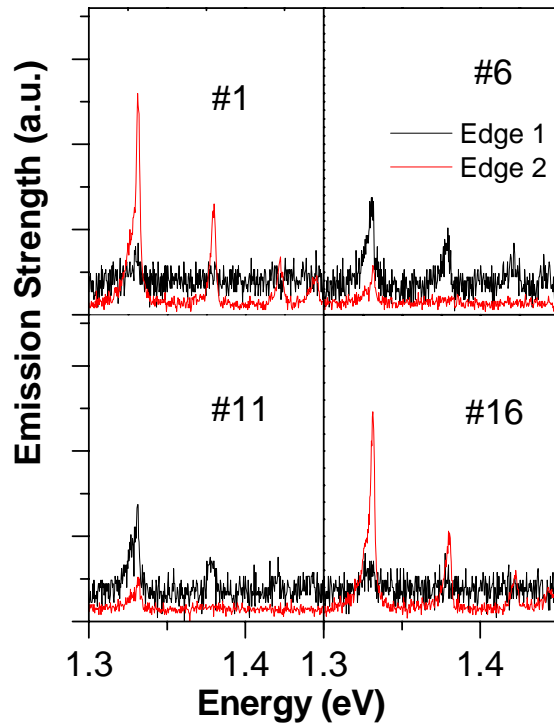
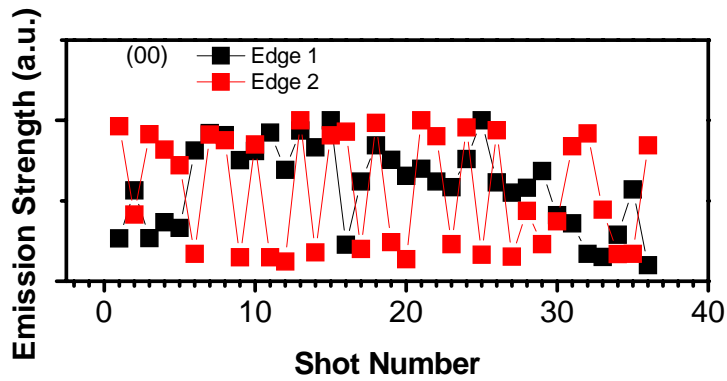


Figure 5-8. Excitation spot size effect on the in plane PL emission. Emission strength and linewidth of the narrow peak from the 0-0 LL versus (a) B and (b), (c), (d) F_{laser} for different pump spot size at 20 Tesla. Both B and F are on log scale.

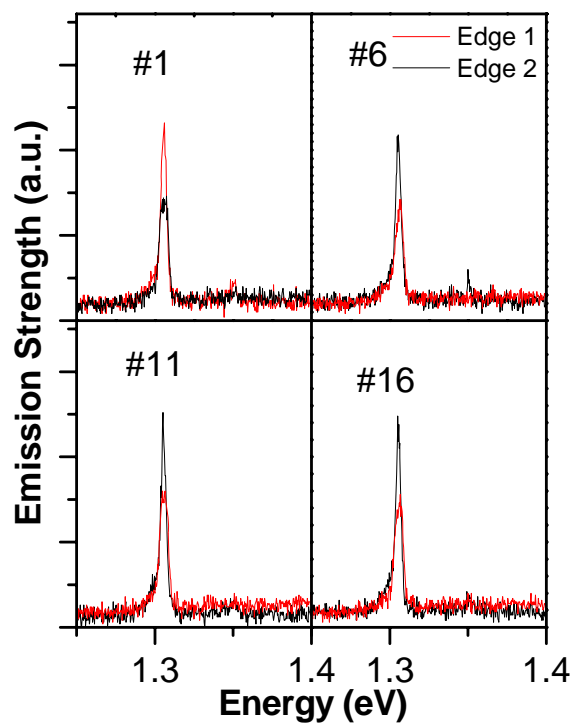


(a)

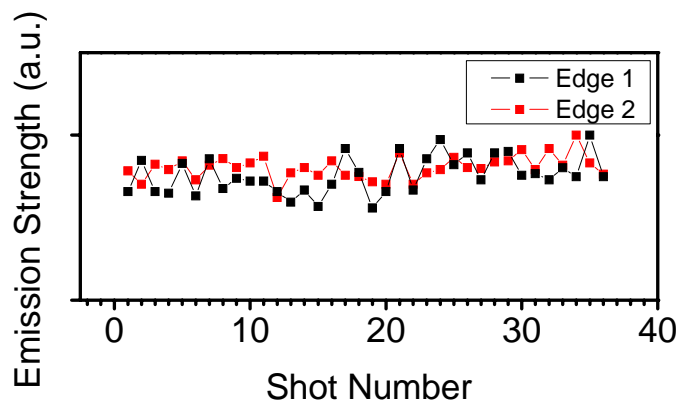


(b)

Figure 5-9. Single shot random directionality measurement of in plane PL emission excited with one CPA pulse in SF regime.(a) Four representative emission spectra from edge 1 (black) and edge 2 (red) fibers, excited from single laser pulse and measured simultaneously. (b) Normalized emission strength from the 0th LL versus shot number in the SF regime.



(a)



(b)

Figure 5-10. Single shot random directionality measurement of in plane PL emission excited with one CPA pulse in ASE regime.(a) Four representative emission spectra from edge 1 (black) and edge 2 (red) fibers, excited from single laser pulse and measured simultaneously (b) Normalized emission strength from the 0th LL versus shot number in the ASE regime.

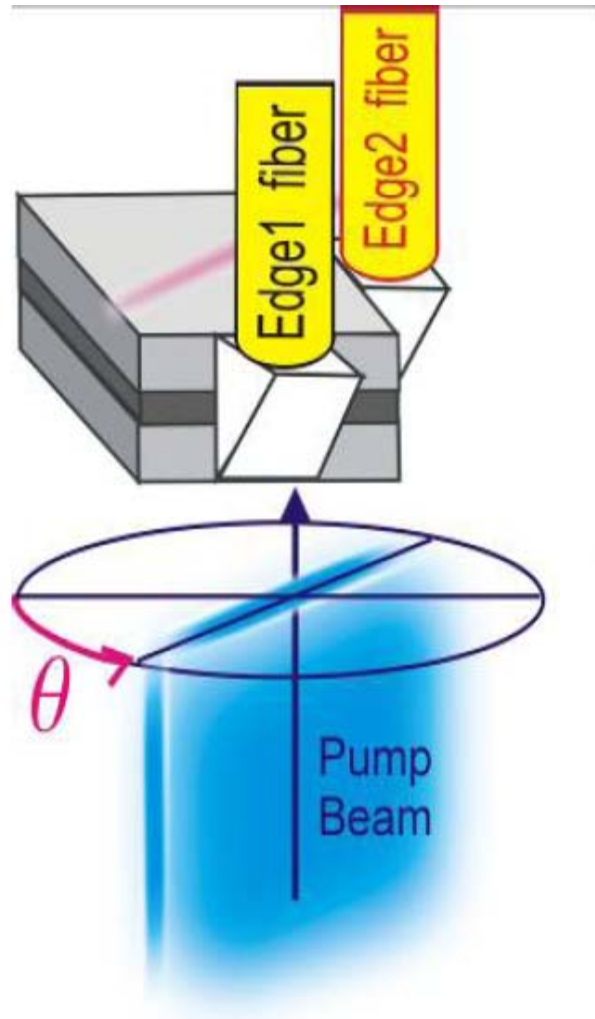


Figure 5-11. Configuration of control of emission directionality in $\text{In}_x\text{Ga}_{1-x}\text{As}$ multiple QW with cylindrical lens.

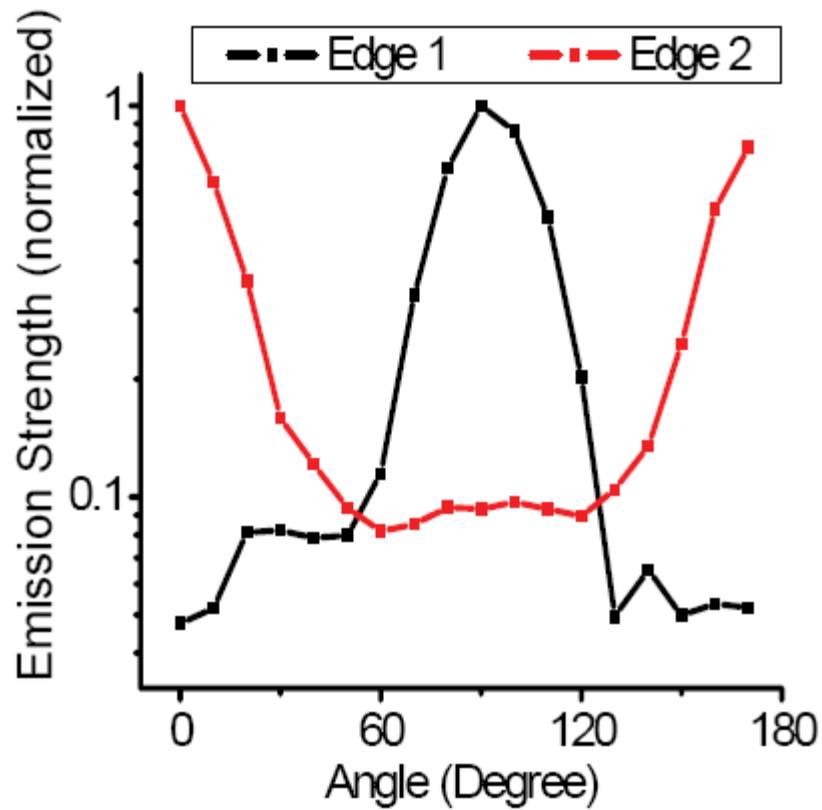


Figure 5-12. Control of coherence of in plane PL emission in $\text{In}_x\text{Ga}_{1-x}\text{As}$ QW. Edge emission strength of 0-0 LL transition from two orthogonally aligned fibers vs. the rotation angle θ . θ is the angular separation between the logner beam axis and the direction of the edge 2 fiber as shown in the Fig. 5-12..Emission strength of the 00 LL is plotted for edge 1(black) and edge 2 (red) as a function of angle.

CHAPTER 6
CARRIER DYNAMICS OF ZINC OXIDE SEMICONDUCTORS WITH TIME RESOLVED
PUMP-PROBE SPECTROSCOPY

6.1 Introduction

The II-VI group wide band gap semiconductor alloys such as ZnO, ZnMgO are recognized as important materials for potential applications in optoelectronic devices in the ultraviolet spectral range as well as for integrated optics substrates. Since the exciton binding energy of ZnO is 60mev [122-126], which is very high compared to GaN (~30mev) [127] or GaAs(~8mev)[128], the radiative electron hole recombination process in ZnO is even visible at room temperature[129]. Due to these unique properties, ZnO semiconductor materials are of interest in applications such as UV light emitting diodes (LEDs) and laser diode (LDs) [130]. Also, ZnO crystal is excellent substrate material for growing another important wide band gap semiconductor [131-132], GaN, since the lattice mismatch is relative small. For ZnO we have $a=b=3.249 \text{ \AA}$ and $c=5.206 \text{ \AA}$, while for GaN, we have $a=b=3.189 \text{ \AA}$ and $c=5.185 \text{ \AA}$.

The dynamics of carriers in ZnO semiconductor, which are critical for high speed electro optical device design, have recently been investigated by ultrafast time-resolved pump-probe spectroscopic method or time resolved photoluminescent spectroscopy [133-134] with above band gap excitation.

In our study, we have performed a comprehensive set of measurements on bulk ZnO, ZnO epilayers and nanorods. We measured the reflectivity and PL spectra of bulk ZnO, ZnO epilayer and nanorod from 4.2 K to 70K. In order to understand the excitonic states in ZnO materials, magneto reflection and PL spectra are also measured at 4.2K. Compared with previous studies [135], we identify and label the excitonic state on each spectrum. Via spectrally resolved degenerate pump-probe spectroscopy, we measured the time resolved differential reflectivity

(TRDR) of the A and B excitonic states in bulk ZnO, ZnO epilayer and nanorod. We find the life time of the A exciton (A-X) is approximately 130ps and while the B exciton (B-X) is ~ 45 ps at for bulk ZnO at 10 K. We also measured the temperature-dependent TRDR of A-X in bulk ZnO up to 70K, we find that the life time of A-X is still around 100ps, which indicates that relaxation processes do not change significantly at higher temperatures. This is associated with the properties of neutral donor bound X (D^0X). The life time of A-X (50ps) and B-X(20ps) in ZnO epilayer are very different from bulk ZnO, which is caused by different neutral donor bound X (D^0X) states in epilaer. The relaxation process of ZnO nanorod is fitted with stretch exponential decay curve, indicating different relaxation dynamics of Xs from bulk ZnO and ZnO epilayer. The coherent process in a very short time range (~ 2 ps) on the TRDR of A-X in bulk ZnO is analyzed with convolution of probe pulse with Gaussian function shape and carriers response with exponential decay curve.

6.2 Background of Crystal Structure and Band Structure of ZnO Semiconductors

ZnO crystallizes stably in a wurtzite structure with C_{6v} point group symmetry. This typical semiconductor lattice structure is shown in Fig. 6-1. In the x-y plane, the atoms in a unit cell form a hexagon, and the zinc atoms form hexagons and oxygen atoms form hexagons stack along the z-axis, called (0001) direction.

In the x-y plane, since ZnO possesses hexagonal symmetry, many physical and optical constants are isotropic, while along the z-direction they are different. However, we can use **a**, **b** and **c** unit vectors to label the unit cell of ZnO, where **c** is along z-axis and **a**, **b** are in x-y plane. In the study of optical properties of ZnO semiconductors, the polarization of absorption or emission light are very critical to probe since they are associated with the selection rules of transition and band structure symmetry. We define π linear polarization parallel to the c axis of

ZnO and σ linear polarization perpendicular to the c -axis. The geometry and definitions of polarization with respect to ZnO unit vectors are plotted in fig. 6-2.

As mentioned in chapter 3, a Hamiltonian with C_{6v} symmetry will couple the s states and form lowest conduction band and p_x , p_y and p_z states into three valence bands. The band structure of ZnO semiconductors is shown in Fig 6-3.

At the center of Brillouin zone, the conduction band is s -like, which has Γ_7 symmetry, while the p -like conduction band splits into three doubly degenerate bands due to spin-orbit (Δ_{so}) and crystal-field interaction (Δ_{cr}). In the valence bands, the top valence A band has Γ_9 symmetry while the B and C bands have Γ_7 symmetry. The excitonic states formed with electron in conduction band and holes in A, B and C valence bands are called A-X and B-X respectively. In Fig. 6-3, the total angular momentum ($J=L+S$, L is orbit momentum and S is spin momentum) of each Γ points are shown. The A, B and C valence band states at Γ point can be expressed as:

$$\begin{aligned}
 A: \left| \frac{3}{2}, \pm \frac{3}{2} \right\rangle &= \pm \frac{1}{\sqrt{2}} \left| X \pm iY, \pm \frac{1}{2} \right\rangle \\
 B: \left| \frac{3}{2}, \pm \frac{1}{2} \right\rangle &= \mp \frac{1}{\sqrt{6}} \left| X \pm iY, \mp \frac{1}{2} \right\rangle - \sqrt{\frac{2}{3}} \left| Z, \pm \frac{1}{2} \right\rangle \\
 C: \left| \frac{1}{2}, \pm \frac{1}{2} \right\rangle &= \mp \frac{1}{\sqrt{3}} \left| X \pm iY, \mp \frac{1}{2} \right\rangle + \sqrt{\frac{1}{3}} \left| Z, \pm \frac{1}{2} \right\rangle
 \end{aligned} \tag{6-1}$$

We can see that each valence band at Γ point are degenerate, each band will split in to doublet states (spin up“+” and spin down“-”) in magnetic field.

6.3 Valence Band Symmetry and Selection Rules of Excitonic Optical Transition in ZnO Semiconductors

The optical properties of bulk ZnO have been studied for over 40 years, and for the most part are well understood. However, there remains ambiguity and controversy in the assignment of symmetries of the A, B and C valence band states. In Thomas and Rodina’s assignment[136-137], the symmetry of A, B and C valence bands are Γ_7 , Γ_9 and Γ_7 since they considered that P_z

component is mixed into the A band, which results the reverse of the order of Γ_7 and Γ_9 in typical II-VI group semiconductors. In contrast, after carefully studying of the absorption, reflection and PL spectra as well as the Zeeman splitting of excitonic states of ZnO semiconductor [138], Reynolds have concluded that the order of top two valence bands in ZnO do not reverse. Therefore, in Reynolds's assignment of the order of valence bands in ZnO semiconductor, A, B and C bands have Γ_9 , Γ_7 and Γ_7 symmetry respectively. In this case, A band is pure P_x and P_y , and the only optical transition from A band to conduction band optical transition is expected to be σ polarization ($k // c$ and $E \perp c$, k is the direction of light propagation, c is c-axis). For the B band, the optical transition could be either σ polarization ($k // c$ and $E \perp c$) or π polarization ($k \perp c$ and $E // c$).

Based on group theory [18], the symmetry and selective rules of optical transition between conduction band and A, B and C valence bands in ZnO semiconductor are given as follows:

$$\text{A-X: } \Gamma_9 \otimes \Gamma_7 \rightarrow \Gamma_6 + \Gamma_5, \quad 6.2(\text{a})$$

$$\text{B-X: } \Gamma_7 \otimes \Gamma_7 \rightarrow \Gamma_5 + \Gamma_1 + \Gamma_2, \quad 6.3(\text{b})$$

$$\text{C-X: } \Gamma_7 \otimes \Gamma_7 \rightarrow \Gamma_5 + \Gamma_1 + \Gamma_2, \quad 6.2(\text{c})$$

where Γ_5 is allowed in σ polarization and Γ_1 is allowed in π polarization. The optical transition Γ_6 and Γ_2 are prohibited and Γ_1 is very weak [139].

In order to resolve the controversy of valence band ordering, a magnetic field was employed to observe Zeeman splitting of different optical transitions, since the Zeeman splitting for $\Gamma_9 \rightarrow \Gamma_7$ transition and $\Gamma_7 \rightarrow \Gamma_7$ transitions are very different-- Γ_6 is a doublet and splits into two in magnetic field while Γ_1 is a singlet and does not split in a magnetic field. Reynolds clarified the symmetry of the top valence band by studying the splitting behavior of PL emission

line from A-X in magnetic field at configuration [139]. In this thesis, we will consider the order of valence band according to the Reynolds assignment.

6.4 Impurity Bound Exciton Complex (I line) in ZnO and Zeeman Splitting

In bulk semiconductor materials there are many types of defects and localized states. Some of these states can bind excitons, resulting in a bound exciton complex (BEC).

Conceptualizations of an exciton bound to an ionized donor (D^+X), a neutral donor (D^0X) and a neutral acceptor (A^0X) are plotted in Fig.6-4. The binding energy E of these bound excitons usually increases according to [40]

$$E_{D^+X} < E_{D^0X} < E_{A^0X} . \quad 6-3$$

These BECs have many emission lines in the PL spectrum of bulk ZnO, termed 'I' lines. Also, when the free excitons or BEC optical transitions couple with longitudinal optical (LO) phonon, the phonon replica can be observed in the PL spectrum at energy position

$$E' = E - m\hbar\omega_{LO} , \quad 6-4$$

where E' is the positions of phonon replica, E is the energy of optical free exciton or BEC transition which is coupled with LO phonons, m is an integer, and $\hbar\omega_{LO}$ is energy of LO phonon. However, these phonon replica emission peaks are usually much weaker than the BEC emissions or free X emissions.

In a magnetic field, a quantum state with spin will split into two states, spin up and spin down. The energy splitting between the two states are called Zeeman splitting. However, in the case of free excitons or BEC, both electrons and holes can be involved in Zeeman splitting, which makes the interpretation of energy splitting of ZnO semiconductor in magnetic field more complicated than free electrons.

Zeeman splitting in ZnO can be express as

$$\Delta E = g_{exc} \mu B, \quad 6-5(a)$$

where μ is Bohr magnon, B is magnetic field strength and g_{exc} factor is Lande factor and can be written as:

$$g_{exc} = g_e + g_h. \quad 6-5 (b)$$

For an electron, the g factor is isotropic, while for a hole the g factor is anisotropic ($g_{//}$ and g_{\perp}), and typically g_{\perp} is nearly zero [136]. In above expression, $//$ means the c -axis of ZnO is parallel to the magnetic field B and \perp means the c -axis is perpendicular to the magnetic field.

In the case of BEC, the Zeeman splitting is qualitatively different than free excitation Zeeman splitting since the splitting of ground states of D^0 and A^0 has to be considered in addition to the splitting of electron and hole in an exciton. Rodina and Reynolds [139] have studied the splitting of BEC in ZnO and the results are shown in Fig. 6-5.

As shown in figure 6-5, the excited state of D^0X consists of a donor defect, two electrons and one hole, with the two electrons spins antiparallel. The Zeeman splitting of the excited state is determined by the anisotropic hole effective g factor, while the Zeeman splitting ground state D^0 is given by the effective g factor of electron g_e . Therefore the splitting of optical transition of D^0X in the Faraday geometry ($B//c$ and $k//c$) (see Fig.6-6) is given by

$$\Delta E = (g_e - g_{h//}) \mu B, \quad 6-6(a)$$

and the splitting in Voigt geometry ($B \perp c$ and $k//c$) (see Fig.6-6(b))is

$$\Delta E = g_e \mu B. \quad 6-6(b)$$

Also the Zeeman splitting should be linear in magnetic field. In the case of the acceptor bound exciton A^0X , the Zeeman splitting has similar form.

6.5 Samples and Experimental Setup for Reflection and PL Measurement

The ZnO samples we used for magneto optical spectroscopic studies are bulk ZnO (grown by MTI Crystal Co.), ZnO epilayers (grown by David Norton's group at University of Florida), and ZnO nanorod grown in GIST in South Korea). The size of bulk ZnO is 5x5x0.5mm and the orientations of the crystals are *c*-plane (*c*-axis perpendicular to the plane) or *a*-plane (*a*-axis perpendicular to the plane and *c*-axis in the plane) configurations. The bulk ZnO crystal was grown with hydrothermal method. The 400nm thick ZnO epilayer samples were grown on a *c*-plane sapphire substrate via the MBE method and the self-assembly ZnO nanorod sample with rod diameter 8nm is grown with laser deposition. All the ZnO samples were nominally undoped.

We measured the reflection spectrum of all the ZnO samples with polarized light to identify the excitonic states. We used a Deuterium lamp with the output polarized using a Glan-Laser polarizer. In the reflection spectrum measurements, ZnO samples were put in a cold finger style optical cryostat, in which the samples can be cooled down to 4.2K with liquid helium.

In magneto-optical spectrum measurements, we used the cw magneto-optical facility at NHMFL shown in Fig.2-2, 2-3. The ZnO was mounted inside the helium tail of a Janis cryostat and cooled down with helium exchange gas. The light was delivered to ZnO sample through multimode optical fiber, and the reflection and PL emission were collected with another multimode optical fiber. Here, we used a UV Xenon lamp for measuring the reflection spectrum and a He-Cd laser (325nm wavelength) for exciting the sample to measure the PL spectrum. Both the reflection light and PL emission were delivered to a 0.75m McPherson spectrometer and the spectrum was recorded with a charge-coupled device (CCD). In the temperature dependent measurement, the sample temperature was measured and controlled by a Cernox sensor, a Cryocon temperature controller and a heater with 50 W maximum power output.

6.6 Results and Discussion

In figure 6-7, the reflection spectrum of a-plane bulk ZnO at 4.2K obtained using σ and π polarized light. The excitonic optical transitions obey the transition rules listed in equation. 6-2, where A-X (Γ_9), B-X (Γ_7) and C-X (Γ_7) are activated in σ polarized light and C-X (Γ_7) is activated only in π polarized light. However we cannot specify the exact energy positions of free excitons peaks since the complexity in reflection spectrum (see Chapter 2).

In figure 6-8(a), the magneto-PL spectrum of *c*-plane bulk ZnO is plotted for the Faraday configuration ($B//c, k//c, E\perp c$). We can see that the PL emission feature is a sharp peak sitting on the top a broader and weaker peak, which caused by inhomogeneous broadening. There is no significant magnetic splitting observed, although the sharp PL peak becomes broader (possibly due the onset of splitting) and the PL intensity becomes lower with the increasing of magnetic field strength. Figure 6-8(b) shows the PL spectrum of the same sample at Voigt configuration ($B\perp c, k//c, E\perp c$). It is clearly evident that the sharp PL peak split linearly into two peaks with the increasing magnetic field. The energy position vs. magnetic field of the peaks is plotted in figure 6-8(c). This is Zeeman splitting and will be discuss further in the following section, however, since we use multi-mode fiber to delivered light, no polarization information can be obtained from the two PL peaks and the spin states can be resolved.

In order to understand the PL emission spectrum, we plot the reflection and PL emission at zero field in figure 6-9(a). We can assign the PL emission peak at 3377 meV to the recombination of free A-X, indicated by an arrow in the figure. The other PL peaks at lower energies are assigned as emission from impurity bound A-X, the strongest bound exciton PL peak is at 3360 meV and has been reported to be neutral donor bound exciton (D^0X) [140].

In figure 6-9(b), the reflection and PL emission spectrum of the c-plane bulk ZnO in both Faraday and Voigt configurations at 30 Tesla are plotted. From this data, we can conclude that the A-X and its bound state do not split in Faraday geometry while they split into two peaks in Voigt geometry. At 30 T, the splitting of PL peaks from A-X donor bound state is ~ 3.4 meV.

The magnetic splitting of A-X and D^0X can be interpreted with the splitting process shown in figure 6-5 and equation 6-6 as following. In the Faraday geometry, according to Eq. 6-6, the magnetic Zeeman splitting of A-X and D^0X is determined by Lande factor g_{exc} , which is $g_e - g_h = 0.7$ [16], therefore the Zeeman splitting at 30 Tesla is around 1.2 meV, which is smaller than the resolution of spectrometer and thus can not be observed with our spectrometer.

However, in Voigt geometry the Lande factor $g_{exc} = g_e$, since $g_h = 0$, therefore the Zeeman splitting at 30 T is ~ 3.38 meV, which is in agreement of our observation 3.08 meV. In Fig. 6-8(d), we plot the experimental and calculated results of ΔE vs. B , the results are in good agreement if we take into consideration that the resolution of spectrometer is around 1meV. This agreement strongly proves that the dominant PL emission peak comes from neutral bound exciton.

In the case of the ZnO epilayer sample, we plot the reflection and PL spectrum at zero fields in figure 6-10(a), we can clearly resolve the A-X and B-X in the reflection curve. In the PL spectrum we observe a strong emission at 3355 meV, which is also from bound exciton transition, however the PL peak is asymmetric and has a long tail at the low energy side, and in addition the PL linewidth is much broader (5~6 meV) than the bulk ZnO (2 meV). All of these observations imply that the optical quality of this ZnO epilayer is not as good as bulk ZnO, with more defect states present which cause more inhomogeneous broadening and carrier trapping below the bandgap, and result in the PL linewidth broadening and an asymmetric line shape. At

3285 meV, we observe a PL emission peak due to LO phonon coupled with bound exciton transition, since the LO phonon energy is 70 meV in ZnO. Due to the fact that the PL emission linewidth is larger than the predicted Zeeman splitting, we cannot resolve and observe the PL peak splitting in neither Faraday geometry nor Voigt geometry in this ZnO epilayer sample as shown in Fig.6-10(b).

6.7 Time Resolved Studies of Carrier Dynamics in Bulk ZnO, ZnO Epilayers, and ZnO Nanorod

As introduced in chapter 2, time resolved spectroscopy is a very important tool for understanding the dynamics of carriers and excitons in semiconductors, critical for applications in electro- optical device.

From Chapter 2, the changes to the dielectric fuction ε are given by [141]

$$\Delta\varepsilon(\omega_L, t) = -\sum_i \frac{\Delta N_i(t) e^2}{\varepsilon_0 m_i \omega_L^2}. \quad 6-7$$

Where ω_L is the laser frequency, $\Delta N_i(t)$ is the carrier density in the *ith* energy band and m_i is the carrier mass of the *ith* band. Since ZnO is a wide bandgap semiconductor, the high-frequency limit ($\omega_L t \gg 1$) is satisfied, therefore the differential reflectivity is proportional to the change in carrier density in each energy band divided by the mass of the band, summed overall bands, which is shown in equation 6-8,

$$\frac{\Delta R}{R} \sim \left(\sum_i \frac{\Delta N_i}{m_i} \right). \quad 6-8$$

This shows clearly that the differential reflectivity measurements effectively probe the changes in carrier density in different ZnO energy bands.

In the recombination of an electron and hole pair, both radiative and nonradiative recombination processes are usually involved, and the rate equation can be expressed as follow

$$\frac{1}{N} \frac{dN}{dt} = \frac{A_1}{\tau_{radiative}} + \frac{A_2}{\tau_{nonradiative}}, \quad 6-9$$

where N is the carrier density, $\tau_{radiative}$ and $\tau_{nonradiative}$ are radiative and nonradiative relaxation times, A_1 A_2 is corresponding efficiency. In radiative recombination, photons are emitted as the carriers recombine to conserve energy, while in nonradiative processes, electrons and holes recombine through emission of acoustic phonons.

As we have seen that bulk and epilayer ZnO exhibit different reflectivity and photo-excited emission characteristics due to the presence of defect states, we now turn to investigations of how those differences impact dynamical carrier processes. We measured the time resolved differential reflectivity (TRDR) spectrum of ZnO semiconductors, including bulk with different orientation, c -plane epilayer and nanorod samples with 8 nm rod diameters. Since the absorption coefficient of ZnO is very high, it is very difficult to get good transmission signal from thick samples, we use reflection geometry to get TRDR signal.

The experimental setup for measuring the TRDR of ZnO semiconductors is shown in figure 6-11. We used ultrafast laser pulses 150fs in duration at a wavelength of 730 nm from a Coherent Mira 900-F laser system with 76 MHz repetition rate. The laser beam was focused onto a nonlinear β -barium-borite (BBO) crystal to frequency double the pulses into the near UV around 365nm via second harmonic generation (SHG). The UV laser pulses were then split into pump and probe beams using a sapphire plate. Both the pump and probe beam propagated through waveplates and Glan-Laser polarizers to make them parallel or perpendicularly polarized before they were focused down to $50\mu\text{m}$ on the ZnO samples, mounted in an optical cryostat. Liquid helium flows into the cryostat during the measurements, by which we can cool down the ZnO samples to down to 4.2K and reduce the thermal broadening effect and phonon effects. The

pump beam was time delayed with respect to probe beam using a Newport stage controlled by computer. To obtain the best signal-to-noise ratio, the pump and probe beams were chopped with a differential frequency $f_1 = 2\text{KHz}$ and $f_2 = 1.57\text{KHz}$, and the probe reflectivity signal was detected using photodiode via a lock-in amplifier demodulating the signal at $f_1 - f_2$.

6.8 Experimental Results and Discussion

6.8.1 Relaxation Dynamics of A-X and B-X in Bulk ZnO

In figure 6-12, the TRDR at 10K are plotted for A-X and B-X in *a*-plane bulk ZnO semiconductor, both the probe beam and pump beam set to σ polarization (perpendicular to *c*-axes), in which A-X and B-X are optically activate. The DR curve decays exponentially. We fit the two curves exponentially with equation 6-9 and obtain the following results,

$$\tau_{AX} = 130 \pm 10 \text{ ps} \text{ and } \tau_{BX} = 45 \pm 1 \text{ ps} .$$

The sharp peaks in figure 6-12(a) and (b) at $t=0$ ps most likely arises from a coherent artifact due to the collinearity of the pump and probe polarization. More discussion about this fast relaxation process will be given in the following.

However, the relaxation time τ is much smaller than previous report for free A and B excitons [142], reported 1ns. This strongly suggests that in these samples, the A and B excitons are mainly bound to an impurity state, which makes the D^0X dominate the relaxation process instead of free exciton recombination. This agrees well with the PL data (figure 6-9) in which the D^0X is three orders stronger than free A-X. In this case, A_1 is much smaller than A_2 , which indicates that the radiative recombination can be neglected compared to nonradiative processes in the exciton relaxation process.

In figure 6-14, we plot the TRDR spectrum of AX in *c*-plane bulk ZnO at different temperatures up to 70K, where the laser wavelength is tuned to resonantly probe the A-X as the

temperature increases. The artifact observed in figure 6-12 does not show up here because the pump and probe laser beam are orthogonally polarized. We also observe mono-exponential decay of DR in this figure. The fitting results of the relaxation time are $\tau_{AX} = 130 \pm 10 ps$, which do not change significantly with temperature up to 70K and imply that the A-X relaxation process is dominated by a bound to impurity state instead of radiative recombination up to 70K, since the binding energy between neutral donor and an exciton is around $\sim 10 meV$ [18], which makes it difficult to break them at low temperature.

In semiconductor, immediately after the carrier are excited with coherent laser light (pump beam), the carriers preserve the coherence generated with laser beam in a very short time ($\sim ps$) [143], if the probe beam arrives during this carrier coherent status, strong interaction will be expected between the coherent carriers and coherent light, which result in the sharp feature in Fig. 12. In this case, the actual signal that we acquired is the convolution of probe pulse and carrier decay, which are presumed to be Gaussian function and exponential decay function respectively. The convolution result is given as:

$$S(t) = \frac{A}{2} \exp\left(\frac{\sigma^2}{2\tau^2} - \frac{t}{\tau}\right) \left[1 - \operatorname{erf}\left(\frac{\sigma}{\sqrt{2}\tau} - \frac{t}{\sqrt{2}\sigma}\right)\right]. \quad 6-10$$

Where τ is the exponential decay time and $\sqrt{2} \sigma$ is the FWHM of the Gaussian function.

Fig. 6-13 shows the fitting of the fast relaxation cure with the convolution function 6-10, we can see that the pulse width is around 0.5ps and the coherence exponential decay time is around 1.4ps.

6.8.2 Relaxation Dynamics of A-X and B-X in ZnO Epilayer and Nanorod

In figure 6.-15, TRDR spectra of AX and BX in ZnO epilayer at 4.2K are plotted. It is clearly resolved that the carriers populate on BX decay mono-exponentially. The fitting result of

BX relaxation time is $\tau_{BX} = 25 \pm 1 ps$. However, the A-X shows a stretched exponential decay process, which is described by

$$I = A \exp\left(-\frac{t}{\tau}\right)^n + I_0, \quad 6-11$$

where τ is the decay time and $n < 1$ is stretched factor.

With this function, the fitting results of A-X relaxation in ZnO epilayer are $n=0.9$ and $\tau=50ps$. These exciton relaxation times are much smaller than the bulk ZnO, which indicate that the density of defect states in the ZnO epilayer sample are more than that in the bulk ZnO sample. Also, by comparing the carrier relaxation time, we might expect that the defect state dominates in epilayer sampler should be different from that in bulk sample since the relaxation are quite different. These can be convinced in the PL spectrum in figure 6-10, in which we can not see the free X emission, most Xs are bound to defect states and emit photons at 3355 meV instead of 3360 meV in bulk ZnO samples.

In figure 6-16, the TRDR of ZnO bulk nanorod is shown. The excitation and probe light energy is 3416mev, which is supposed to be above the ZnO bandgap. We can see that the TRDR cure of ZnO bulk nanorod sample decay stretched exponentially. This curve is fitted with 6-11. The fitting results are $\tau=17ps$ and $n=0.65$.

The stretched exponential relaxation is summation of distribution of independent exponential decay relaxations and is indication that there is an inhomogeneous distribution of recombination times. It is reported in many semiconductors material especially in nanostructures [144-145]. Three mechanisms [146-147] are proposed to interpret the stretched exponential decay.

The distribution in lifetime is a result of varying carrier localization such that carriers can escape from one area of sample to other area and recombine nonradiatively.

The migration of excitons between distorted nanostructures is possible, which result in the capture and delayed released of excitons.

Distribution of the lifetime in PL at a single wavelength could be explained by the distribution of the nanocrystal shapes in a given area.

From the above explanations, we found that the stretched exponential is mainly caused by the either trapped of carriers, carrier hopping between nanostructures or different size of nanostructures.

We can see that the stretched exponential decay of exciton in ZnO epilayer and nanorods indicate that the sample might have many defects states, which traps the carriers, the nanorod sample might have different size effect and also the carriers in nanorod might migrate between rods.

Table 6-1. Some parameters of ZnO bulk semiconductors

Point group	$6mm(C_{6v})$ (Wurtzite)
Lattice constants at room temperature	$a=3.250, c=5.205 \text{ nm}^1$
Electron mass	$0.28 m_e^1$
Hole mass	$1.8 m_e^1$
Bandgap energy at room temperature	3.37 eV^1
Exciton binding energy	60 meV^1
Melting point	2250 K^1
LO phonon	70 meV^1

¹ Reference[10]

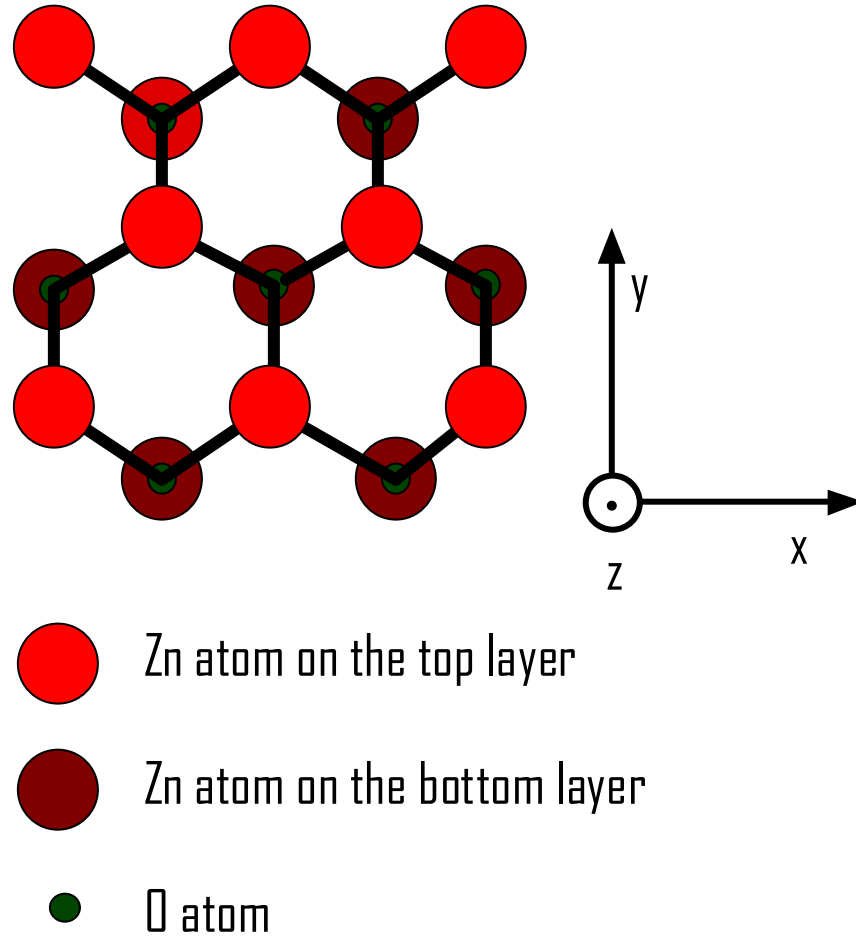


Figure 6-1. Top view of the lattice structure of a wurtzite ZnO crystal. In the x-y plane, ZnO has hexagonal symmetry along the z-axis. In z-axis direction, Zn atoms are on the top and bottom layers, O atoms layer is between the two Zn atom layers. Also, another O atoms layer (not shown) is on the top of top layer of Zn atoms. In the (0001) direction, hexagonal symmetry is along the z-axis.

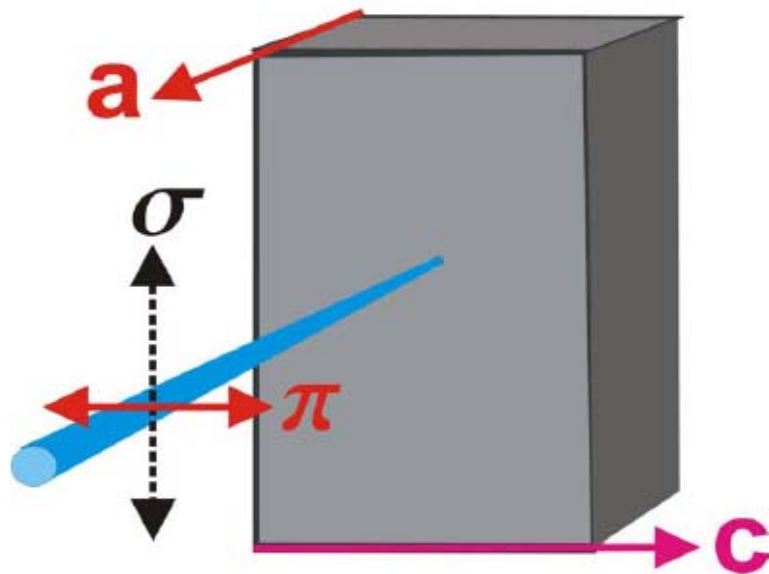


Figure 6-2. The orientation of light polarization with respect to the ZnO unit cell. The σ polarization is defined as perpendicular to c-axis and π polarization is defined as parallel to c-axis.

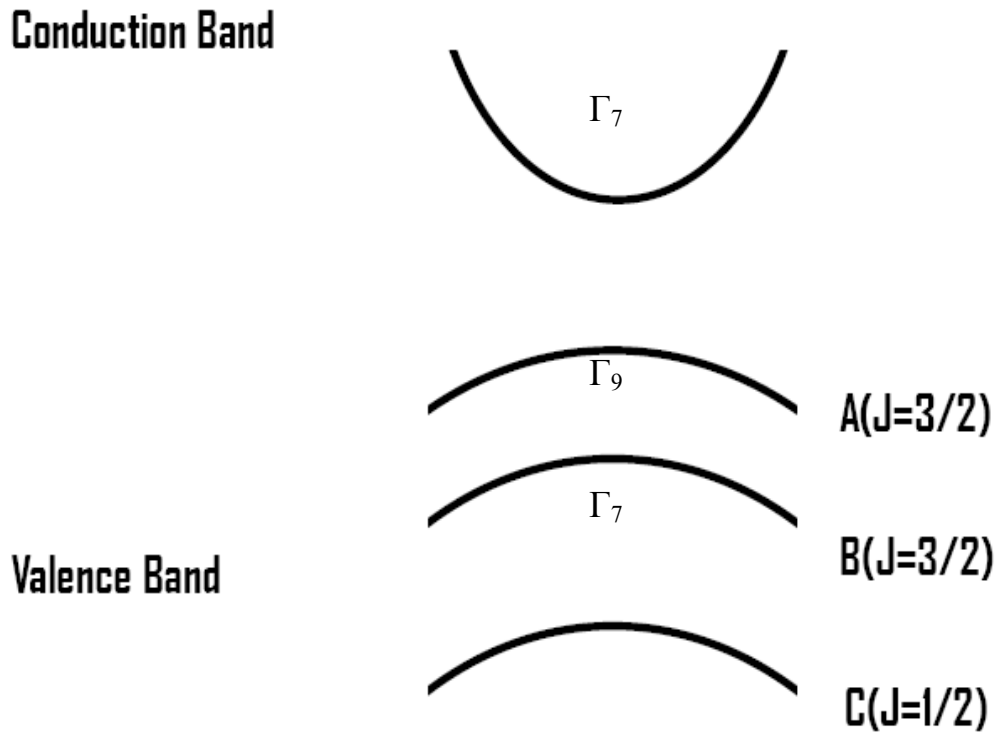


Figure 6-3. Band structures and symmetry of each band of a ZnO semiconductor. At the center of the Brillouin zone, the conduction band has Γ_7 symmetry, and for the valence bands listed as A, B and C from top to lowest, the symmetries are, Γ_9 and Γ_7 respectively.

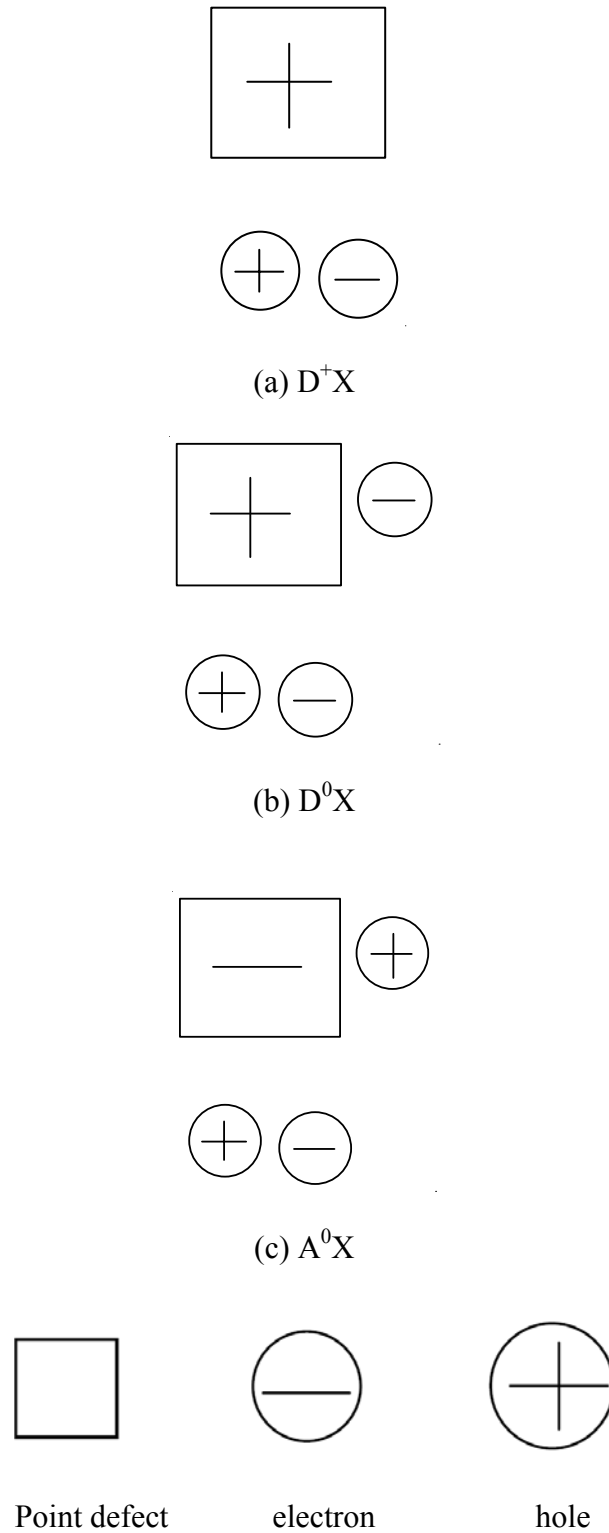


Figure 6-4. Schematic of types of impurity bound exciton complexes. (a) an ionized bound exciton (b) a neutral donor bound exciton (c) a neutral acceptor bound exciton

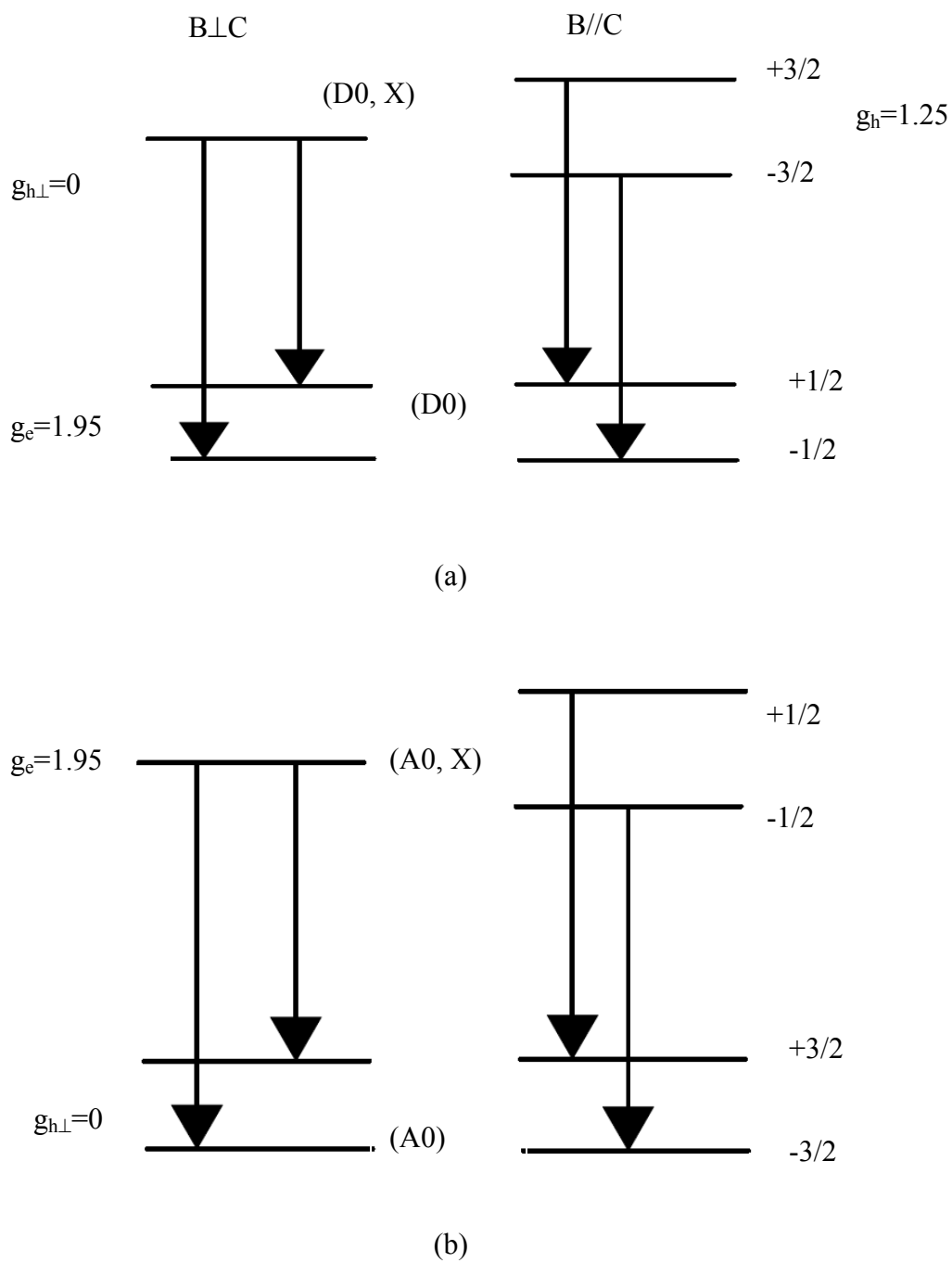


Figure 6-5. Energy diagram of Zeeman splitting of neutral bound excitons in ZnO. (a) donor-bound exciton, (b) acceptor-bound exciton

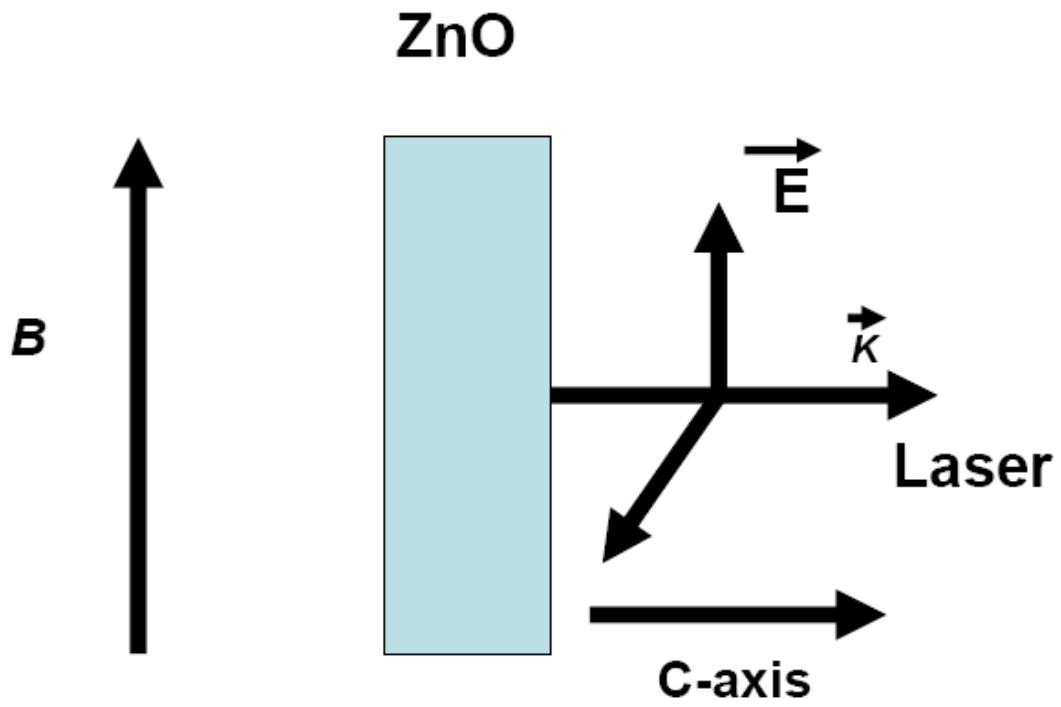


Fig.6-6. Voigt configuration of c-plane ZnO in magnetic field. Faraday configuration is shown in Chapter 4.

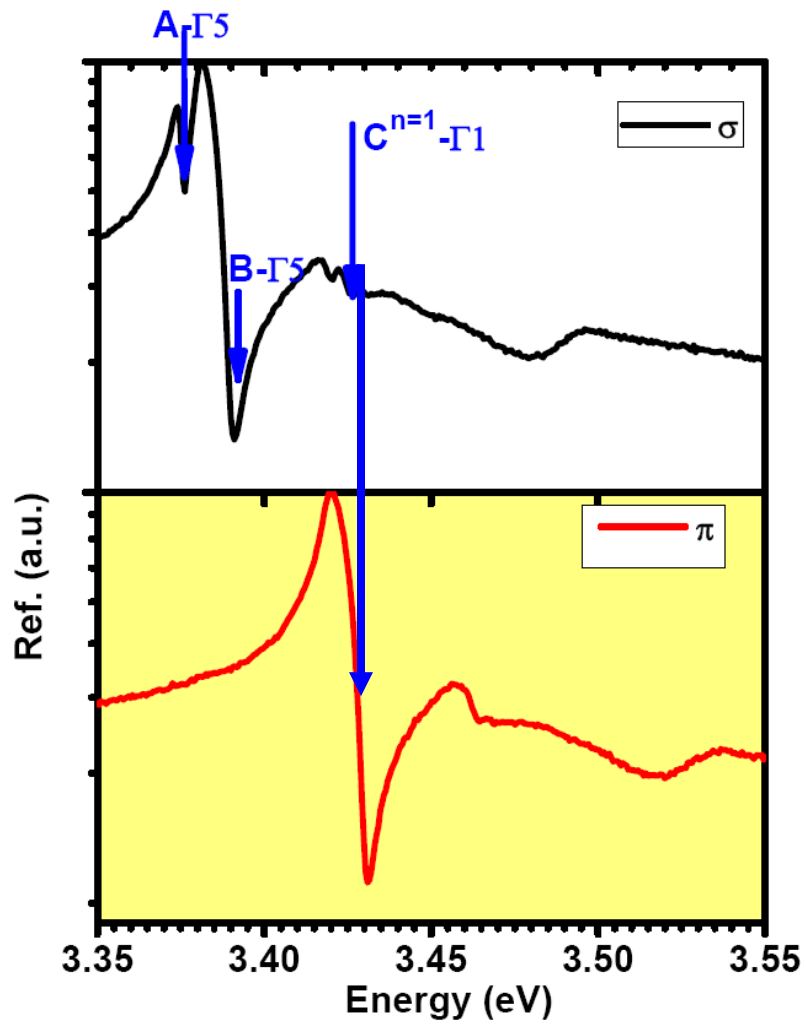


Figure 6-7. Reflection spectrum of a-plane bulk ZnO semiconductor for different linear optical polarization at 4.2K. The upper curve is σ polarization and the lower curve is π polarization. The arrows point out the exciton energy position and the related symmetry.

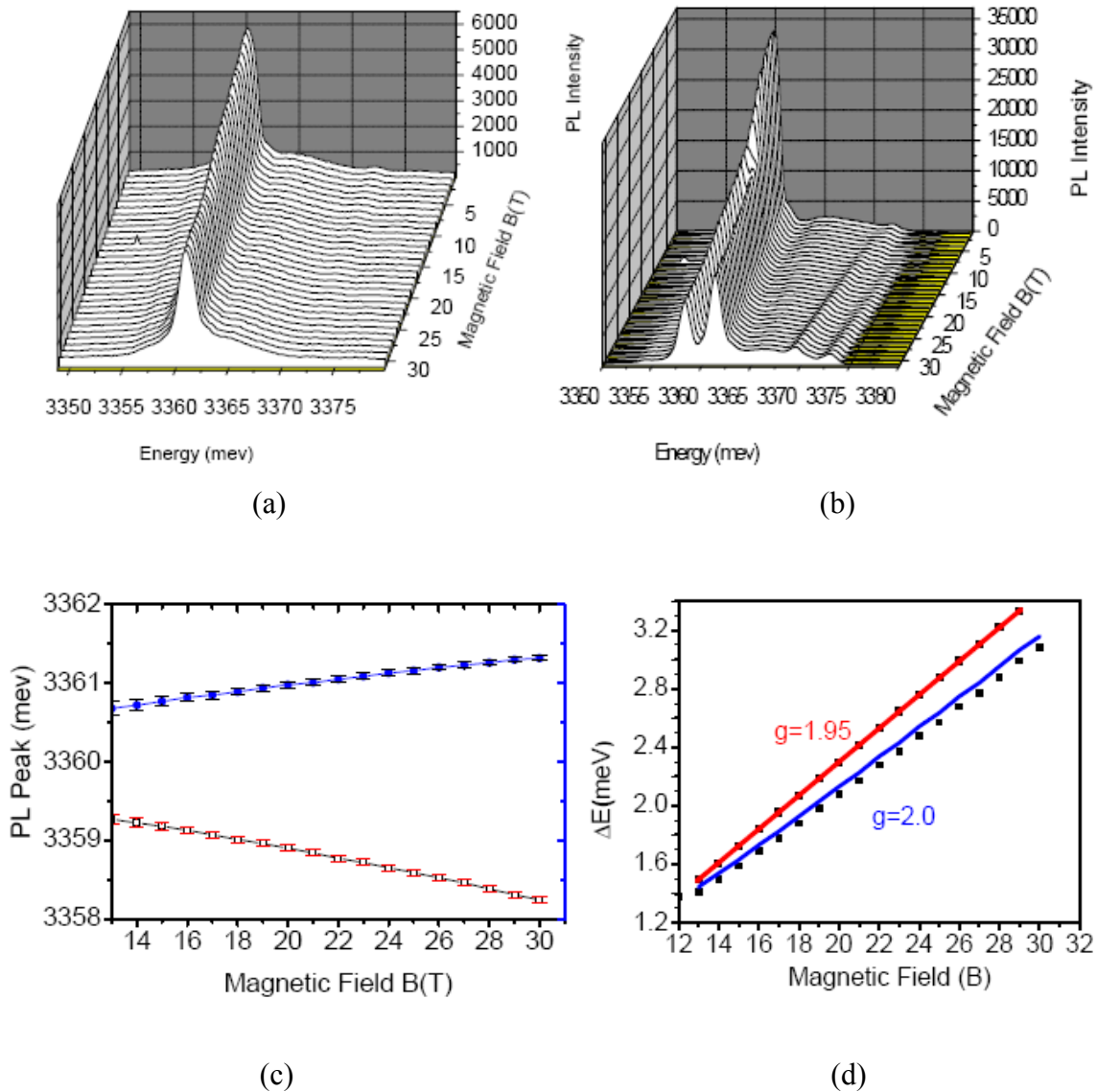
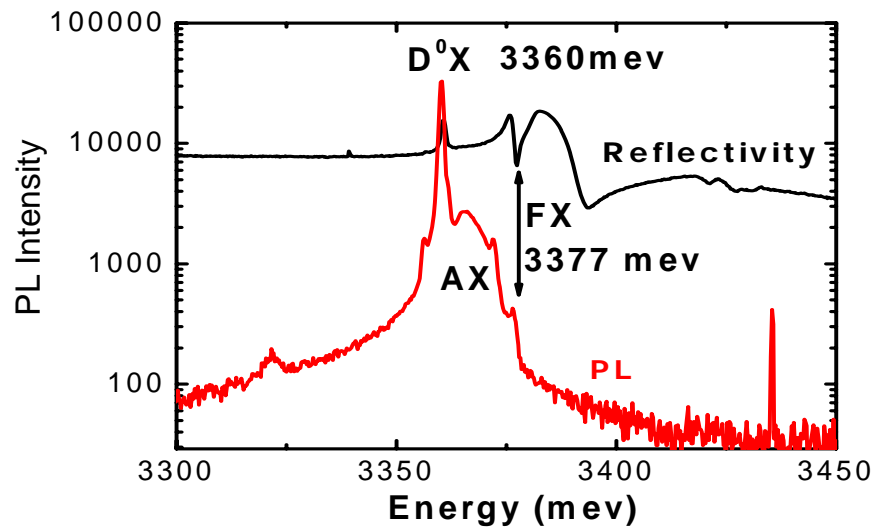
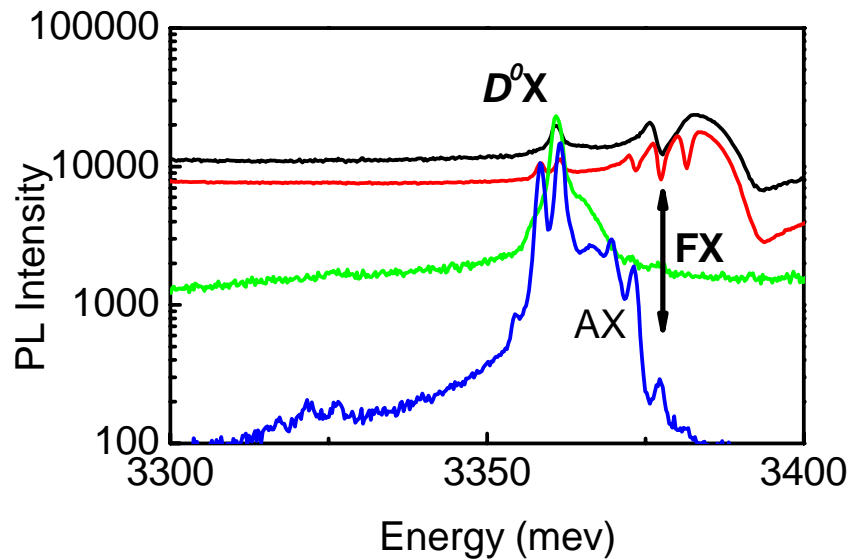


Figure 6-8. The magneto-PL spectrum of *a* and *c*-plane bulk ZnO sample and Zeeman splitting at 4.2K PL spectrum in (a) Faraday and (b) Voigt configurations, (c) The Zeeman energy splitting in Voigt geometry as function of magnetic field, (d) Zeeman splitting ΔE vs. magnetic field, black dot is experimental result and red and blue line are fitting with $g=1.95$ and 2.0 respectively.

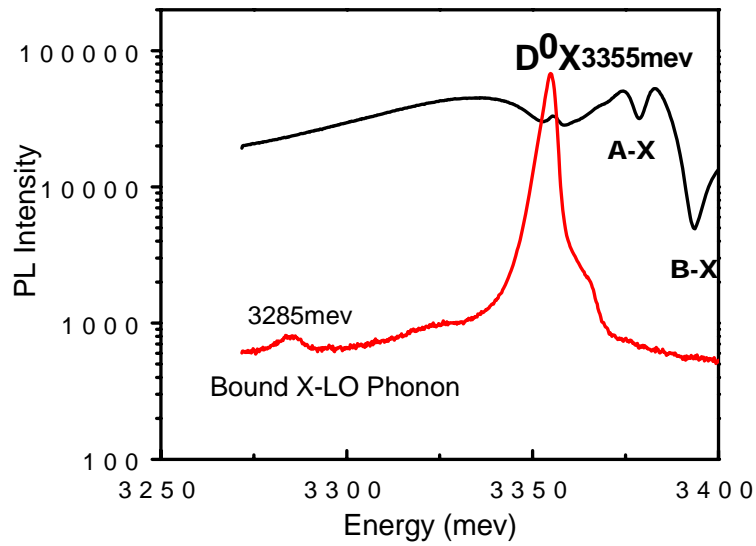


(a)

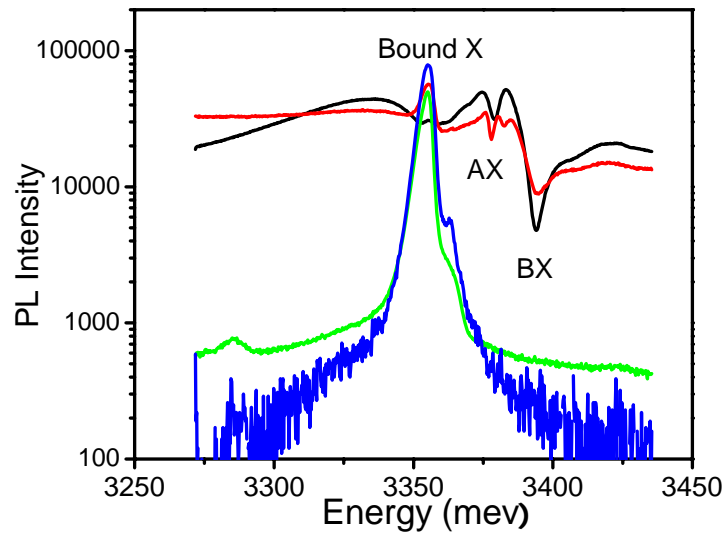


(b)

Figure 6-9. Comparison of reflection and PL spectrum of c-plane bulk ZnO. (a) reflection (black curve) and PL (red curve) at zero magnetic field, (b) reflection in the Faraday geometry (black curve), Voigt geometry (red curve), and PL in the Faraday (green curve) and Voigt (blue curve) configurations at 30 T.



(a)



(b)

Figure 6-10. Comparison of reflection and PL spectrum of c-plane epilayer ZnO at 4.2 K. (a) reflection (black curve) and PL (red curve) at zero magnetic field, (b) reflection in the Faraday geometry (black curve), Voigt geometry (red curve), and PL in the Faraday (green curve) and Voigt (blue curve) configurations at 30 T.

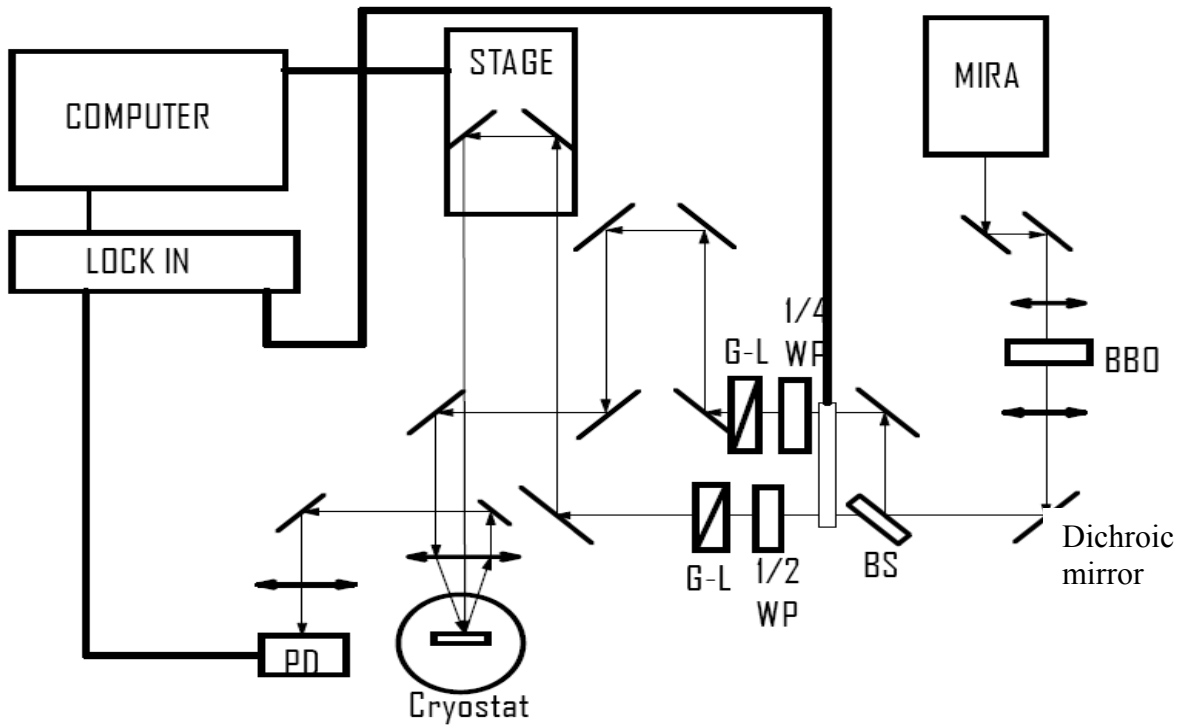
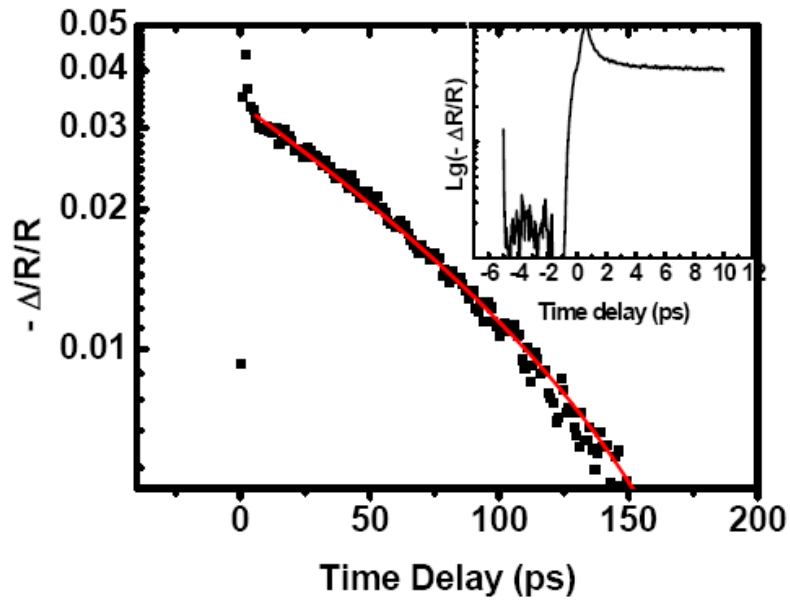
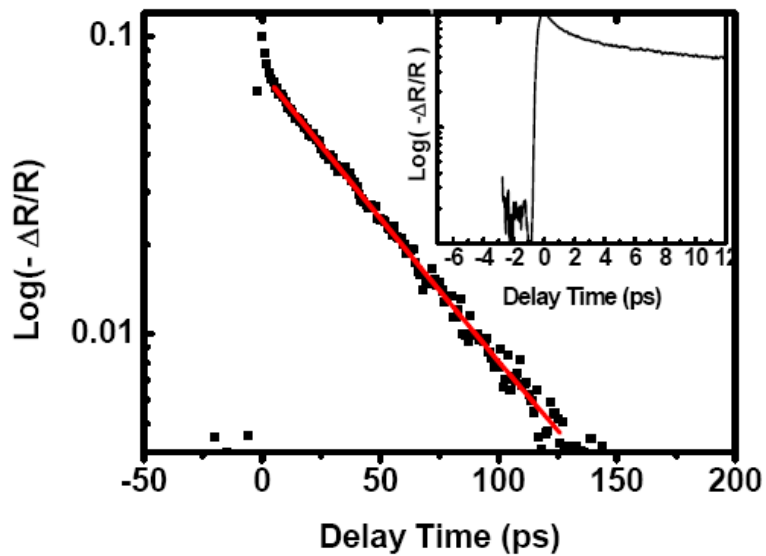


Figure 6-11. Pump-probe experimental setup for measuring TRDR of ZnO semiconductors. BS is beam splitter, WP is waveplate, G-L is Glan-Laser polarizer, PD is photodiode



(a)



(b)

Figure 6-12. TRDR plots of a-plane bulk ZnO semiconductor at 4.2K (black dot) and exponential decay fitting line.(a) AX probe at 3375 meV, decay time 130 ± 10 ps, (b) BX, probe at 3387 meV decay time 45 ± 1 ps. Both of the inserts are TRDR spectra show fast decay in short time (~ 1 ps) range. The cure in (a) does not fit well with exponential decay due to alignment problems of optics.

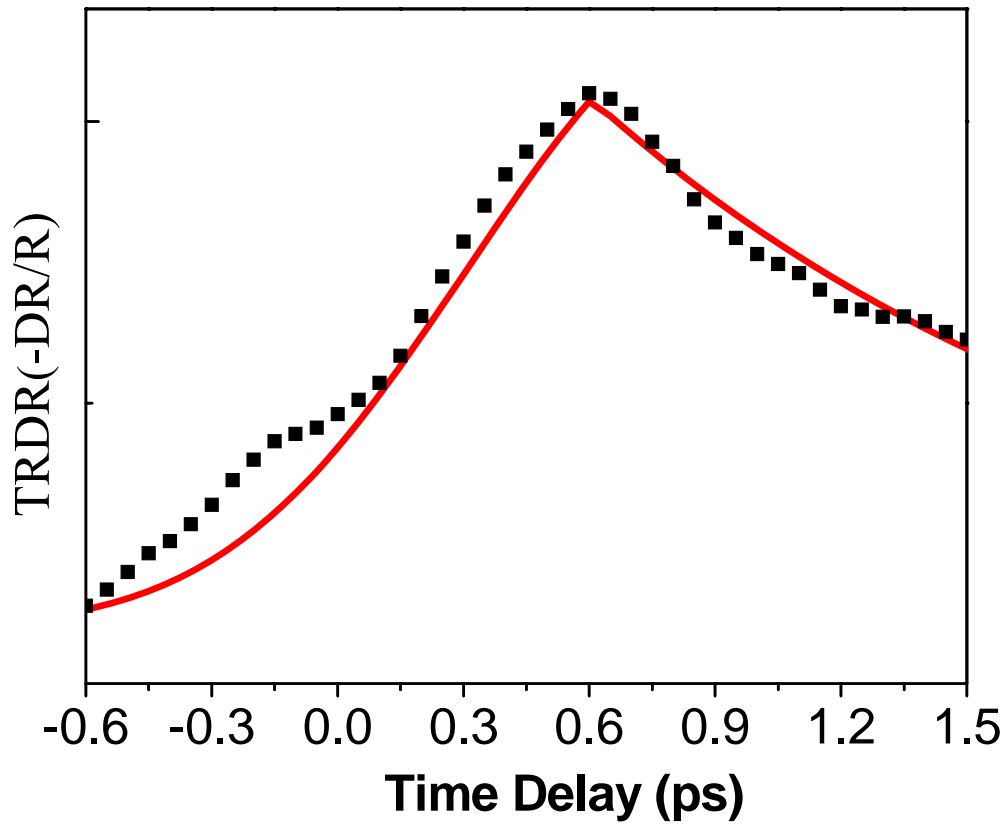


Figure 6-13. Fast decay in TRDR of A-X in a-plane bulk ZnO and the fitting with convolution of Gaussian function probe pulse and exponential decay response function. Fitting parameters are pulsewidth=0.5ps and $\tau_{\text{response}}=1.4\text{ps}$.

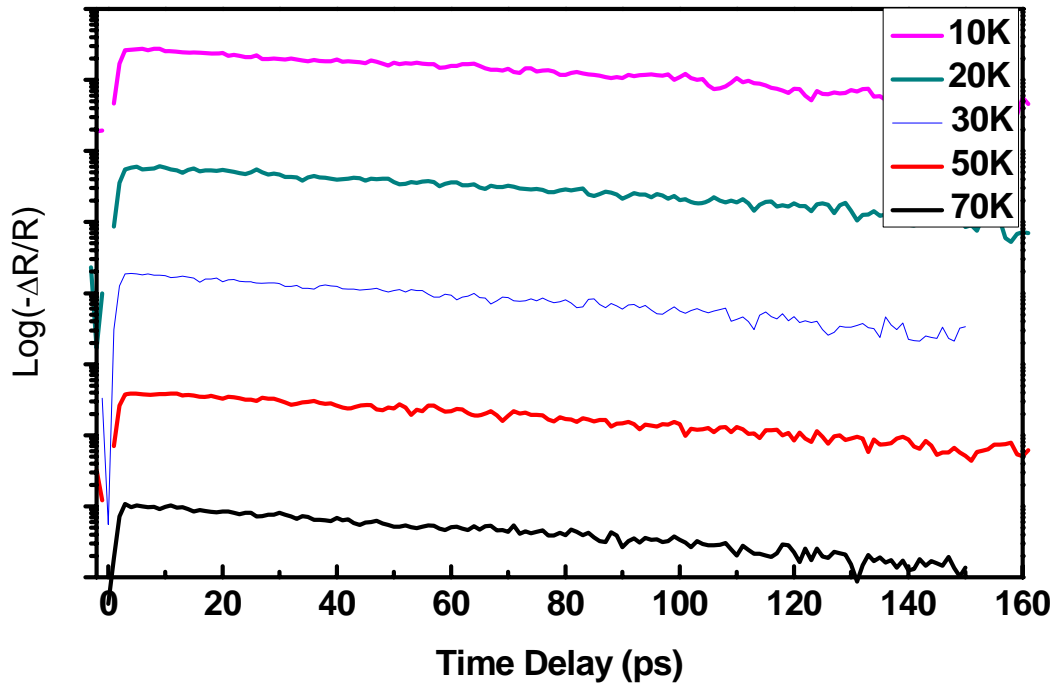
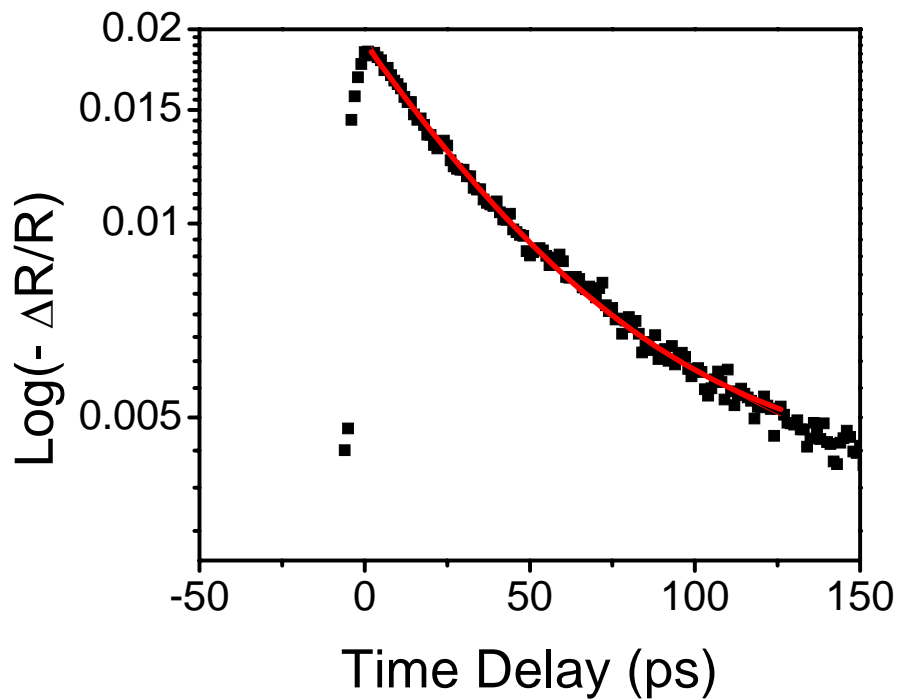
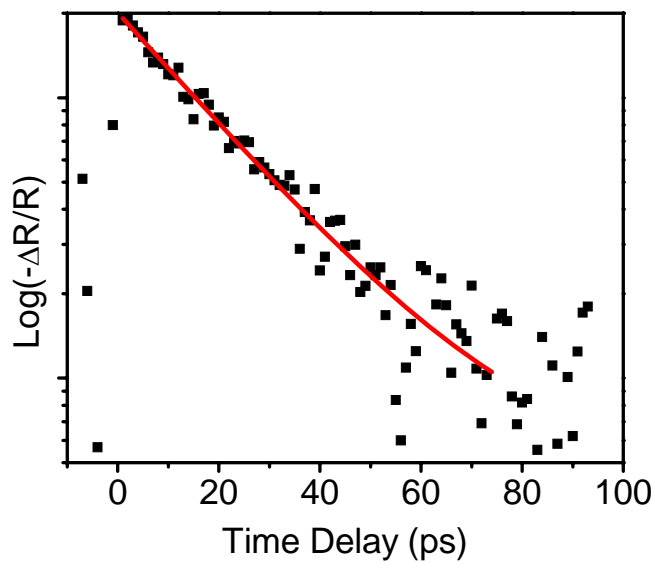


Figure 6-14. Temperature dependent TRDR of A-X recombination in c-plane bulk ZnO. Probe wavelength is tuned to the A-X resonant wavelength. The fitting results of decay time $\tau=130$ ps do not change significantly with the temperature increasing.



(a)



(b)

Figure 6-15. TRDR plots of excitonic recombination in ZnO epilayer for different exciton states. (a) A-X, probe tuned to 3375 meV (b) B-X, probe tuned to 3387 meV. Fitting result is shown with red line.

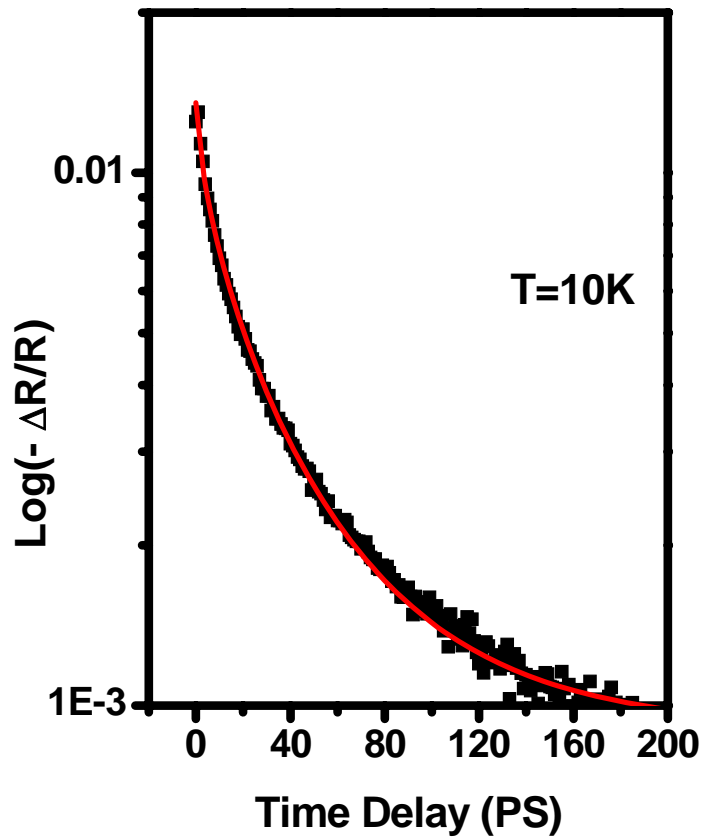


Figure 6-16. Experimental TRDR plot of ZnO nanorod sample at 10K and fitting result with a stretched exponential decay. Black dots are experimental results and red curve is fitting results with a stretched exponential function. Fitting parameter are $\tau=17\pm 1\text{ps}$ and $n=0.65\pm 0.01$.

CHAPTER 7 CONCLUSION AND FUTURE WORK

In order to study the carriers dynamics of III-V group semiconductor quantum wells at high carrier density ($\sim 10^{12} \text{cm}^{-2}$) and high magnetic fields, we have developed an ultrafast optics facility at the National High Magnetic Field Laboratory, including an ultrafast chirped pulse amplifier, optical parametric amplifier, and a 17.5 Tesla superconducting magnet (SCM3) as well as the necessary cryogenic system and optical probes for both SCM3 and the 31 T Bitter magnet in cell 5. This unique facility provides us high power pulses (GW/cm^2) in broad wavelength range (200nm to $20\mu\text{m}$) and high magnetic fields (up to 31 Tesla) to study the quantum optics of e - h pair in semiconductor quantum wells. A detailed description of this facility was shown in Chapter 2.

To understand the optical transmission and reflection spectrum of semiconductors, we gave a detailed description of the optical response theory. In addition, the detailed theory of the electronic states in semiconductor quantum well is given as well as the excitonic states and LL splitting in high magnetic field was presented.

With these as a background, this dissertation has presented a systemic spectroscopic study of magneto-optical properties of $\text{In}_x\text{Ga}_{1-x}\text{As}/\text{GaAs}$ multiple quantum well in the low and high excitation regimes using CW light source high excitation domain with a high power ultrafast light sources at magnetic field up to 30 T.

In low excitation regime, we can clearly resolve the interband LL transitions originating from the same conduction and valence subbands in the absorption spectrum of $\text{In}_x\text{Ga}_{1-x}\text{As}/\text{GaAs}$ multiple quantum wells at 4.2K to 30 T. Anticrossing phenomena and dark excitonic states are shown between the traces of e^1h^1ns and e^1l^1ns magneto excitonic states. Theoretical calculation shows that this larger splitting ($\sim 9 \text{meV}$) does not arise from valence band complexity.

In high excitation regime, we measured PL emission from $\text{In}_x\text{Ga}_{1-x}\text{As}/\text{GaAs}$ multiple quantum wells excited with high power CPA pulses ($\sim\text{GW}/\text{cm}^2$). We do not see Coulomb interaction-induced anticrossing between LL levels originating from heavy holes and light holes. Bandgap renormalization is clearly observed when we compared the Landau fan diagrams of absorption spectrum in low excitation and PL spectrum in high power regime. Both of these indicate that Coulomb interaction in e - h pair is screened at high carrier density ($\sim 10^{12}/\text{cm}^2$) and PL from high density e - h plasma dominates the out-of-plane PL emission at high field and high excitation.

In the high power excitation spectrum of $\text{In}_x\text{Ga}_{1-x}\text{As}/\text{GaAs}$ multiple quantum well, we observed strong and sharp features on the PL peaks, suggesting the study of amplified emission processes in the $\text{In}_x\text{Ga}_{1-x}\text{As}/\text{GaAs}$ MQWs. With the ultrafast facility developed at NHMFL, we were able to study the in-plane PL emission from $\text{In}_x\text{Ga}_{1-x}\text{As}/\text{GaAs}$ MQWs. We observed abnormally strong emission. By measuring and analyzing the field dependent, power dependent PL spectra and the single pulse excited PL spectra, we characterized this sharp peak emission. (I) the PL emission strength of sharp peak increased linearly above a certain magnetic field (13 T) or laser fluence ($0.01 \text{ mJ}/\text{cm}^2$) associated with an ASE process. (II) above a critical magnetic field ($\sim 16 \text{ T}$) or laser fluence ($\sim 0.03 \text{ mJ}/\text{cm}^2$), the PL strength increases super linearly ($\sim B^{1.5}$ or $F^{1.5}$), (III) for single pulse excitation above the fluence threshold, we collect the in-plane PL emission for different propagation directions, and the single shot experiment shows anticorrelated emission between the PL strength at different directions. However, for the single pulse excitation experiment, we observed a complete correlation between in-plane PL at different propagating directions, consistent with ASE emission. With an understanding of the cooperative theory of light emission introduced in detailed in chapter 5, we found that the characteristics of

strong PL above magnetic field or fluence threshold from in-plane emission are consistent with the cooperative emission process--superfluorescence, in which all the excited carrier are coherent during the emission process and give a very short burst emission of coherent light.

This dissertation also presents comprehensive spectroscopic investigations on ZnO semiconductors, including bulk, epilayer and nanorod samples. The A and B excitonic states are clearly identified in the reflection spectra with optical selection rules. PL from donor or acceptor bound excitons dominates the emission spectrum up to 70K in the bulk ZnO and ZnO epilayer. To understand the excitonic states of ZnO in more detail, we measured the PL spectrum at high magnetic field up to 30 Tesla. Zeeman splitting from donor bound excitons is clearly resolved and analyzed with theoretical predication, we found that in Voigt geometry, the effective Lande factor is $g \sim 2$, which is close to theoretical predication.

Ultrafast time resolved pump-probe experiments are also carried to study the A-X, B-X dynamics in bulk ZnO, ZnO epilayer as well as ZnO nanorod. Exponential decay is observed in A-X (~ 130 ps) and B-X (~ 50 ps) in bulk material, which is corresponding to relaxation to D^0X . In epilayer and nanorod sample, we observed stretched exponential decay process, ($n=0.9$ and $\tau=50$ ps for A-X for the epilayer, $n=0.6$, $\tau=17$ ps for the nanorods), related with carrier hopping transport and carrier localization.

For the future, we need to obtain the time resolved information of the cooperative recombination process in high density $e-h$ plasma in high magnetic field, including measuring the SF pulse width, time delay for evolution of coherence between atoms. We proposed the following experiments:

- Time resolved pump-probe experiment to measure the carrier dynamics in $\text{In}_x\text{Ga}_{1-x}\text{As}/\text{GaAs}$ QW at high magnetic fields. This can be done with the CPA and OPA.

- Time resolved PL from in-plane emission in QW at high magnetic field, this can be done with streak camera and provide us the time information of evolution of coherence.
- Upconversion PL measurement of SF from $\text{In}_x\text{Ga}_{1-x}\text{As}/\text{GaAs}$ QW in high magnetic field, this can provide us the time information of the pulse width of SF.

As for the ZnO semiconductor, we propose to perform time resolved PL measurements with a streak camera, which can provide more information of the radiative and nonradiative dynamics of exciton and bound excitons.

APPENDIX A SAMPLE MOUNT AND PHOTOLUMINESCENCE COLLECTION

A commercial Janis cryostat (shown in Fig.2-8) is modified for sending fs laser directly on the sample cooled down to 10K inside the cryostat. On the tail of modified optical cryostat shown in Fig.2-10, an optical window is mounted on the bottom of the cryostat outer tail. Fig. A-1 shows the detailed configuration of the sample mount, optical fiber and PL collection used in the experiments.

The sample mount, which is made of cooper, is bolted on the bottom of liquid helium tail of the cryostat. An indium foil is used between the sample mount and the bottom of liquid helium tail for better heat conduction. With this method, the sample can be cooled down to around 10K.

The $\text{In}_x\text{Ga}_{1-x}\text{As}/\text{GaAs}$ MQW is positioned on the top of a sapphire plate, which is about 1mm thick. Special optical glue is used to firmly attach the sample on the sapphire plate. This optical glue is transparent for visible and near infrared light, which is suitable for 800nm CPA excitation light and the PL emission around 930nm. The optical glue is dried with strong UV light heater. A right prism with size 1mmx1mm is also attached to the sapphire plate and one edge of the $\text{In}_x\text{Ga}_{1-x}\text{As}/\text{GaAs}$ MQW. The sapphire plate with sample on it is positioned on the cooper sample mount with GE varnish, special glue with good conductivity at low temperature. A Cernox temperature sensor is attached to the sample mount right beneath the sapphire plate, so that the temperature of sample can correctly measured. An electric heater is also position around the sapphire plate for temperature control.

Two optical fibers are inserted into the small tubing inside the liquid helium and go through the bottom of the helium tail, indium foil and sample mount, and reach the sapphire plate. The sapphire is positioned well so that the two fibers are right on the top of the center of

sample and the top of right angle prism respectively. The fiber on the center is used to collecting the PL emitted perpendicular to the quantum well plane while the fiber on the prism is used for collecting the PL propagating inside the quantum plane, the in plane PL is coupled into the fiber with the prism. Strong white light is induced to the fibers from the open end to find the best positions of the other ends of optical fiber on the top of sapphire plate.

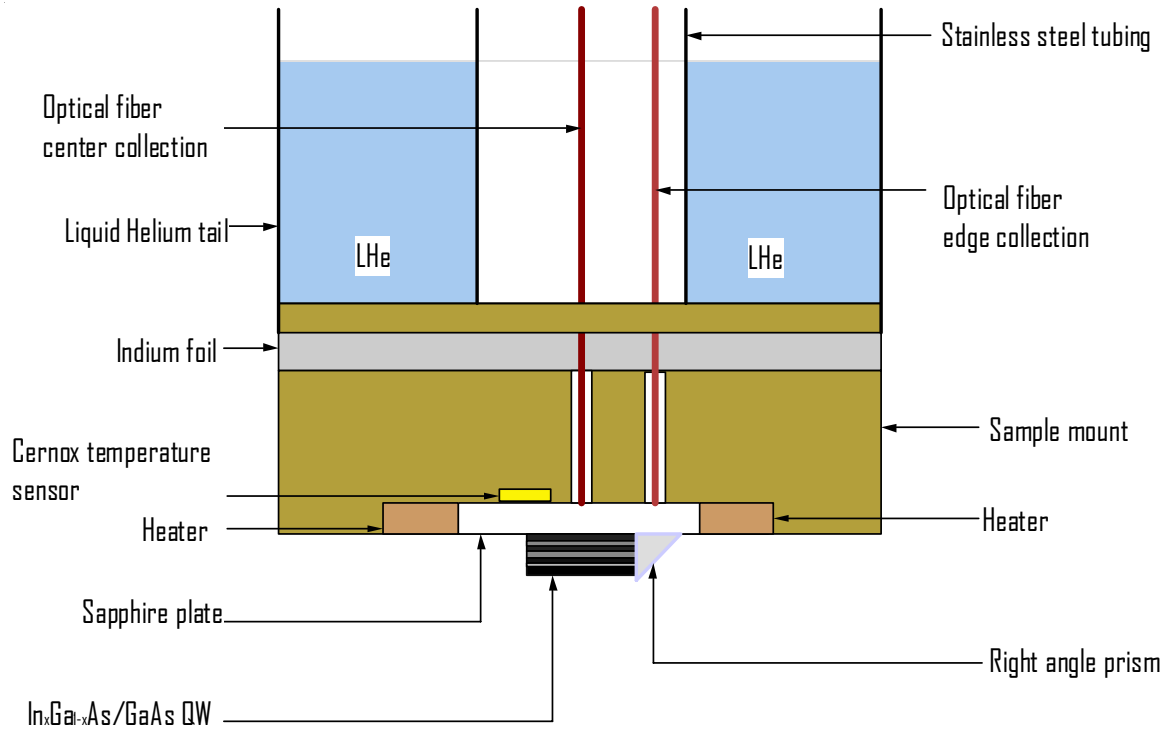


Figure A-1. Detailed schematic diagram of sample mount and PL collection used in the experiment.

APPENDIX B PIDGEON-BROWN MODEL

In a realistic calculation of electronic states in semiconductor in magnetic fields, $\mathbf{k} \cdot \mathbf{p}$ theory [71] is required to for good approximation of the bandstructure. For narrow gap semiconductors such InGaAs or InAs, the coupling between the conduction and valence bands is strong, so it is necessary to calculate the *LLs* with eight-band model. Pidgeon and Brown [94] develop a model to calculate the *LLs* in magnetic field at $k=0$. This model is generalized to include the wave vector ($k \neq 0$) in this chapter.

The wave function basis in Tab. 3-1 is still used in the calculation. In the presence of a uniform magnetic field B along z -axis, the wave vector k in the effective mass Hamiltonian is replaced by the operator

$$\mathbf{k} = \frac{1}{\hbar} \left(\mathbf{p} + \frac{e}{c} \mathbf{A} \right), \quad -1$$

where $\mathbf{p} = -i\hbar\nabla$ is momentum operator. In Landau gauge, $\mathbf{B} = \nabla \times \mathbf{A} = B \hat{z}$

Two operators are defined as

$$a^+ = \frac{\lambda}{\sqrt{2}} (k_x + ik_y), \quad \text{B-2 (a)}$$

$$a = \frac{\lambda}{\sqrt{2}} (k_x - ik_y), \quad \text{B-2 (b)}$$

where λ is the magnetic length $\lambda = \sqrt{\frac{\hbar c}{eB}}$.

The operators defined in Eq. B-2 are creation and annihilation operators. The states they create and annihilate are simple harmonic oscillator functions, and $aa^+ = N$ are the order of

Note: The Pidgeon-Brown Model is taken with permission from Y. Sun, Theoretical Studies of the Electronic Magneto-optical and Transport Properties of Diluted Magnetic Semiconductors, Page 45-50, PhD dissertation, Univ. of Florida, Gainesville, FL2005

harmonic functions. Using these two operators to eliminate k_x and k_y in the Hamiltonian, a new Landau Hamiltonian is reached

$$H_L = \begin{bmatrix} L_a & L_c \\ L_c^+ & L_b \end{bmatrix}, \quad \text{B-3}$$

The L_a , L_b and L_c are given by

$$L_a = \begin{bmatrix} E_g + A & i\frac{V}{\lambda}a & i\sqrt{\frac{1}{3}}\frac{V}{\lambda}a^+ & \sqrt{\frac{2}{3}}\frac{V}{\lambda}a^+ \\ -i\frac{V}{\lambda}a^+ & -P-Q & -M & i\sqrt{2}M \\ -i\sqrt{\frac{1}{3}}\frac{V}{\lambda}a & -M^+ & -P+Q & i\sqrt{2}Q \\ \sqrt{\frac{2}{3}}\frac{V}{\lambda}a & i\sqrt{2}M^+ & -i\sqrt{2}Q & -P-\Delta \end{bmatrix}, \quad \text{B-4}$$

$$L_b = \begin{bmatrix} E_g + A & i\frac{V}{\lambda}a^+ & -i\sqrt{\frac{1}{3}}\frac{V}{\lambda}a & i\sqrt{\frac{2}{3}}\frac{V}{\lambda}a \\ -\frac{V}{\lambda}a & -P-Q & -M^+ & i\sqrt{2}M^+ \\ -\sqrt{\frac{1}{3}}\frac{V}{\lambda}a & -M & -P+Q & i\sqrt{2}Q \\ -i\sqrt{\frac{2}{3}}\frac{V}{\lambda}a^+ & -i\sqrt{2}M & -i\sqrt{2}Q & -P-\Delta \end{bmatrix}, \quad \text{B-5}$$

$$L_c = \begin{bmatrix} 0 & 0 & \sqrt{\frac{2}{3}}Vk_z & i\sqrt{\frac{1}{3}}Vk_z \\ 0 & 0 & -L & -i\sqrt{\frac{1}{2}}L \\ -i\sqrt{\frac{2}{3}}Vk_z & L & 0 & i\sqrt{\frac{3}{2}}L^+ \\ -\sqrt{\frac{1}{3}}Vk_z & -i\sqrt{\frac{1}{2}}L & i\sqrt{\frac{3}{2}}L^+ & 0 \end{bmatrix}. \quad \text{B-6}$$

The operators A , P , Q , L and M are

$$A = \frac{\hbar^2}{m_0} \frac{\gamma_4}{2} \left(\frac{2N+1}{\lambda^2} + k_z^2 \right), \quad \text{B-7(a)}$$

$$P = \frac{\hbar^2}{m_0} \frac{\gamma_1}{2} \left(\frac{2N+1}{\lambda^2} + k_z^2 \right), \quad \text{B-7(b)}$$

$$Q = \frac{\hbar^2}{m_0} \frac{\gamma_2}{2} \left(\frac{2N+1}{\lambda^2} - 2k_z^2 \right), \quad \text{B-7(c)}$$

$$L = \frac{\hbar^2}{m_0} \gamma_3 \left(\frac{-i\sqrt{6}k_z a}{\lambda} \right), \quad \text{B-7(d)}$$

$$M = \frac{\hbar^2}{m_0} \left(\frac{\gamma_2 + \gamma_3}{2} \right) \left(\frac{\sqrt{3}}{\lambda^2} a^2 \right). \quad \text{B-7(e)}$$

The parameter $\gamma_1, \gamma_2, \gamma_3$ and γ_4 are Luttinger parameters [80] and Δ is the spin-orbit coupling. With Landau gauge translation symmetry in the x direction is broken while translation symmetry along the y and z directions is maintained. Therefore, k_y and k_z are good quantum numbers and the envelop of the effective mass Hamiltonian H_L can be written as

$$F_{nv} = \frac{e^{i(k_y y + k_z z)}}{\sqrt{A}} \begin{bmatrix} a_{1,n,v} \phi_{n-1} \\ a_{2,n,v} \phi_{n-2} \\ a_{3,n,v} \phi_n \\ a_{4,n,v} \phi_n \\ a_{5,n,v} \phi_n \\ a_{6,n,v} \phi_{n+1} \\ a_{7,n,v} \phi_{n-1} \\ a_{8,n,v} \phi_{n-1} \end{bmatrix}. \quad \text{B-8}$$

In Eq. B-8, n is the Landau quantum number associated with the Hamiltonian matrix, v labels the eigenvectors, $A=L_x L_y$ is the cross sectional area of the sample in the x-y plane, $\phi_n(\xi)$ are harmonic oscillator eigenfunctions evaluated at $\xi = x - \lambda^2 k_y$, and $a_{1,n,v}(k_z)$ is complex expansion coefficients for the vth eigenstate, which depend explicitly on n and k. Note that the wave functions themselves will be given by the envelop functions in Eq. B-8 with each component multiplied by the corresponding $k=0$ Bloch basis states given in Table 3-1.

Substituting F_{nv} from Eq. B-8 into the effective mass Schrodinger equation with H given by Eq. B-3, we obtain a matrix eigenvalue equation

$$H_n F_{n,v} = E_{n,v}(k_z) F_{n,v}.$$

That can be solved for each allowed value of the Landau quantum number, n, to obtain the Landau levels $E_{n,v}(k_z)$. The components of the normalized eigenvectors $F_{n,v}$ are the expansion coefficients a_i .

LIST OF REFERENCES

- 1 T. Ando, A. B. Fowler and F. Stern, *Rev. Mod. Phys.* **54**, 437 (1982).
- 2 D. A. Miller, D. S. Chemla, T. C. Damen, A. C. Gossard, W. Wiegmann, T. H. Wood, and C. A. Burrus, *Phys. Rev. B* **32**, 1043 (1985).
- 3 A. Gaj, W. Grieshaber, C. Bodin-Deshayes, J. Cibert, G. Feuillet, Y. Merle d'Aubigné, and A. Wasiela, *Phys. Rev. B* **50**, 5512 (1994).
- 4 S. N. Walck and T. L. Reinecke, *Phys. Rev. B* **48**, 17321 (1993).
- 5 C. Riva, F. M. Peeters, and K. Varga, *Phys. Rev. B* **46**, 1897 (1992).
- 6 M. Bagnall, Y. F. Chen, Z. Zhu, T. Yao, S. Koyama, M. Y. Shen, and T. Goto, *Appl. Phys. Lett.* **70**, 2230 (1997).
- 7 Y. Chen, N. T. Tuan, Y. Segawa, H. Ko, S. Hong, and T. Yao, *Appl. Phys. Lett.* **78**, 1469 (2001).
- 8 S. Cho, J. Ma, Y. Kim, Y. Sun, G. K. L. Wong, and J. B. Ketterson, *Appl. Phys. Lett.* **75**, 2761 (1999).
- 9 Z. Yu, K. Wang, G. Wong, M. Kawasaki, A. Ohtomo, H. Koinuma, and Y. Segawa, *J. Cryst. Growth* **184**, 601 (1998).
- 10 L. Ley, R. A. Pollak, F. R. McFeely, S. P. Kowalczyk, and D. A. Shirley, *Phys. Rev. B* **9**, 600 (1974).
- 11 P. Peyla, R. Romestain, Y. Merle d'Aubigné, G. Fishman, A. Wasiela, and H. Mariette, *Phys. Rev. B* **52**, 12026 (1995).
- 12 D. A. Kleinman, *Phys. Rev. B* **32**, 3766 (1985).
- 13 D. S. Chemla, J.Y. Bigot, M.A. Mycek, S. Weiss, and W. Schäfer, *Phys. Rev. Lett.* **81**, 2372 (1998).
- 14 S. L. Chuang, M. S. Luo, S. Schmitt-Rink, and A. Pinczuk, *Phys. Rev. B* **50**, 8439 (1994).
- 15 R. Winkler, *Phys. Rev. B* **59**, 15363 (1999).
- 16 G. E. Bauer, *Phys. Rev. B* **45**, 9153 (1992).
- 17 C. Riva, F. M. Peeters, and K. Varga, *Phys. Rev. B* **63**, 115302 (2001).
- 18 D. S. Citrin, *Phys. Rev. B* **52**, 12026 (1995).

- 19 S. N. Walck, T. L. Reinecke, and P. A. Knipp, *Phys. Rev. B* **59**, 5568 (1999).
- 20 R. L. Greene, K. K. Bajaj, and D. E. Phelps, *Phys. Rev. B* **29**, 1807 (1984).
- 21 D. Paquet, T. M. Rice, and K. Ueda, *Phys. Rev. B* **32**, 5208 (1985).
- 22 S. K. Lyo, E. D. Jones, and J. F. Klem, *Phys. Rev. Lett.* **61**, 2265 (1988).
- 23 X. Zhu and S. G. Louie, *Phys. Rev. B* **52**, 5863 (1995).
- 24 R. Yakovlev, V. P. Kochereshko, R. A. Suris, H. Schenk, W. Ossau, A. Waag, G. Landwehr, P. C. Christianen, and J. C. Maan, *Phys. Rev. Lett.* **79**, 3974 (1997).
- 25 H. Morf, N. d'Ambrumenil, and S. Das Sarma, *Phys. Rev. B* **66**, 075408 (2002).
- 26 J. Wang, C. Sun, Y. Hashimoto, J. Kono, G. A. Khodaparast, L. Cywinski, L. J. Sham, G. D. Sanders, C. J. Stanton, and H. Munekata, *J. Phys.: Condensed Matter* **18**, 34754 (2006).
- 27 J. Wang, C. Sun, J. Kono, A. Oiwa, H. Munekata, L. Cywinski, and L. J. Sham, *Phys. Rev. Lett.* **95**, 167401 (2005).
- 28 S. A. Crooker, D. A. Tulchinsky, J. Levy, D. D. Awschalom, R. Garcia, and N. Samarth, *Phys. Rev. Lett.* **75**, 505 (1995).
- 29 S. A. Crooker, J. J. Baumberg, F. Flack, N. Samarth, and D. D. Awschalom, *Phys. Rev. Lett.* **77**, 2814 (1996).
- 30 S. A. Crooker, D. D. Awschalom, J. J. Baumberg, F. Flack, and N. Samarth, *Phys. Rev. B* **56**, 7574 (1997).
- 31 J. B. Stark, W. H. Knox, D. S. Chemla, W. Schäfer, S. Schmitt-Rink, and C. Stafford, *Phys. Rev. Lett.* **65**, 3033 (1990).
- 32 P. Kner, S. Bar-Ad, M. V. Marquezini, D. S. Chemla, and W. Schäfer, *Phys. Rev. Lett.* **78**, 1319 (1997).
- 33 Y. E. Lozovik, I. V. Ovchinnikov, S. Yu. Volkov, L. V. Butov, and D. S. Chemla, *Phys. Rev. B* **65**, 235304 (2002).
- 34 S. H. Autler, C. H. Townes, *Phys. Rev.* **100**, 703-722 (1955).
- 35 R. H. Dicke, *Phys. Rev.* **93**, 99 (1954).
- 36 N. Skribanowitz, I. P. Herman, J. C. MacGillivray, and M. S. Feld, *Phys. Rev. Lett.* **30**, 309 (1973).

- 37 I. Vurgaftman and J. R. Meyer, *J. Appl. Phys.* **89**, 5815 (2001).
- 38 S. Schmitt, D. S. Chemla and D. A. B. Miller, *Advance in Physics*, **38**, 89 (1989).
- 39 N. W. Ashcroft, *Solid State Physics*, Holt Rinehart and Winston, International Ed edition, New York (1987).
- 40 C. Klingshrim, *Semiconductor Optics*, Springer, 3rd ed. Edition, New York (2006).
- 41 N. Peyghambarian, *Introduction to Semiconductor Optics*, Prentice Hall College Div., 1st edition, New York (1993).
- 42 I. B. Joseph, J. M. Kuo and C. Klingshirn, *Phys. Rev. Lett.*, **59**, 1357 (1987).
- 43 M. S. Skolnick, P. R. Tapster and S. J. Bass, *Semiconductor Science and Technology* **1** 29, (1986).
- 44 S. D. Gunapala, *Appl. Phy. Lett.*, **58**, 2024 (1991).
- 45 H. Temkin, T. Tanbunek and R. Logan, *IEEE Photonics Technology Letters* **3**, 100 (1991).
- 46 M. Hickey, C. Damsgard and I. Farrer, *Appl. Phy. Lett.*, **86**, 252106 (2005).
- 47 M. Skolnick, P. Tapster and S. Bass, *Semiconductor Science and Technology* **1**, 29 (1986).
- 48 R. Schneider and B. Wessels, *Journal of Electronic Materials*, **20**, 1117 (1991).
- 49 T. Arakwa, *Japanese Journal of Applied Physics Part 2-Letters* **32**, L1377 (1993).
- 50 P. Wiesner, R. A. Street, and H. D. Wolf, *Phys. Rev. Lett.* **35**, 1366 (1975).
- 51 D. A. Miller, D. S. Chemla, T. C. Damen, A. C. Gossard, W. Wiegmann, T. H. Wood, and C. A. Burrus, *Phys. Rev. B* **32**, 1043 (1985).
- 52 M. Joffre, D. Hulin, A. Migus, and M. Combescot, *Phys. Rev. Lett.* **62**, 74 (1989).
- 53 K. Leo, M. Wegener, J. Shah, D. S. Chemla, E. O. Göbel, T. C. Damen, S. Schmitt-Rink, and W. Schäfer, *Phys. Rev. Lett.* **65**, 1340 (1990).
- 54 M. Wegener, D. S. Chemla, S. Schmitt-Rink, and W. Schäfer, *Phys. Rev. A* **42**, 5675 (1990).
- 55 H. J. Zeiger, J. Vidal, T. K. Cheng, E. P. Ippen, G. Dresselhaus, and M. S. Dresselhaus, *Phys. Rev. B* **45**, 768 (1992).

- 56 G. D. Sanders and C. J. Stanton, Phys. Rev. B **74**, 205303 (2006).
- 57 J. L. Krause, D. H. Reitze, G. D. Sanders, A. V. Kuznetsov, and C. J. Stanton, Phys. Rev. B **57**, 9024 (1998).
- 58 A. V. Kuznetsov and C. J. Stanton, Phys. Rev. B **48**, 10828 (1993).
- 59 G. N. Ostojic, J. Shaver, S. Zaric, and J. Kono, Physica E-Low-Dimensional Systems & Nanostructures **29**, 469 (2005).
- 60 S. Zaric, G. Ostojic, J. Shaver, and J. Kono, Phys. Rev. Lett., **96**, 016406 (2006).
- 61 S. Zaric, G. N. Ostojic, J. Kono, J. Shaver, V. C. Moore, M. S. Strano, R. H. Hauge, R. E. Smalley, and X. Wei, *Science* **304**, 1129 (2004).
- 62 J. Schnack, M. Bruger, M. Luban, P. Kogerler, E. Morosan, R. Fuchs, R. Modler, J. Musfeldt, and X. Wei, Phys. Rev. B **73**, 094401 (2006).
- 63 J. Woodward, J. Choi, and J. Musfeldt, Phys. Rev. B **71**, 174416 (2005).
- 64 J. Cao, J. Haraldsen, R. Rai, S. Brown, J. Musfeldt, Y. Wang, and X. Wei, Phys. Rev. B **74**, 045113 (2006).
- 65 R. Rai, J. Cao, J. Musfeldt, S. Kim, and X. Wei, Phys. Rev. B **75**, 184414 (2007).
- 66 R. Rai, J. Cao, J. Musfeldt, and X. Wei, Phys. Rev. B **73**, 075112 (2006).
- 67 L. Kuskovsky, W. MacDonald, A. O. Govorov, L. Mourokh, and X. Wei, Phys. Rev. B **76**, 035342 (2007).
- 68 M. Guillot, F. Zhang, Y. Xu, J. Yang, and X., Wei, J. Appl. Phys. **101**, C510 (2007).
- 69 DC Field Instruments & Tools at the National High Magnetic Field Laboratory, <http://www.magnet.fsu.edu/usershub/scientificdivisions/dcfld/cell5grad/cell5sidegrad.html>, last accessed September, 2007.
- 70 A. Crubellier, S. Liberman, and P. Pillet, Phys. Rev. Lett. **41**, 1237 (1978).
- 71 G. Basterd, *Wavemechanics Applied to Semiconductor Heterostructures*, Wiley-Interscience, 1st edition, NewYork (1991).
- 72 E.O. Kane, J. Phys. Chem. Solids **1**, 249(1957).
- 73 D. W. Kim, Y. A. Leem, S. D. Yoo, D. H. Woo, D. H. Lee, and J. C. Woo, Phys. Rev. B **47**, 2042 (1993).

- 74 G. Bastard, E. E. Mendez, L. L. Chang, and L. Esaki, Phys. Rev. B, **26** 1974 (1982).
- 75 L. Greene, K. Krishan, and P. Dwight, Phys. Rev. B **29**, 1807 (1984).
- 76 D. A. Miller, D. S. Chemla, T. C. Damen, A. C. Gossard, W. Wiegmann, T. H. Wood, and C. A. Burrus, Phys. Rev. B **32**, 1043 (1985).
- 77 A. Baldereschi and C. Nunzio, Phys. Rev. B **3**, 439 (1971).
- 78 Ioffe Institute, Electronic archive New Semiconductor Materials. Characteristics and Properties, GaAs <http://www.ioffe.rssi.ru/SVA/NSM/Semicond/GaAs/Figs/421.gif>, last accessed September, 2007.
- 79 Ioffe Institute, Electronic archive New Semiconductor Materials. Characteristics and Properties, GaN, <http://www.ioffe.rssi.ru/SVA/NSM/Semicond/GaN/bandstr.html>, last accessed September, 2007.
- 80 G. E. Bauer and T. Ando, Phys. Rev. B **38**, 6015 (1988).
- 81 I. Vurgaftmana and J. R. Meyer, J. of Appl. Phys., **89**, 5815 (2001).
- 82 Y. D. Jho, F. Kyrychenko, G. Sanders, X. Wei, D. Reitze, J. Kono, C. Stanton, and S. Solomon, Phys. Rev. B **72**, 045340 (2005).
- 83 L. V. Butov, A. Zrenner, M. Shayegan, G. Abstreiter, and H. C. Manoharan, Phys. Rev. B **49**, 14054 (1994).
- 84 L. V. Butov, V. D. Kulakovskii, G. E. Bauer, A. Forchel, and D. Grützmacher, Phys. Rev. B **46**, 12765 (1992).
- 85 G. E. Bauer and T. Ando, Phys. Rev. B **37**, 3130 (1988), H. Aoki and T. Ando, Phys. Rev. Lett. **54**, 831 (1985).
- 86 L. V. Butov, V. D. Egorov, V. D. Kulakovskii, and T. G. Andersson, Phys. Rev. B **46**, 15156 (1992).
- 87 A. H. MacDonald and D. S. Ritchie, Phys. Rev. B **33**, 8336 (1986).
- 88 L. V. Butov, V. D. Kulakovskii, E. Lach, A. Forchel, and D. Grützmacher, Phys. Rev. B **44**, 10680 (1991).
- 89 L. V. Butov, V. D. Kulakovskii, and G. E. Bauer, Phys. Rev. B **46**, 12765 (1992).
- 90 G. E. Bauer and T. Ando, Phys. Rev. B **37**, 3130 (1988).
- 91 W. Hanke and L. J. Sham Phys. Rev. Lett. **43**, 387 (1979).

- 92 S. R. Yang and L. J. Sham Phys. Rev. Lett. **58**, 2598 (1987).
- 93 L. V. Butov, V. D. Kulakovskii, and T. G. Andersson, Phys. Rev. B **44**, 1692 (1991).
- 94 R. Pidgeon and R. N. Brown, Phys. Rev. **146**, 575 (1966); E. O. Kane J. Phys. Chem. Solids **1**, 249 (1957).
- 95 L. V. Butov, V. D. Kulakovskii, and G. E. Bauer, Phys. Rev. B **46**, 12765 (1992).
- 96 R. Boyd, *Nonlinear Optics*, Academic Press, 2nd edition, New York (2002).
- 97 Y. Yoshihisa, *Mesoscopic Quantum Optics*, John Wiley, 3rd edition, New York (1999).
- 98 P. Meystre, *Atomic Optics*, Springer-Verlag, 2nd edition, New York (2001).
- 99 L. Allen *et al.*, *Optical Resonance and Two-level Atoms*, Wiley, 2nd edition, New York (1975).
- 100 F. Tsai *et al.*, Journal of Applied Physics **89**, 7875 (2007).
- 101 A. Djurisic, W. Kwok, Y. Leung, *et al.*, Nanotechnology **17**, 244 (2006).
- 102 H. M. Gibbs, Q. H. Vreken, and H. M. Hikspoors, Phys. Rev. Lett. **39**, 547 (1977).
- 103 N. Skribanowitz, I. P. Herman, J. C. MacGillivray, and M. S. Feld, Phys. Rev. Lett. **30**, 309 (1973).
- 104 M. Gross, C. Fabre, P. Pillet, and S. Haroche, Phys. Rev. Lett. **36**, 1035 (1976).
- 105 Y. Kaluzny, P. Goy, M. Gross, J. M. Raimond, and S. Haroche, Phys. Rev. Lett. **51**, 1175 (1983).
- 106 A. T. Rosenberger and T. A. DeTemple, Phys. Rev. A **24**, 868 (1981).
- 107 R. Bonifacio, P. Schwendimann, and Fritz Haake, Phys. Rev. A **4**, 854 (1971); R. Bonifacio, P. Schwendimann, and F. Haake, Phys. Rev. A **4**, 302 (1971).
- 108 J. C. MacGillivray and M. S. Feld, Phys. Rev. A **14**, 1169 (1976).
- 109 H. M. Gibbs, Q. H. Vreken, and H. M. Hikspoors, Phys. Rev. Lett. **39**, 547 (1977).
- 110 A. Crubellier, S. Liberman, and P. Pillet, Phys. Rev. Lett. **41**, 1237 (1978).
- 111 A. Belyanin, V. Kocharovskiy and V. Kocharovskiy, Quantum and Semiclass. Optics, **9**, 1 (1997).

- 112 A. Kazantzev and V. Smirnov, Sov. Phys. JETP. **19**, 130 (1964); A. Alekseev, Y. Vdovin, and V. Galitzky, Sov. Phys. JETP. **19**, 220, (1964).
- 113 V. Zheleznyakov and V. Kocharovsky, Sov. Phys.Usp, **32**, 835 (1989).
- 114 A. Belyanin, V.V. Kocharovsky, and VI.V. Kocharovsky, JEOS Part B (Quantum & Semiclass. Optics) **10**, L13 (1998).
- 115 A. Belyanin, V.V. Kocharovsky, and VI.V. Kocharovsky, Bull. Russian Acad. Sciences, **62**, 372 (1998).
- 116 A. Belyanin, V.V. Kocharovsky, and VI.V. Kocharovsky, Computers Math. Application. **34**, 845 (1997).
- 117 A. Belyanin, V.V. Kocharovsky, and VI.V. Kocharovsky, Laser Physics, **5**, 1121 (1995).
- 118 A. Belyanin, V.V. Kocharovsky, and VI.V. Kocharovsky, Solid State Commun., **80**, 243 (1991).
- 119 A. I. Lvovsky, S. R. Hartmann, and F. Moshary, Phys. Rev. Lett. **82**, 4420 (1999).
- 120 Spontaneous emission, Wikipedia, the free encyclopedia, http://en.wikipedia.org/wiki/Spontaneous_emission, last accessed September, 2007.
- 121 Stimulated emission, Wikipedia, the free encyclopedia, http://en.wikipedia.org/wiki/Stimulated_emission, last accessed September, 2007.
- 122 Z. Z. Ye *et al.*, Appl. Phys. Lett. **91**, 113503 (2007).
- 123 Y. Ogawa and S. Fujihara, J. Electrochem. Soc. **154**, J283 (2007).
- 124 D. Yu, Y. Chen, B. Li, and S. Ren, Appl. Phys. Lett. **91**, 091116 (2007).
- 125 F. A. Selim, M. H. Weber, D. Solodovnikov, and K. G. Lynn, Phys. Rev. Lett. **99**, 085502 (2007).
- 126 M. Al-Suleiman, A. El-Shaer, A. Bakin, H.H. Wehmann, and A. Waag, Appl. Phys. Lett. **91**, 081911 (2007).
- 127 B. Monemar, Phys. Rev. B **10**, **676** (1974).
- 128 W. F. Brinkman and T. M. Rice, Phys. Rev. B **7**, 1508 (1973).
- 129 Y. Harada and S. Hashimoto, Phys. Rev. B **68**, 045421 (2003); M. Zamfirescu, A. Kavokin, B. Gil, G. Malpuech, and M. Kaliteevski, Phys. Rev. B **65**, 161205 (2002).

- 130 Ü. Özgür,^a Ya. I. Alivov, C. Liu, A. Teke,^b M. A. Reshchikov, S. Doğan,^c V. Avrutin,^{S.-J. Cho,} and H. Morkoçd, *J. of Appl. Phys.* **98**, 041301 (2005).
- 131 X. Sun , K. Maeda, M. Faucheur M, *et al.*, *Applied Catalysis A-General* **327**, 114 (2007).
- 132 A. Kobayashi, S. Kawano, Y. Kawaguchi, *et al.*, *Appl. Phys. Lett.* **90**, 041908 (2007).
- 133 C. Sun, S. Sun, K. Lin, *et al.*, *Appl. Phys. Lett.* **87**, 023106 (2005).
- 134 S. Yamamoto, H. Yano, T. Mishina, *et al.*, *J. of Lumin.*, **126**, 257 (2007).
- 135 Y. S. Park, C. W. Litton, T. C. Collins, and D. C. Reynolds, *Phys. Rev.* **143**, 512 (1966).
- 136 A. Rodina, M .Strassburg, M. Dworzak, *et al.*, *Phys. Rev. B* **69** (12), (2005).
- 137 R. Dietz, D. Thomas, and J. Hopfield, *J. of Appl. Phys.* **32**: 2282& Suppl. (1961).
- 138 D. C. Reynolds, D. C. Look, B. Jogai, C. W. Litton, T. C. Collins, W. Harsch, and G. Cantwel, *Phys. Rev. B* **57**, 12151 (1998).
- 139 D. Reynolds, D. Look, B. Jogai, *et al.*, *J. of Appl. Phys.* **86**, 5598 (1999).
- 140 D. C. Reynolds, D. C. Look, B. Jogai, C. W. Litton, T. C. Collins, W. Harsch, and G. Cantwell, *Phys. Rev. B* **57**, 12151 (1998).
- 141 Chris Cook and Chris Stanton, in preparation for PRB.
- 142 A. Teke, U. Ozgur, S. Dogan, *et al.*, *Phys. Rev. B* **70**, 195207 (2004).
- 143 J. Shah, *Ultrafast Spectroscopy of Semiconductors and Semiconductor Nanostructures*, Springer, 2nd enlarged Edition, New York (1999).
- 144 L. Pavesi, *J. Appl. Phys.* **80**, 216 (1996).
- 145 I. Mihalcescu, J. C. Vial, and R. Romestain, *Phys. Rev. Lett.* **80**, 3392 (1998).
- 146 I. Mihalcescu, J. C. Vial, and R. Romestain, *J. Appl. Phys.* **80**, 2404 (1996).
- 147 E. Martin, C. Delerue, G. Allan, and M. Lannoo, *Phys. Rev. B* **50**, 18 258 (1994).

BIOGRAPHICAL SKETCH

Xiaoming Wang was born in Nov. 1971. He earned the Bachelor of Science degree at Tianjin University, China, in 1994. After that he entered the graduate school of Tianjin University and got his Master of Science degree in physics in 1997. Right after that, he started his job as a research associate in the Institute of Physics, China Academy of Sciences. After three year of being a research associate in the Institute of Physics, Chinese Sciences, he resigned his job and came to University of Florida in 2000, to pursue a Ph.D in physics. He joined Prof. David Reitze's ultrafast group in summer 2001. He has been working for several different research projects, some of which are related to this dissertation.